RAYLEIGH-WAVE MULTICOMPONENT CROSSCORRELATION-BASED ESTIMATION OF PHASE VELOCITIES AND AMBIENT SEISMIC SOURCE DISTRIBUTIONS

by

Zongbo Xu

A dissertation

submitted in partial fulfillment

of the requirements for the degree of

Doctor of Philosophy in Geophysics

Boise State University

May 2020

BOISE STATE UNIVERSITY GRADUATE COLLEGE

DEFENSE COMMITTEE AND FINAL READING APPROVALS

of the thesis submitted by

Zongbo Xu

Thesis Title: Rayleigh-wave multicomponent crosscorrelation-based estimation of phase velocities and ambient seismic source distributions

Date of Final Oral Examination: 6 March 2020

The following individuals read and discussed the dissertation submitted by student Zongbo Xu, and they evaluated the student's presentation and response to questions during the final oral examination. They found that the student passed the final oral examination.

T. Dylan Mikesell Ph.D.	Chair, Supervisory Committee
John Pelton Ph.D.	Member, Supervisory Committee
Lee M. Liberty M.S.	Member, Supervisory Committee
Jodi L. Mead Ph.D.	Member, Supervisory Committee

The final reading approval of the thesis was granted by T. Dylan Mikesell Ph.D., Chair of the Supervisory Committee. The thesis was approved by the Graduate College.

ACKNOWLEDGMENT

I spent four enjoyable years as a Ph.D. student at Boise State. Many people made my time in Boise such a great experience. At the end of this experience, I would like to say thank you again to these people, as I guess I have said many times to them before.

It is perfect to work with Dylan. Dylan has showed me what a professional researcher, a supportive advisor and a good friend is. He always encourages me to explore my own research interests, and provides a lot of support. With his support, I attended many academic conferences including 2019 Cargese summer school, did a summer internship at MIT, and worked with Dr. Ludovic Margerin for about three months in France. I still remember Dylan's revision of my first paper manuscript in Boise. The manuscript was about 25 pages and almost each page was fully marked with his comments. I can not imagine how much time and patience the revision took. When he handed the revised manuscript to me, he said good work with a smile as usual. At that time, I was thinking that I want to be such an awesome advisor in the future.

I would like to express my appreciation to my committee members and faculty members. I often asked Jack fundamental questions about seismology, and I guess sometimes my questions took a lot of his time. However, Jack is always patient and explain to me in details. Jack is such an ideal teacher that I want to be. Lee helped

me a lot in seismic method applications and Jodi is always nice to my questions about inverse theory. I also want to say thank you to Ludovic. Without his help, the France journey will not be possible. Ludovic showed me a totally new field for me, multiply scattering, and is always happy to answer my questions. I thank Karen, John, Shawn and HP. I also thank Tomo, Esther, Aurelian, Dr. Niels Grobbe, Dr. Sarah Kruse.

I also want to thank my friends. Diego, Aida and Rebekah helped me a lot to get used to the US life when I first got here. Chatting with Gabe, Alex, Megan and Tate is always a good relaxing from research. I also want to thank Feng, Xue, Yudi and Lingli for their hospitality.

This Ph.D. research is supported by many sources. I would like to thank the financial support from NSF, SEG scholarship, GSA graduate student research grant and Burnham Graduate Research grant. I also want to thank Boise State research computer support, and also Geosciences IT support, James.

Last but not least, I am grateful to my family. My wife, Yang, always supports, encourages and accompanies me. Thank you, my love. I can not imaging finishing my Ph.D. without Yang. I also want to express my appreciation to my parents, Junyuan and Xiangchun, my parents in law, Zhengqu and Xiaocui, my brother and sister.

ABSTRACT

One uses seismic interferometry (SI) to recover Green's functions (i.e. impulse response) from ambient seismic recordings and estimate surface-wave phase velocities to investigate subsurface structure. This method has been commonly used in the last 20 years because this method only utilizes ambient seismic recordings from seismic stations/sensors and does not rely on traditional seismic sources (e.g. earthquakes or active sources). SI assumes that the ambient seismic wavefield is isotropic, but this assumption is rarely met in practice. We demonstrate that, with linear-array spatial sampling of an anisotropic ambient seismic wavefield, SI provides a better estimate of Rayleigh-wave phase velocities than another commonly used ambient seismic method, the refraction microtremor (ReMi) method. However, even SI does not work in some extreme cases, such as when the out-of-line sources are stronger than the in-line sources. This is because the recovered Green's functions and surface-wave phase velocity estimations from SI are biased due to the anisotropic wavefield. Thus, we propose to use multicomponent data to mitigate this bias. The multicomponent data are vertical (Z) and radial (R) components, where the R direction is parallel to a line or great circle path between two sensors. The multicomponent data can deal with the extreme anisotropic source cases, because the R component is more sensitive to the in-line sources than the out-of-line sources, while the Z component possesses a constant sensitivity to sources in all directions.

Estimation of source distributions (i.e. locations and strengths) can aid correction of the bias in SI results, as well as enable the study of natural ambient seismic sources (e.g. microseism). We use multicomponent seismic data to estimate ambient seismic source distributions using full-waveform inversion. We demonstrate that the multicomponent data can better constrain the inversion than only the Z component data, due to the different source sensitivities between the Z and R components. When applying the inversion to field data, we propose a general workflow which is applicable for different field scales and includes vertical and multicomponent data. We demonstrate the workflow with a field data example from the CO_2 degassing in Harstoušov, Czech Republic. We also apply the workflow to the seismic recordings in Antarctica during February 2010 and estimate the primary microseism source distributions.

The SI results include both direct and coda waves. While using the direct waves in investigating subsurface structure and estimating source distributions, one can utilize the coda waves to monitor small changes in the subsurface. The coda waves include multiply-scattered body and surface waves. The two types of waves possess different spatial sensitivities to subsurface changes and interact each other through scattering. We present a Monte Carlo simulation to demonstrate the interaction in an elastic homogeneous media. In the simulation, we incorporate the scattering process between body and Rayleigh waves and the eigenfunctions of Rayleigh waves. This is a first step towards a complete modelling of multiply-scattered body and surface waves in elastic media.

TABLE OF CONTENTS

LIST OF FIGURES

LIST OF TABLES

CHAPTER 1:

INTRODUCTION

Mechanical waves are a common type of physical phenomena. For example, when we talk, we actually generate acoustic waves; the acoustic waves propagate through air and then are received by another person's ears, so the person hears us. The whole process is similar to the seismic wave propagation. Seismic sources (e.g. earthquakes) generate seismic waves; the seismic waves propagate through the solid Earth and then are received by sensors (e.g. geophones or seismometers). One can use the wave propagation to infer properties of the wave sources, as well as the structure through which it propagates. For example, one can tell who is talking based on which direction the acoustic waves are coming from and the vocal properties, usually frequency. In seismology, one can study source mechanisms for earthquakes and ambient seismic sources (e.g. microseisms caused by ocean activities) based on seismic recordings (e.g. Aki & Richards, 2002). The wave propagation also enables one to investigate subsurface structure, which is another important application in seismology. Subsurface investigations can provide estimates of subsurface structure to aid geotechnical engineering (e.g. Kramer, 2002), hydrocarbon exploration (e.g. Yilmaz, 2001), and solid earth studies (e.g. Dahlen & Tromp, 1998; Aki & Richards, 2002).

The basic idea underlying seismic methods is simple, but in practice is hard. A seismic recording is a convolution between the seismic source(s) and seismic wave

propagation along a path, which implies that the sources and propagation are coupled. One can not study the sources without accurately knowing the propagation and vice versa. Real wave propagating in the subsurface is extremely complex because the subsurface in reality is viscoelastic, anisotropic and inhomogeneous at all spatial scales. In order to study the propagation, one usually assumes that the subsurface media is elastic and isotropic, and thus focuses on just imaging the subsurface heterogeneity. To investigate the heterogeneity, one commonly studies wave velocities (e.g. P-/S-/surface-wave velocities) in the media.

One can use "noise" in seismic recordings to estimate subsurface velocity models. In seismic recordings, besides transient signals (e.g. earthquakes), the continuous "noise" mainly are waves from ambient seismic sources, such as microseisms (frequency<0.12 Hz) and traffic (frequency>2 Hz). If the ambient seismic sources are equal in strength and isotropically distributed in all directions around two sensors, one can use a noise crosscorrelation between the two sensors to approximate the band-limited Green's function (impulse response) between the sensors. This method is called Seismic Interfermoetry (SI, e.g. Wapenaar & Fokkema, 2006). As the Green's function represents the wave propagation, one can apply SI to subsurface investigations. One commonly recovers surface-wave Green's functions from the ambient seismic noise (e.g. Shapiro *et al.*, 2005) and thus uses surface-wave tomography to investigate Earth's crust (e.g. Yao *et al.*, 2006; Lin *et al.*, 2008). People have also applied this method in urban areas to estimate shallow shear-wave velocity (V_S) models (e.g. Halliday *et al.*, 2008; Xu *et al.*, 2013; Cheng *et al.*, 2015).

The isotropic source assumption is rarely met in practice. To meet the assumption, one usually has to use long-time (e.g. over 1 year) seismic recordings and preprocess-

ing procedures (time-/frequency-domain normalization, e.g. Bensen *et al.*, 2007) in the SI method. Without this assumption, the crosscorrelation does not approximate the Green's function anymore (e.g. Yang & Ritzwoller, 2008), and thus the surface-wave velocities estimated from the crosscorrelations will be biased (e.g. Yao & Van Der Hilst, 2009). In this case, many solutions have been proposed (e.g. Stehly *et al.*, 2008; Yao & Van Der Hilst, 2009). The main idea beneath these solutions is either normalizing source strengths in all directions (e.g. Stehly *et al.*, 2008; Seydoux *et al.*, 2017) or correcting the crosscorrelations/velocities based on the dominate source direction(s) (e.g. Yao & Van Der Hilst, 2009; Wapenaar *et al.*, 2011; Nakata *et al.*, 2015; Cheng *et al.*, 2016). Most of these solutions assume that the seismic waves from ambient seismic sources are plain waves. However, the waves can not be treated as plain waves if the sources are close to the sensors (e.g. Park & Miller, 2008) or the subsurface is laterally heterogeneous (e.g. Froment *et al.*, 2011).

One can also use ambient seismic noise to study the ambient seismic sources. The ambient seismic sources in low frequencies (<0.12 Hz) are mainly microseisms, including primary/secondary microseisms (e.g. Longuet-Higgins, 1950; Hasselmann, 1963) and Earth's hum (e.g. Ardhuin *et al.*, 2011b). Some microseismic source mechanisms are still unclear, such as the origins of Earth's hum (e.g. Traer & Gerstoft, 2014; Ardhuin *et al.*, 2015) and Love waves in microseisms (e.g. Nishida *et al.*, 2008; Juretzek & Hadziioannou, 2016). To study these source mechanisms, one would like knowledge of these sources (e.g. strengths and locations). As stated above, however, the source information and the wave propagation (i.e. Green's function) are coupled in the seismic crosscorrelations (e.g. Fichtner, 2015). Thus with a relatively accurate subsurface structure model, one can simulate the wave propagation in the model and

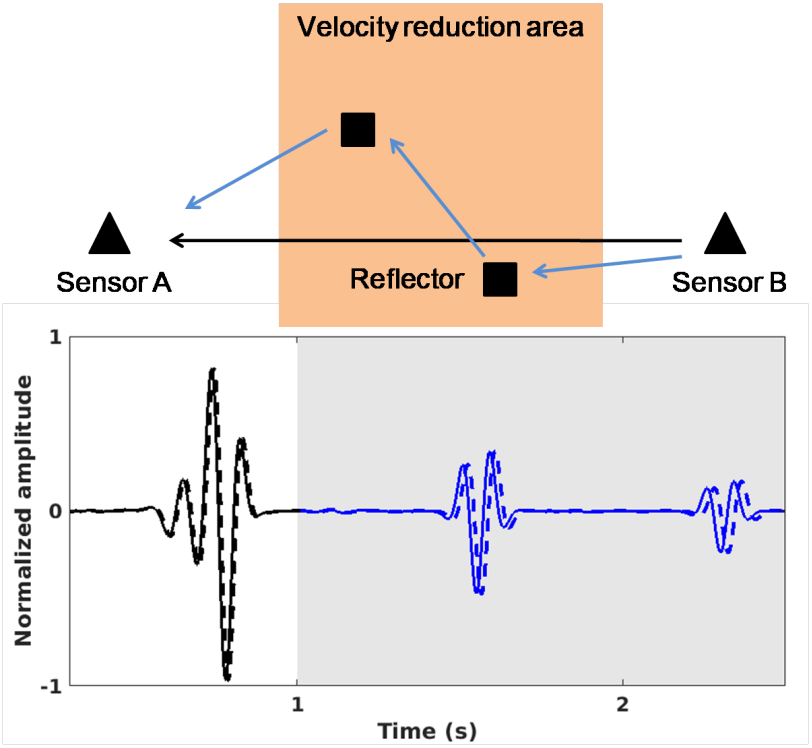

Figure 1.1: A crosscorrelation between ambient seismic noise of two sensors. The black squares indicate structural anomalies (scatterers). The black wiggles indicate a direct wave from sensor B to A directly and is corresponding to the black arrow. The blue wiggles indicate multiply scattered waves and are corresponding to the blue arrow. The dashed waves represent the waves after the velocity reduction.

then isolate/estimate the source information from the crosscorrelaitons (e.g. Ermert *et al.*, 2017). The accuracy of the source information will be determined by many factors, e.g. the accuracy of the subsurface model, the simulation method (ray theory or wave-equation) and the isolation method (imaging or inversion).

One can also use ambient seismic noise to monitor time-lapse changes in the subsurface. In monitoring, one commonly uses coda waves (later arrivals after direct waves) in the crosscorrelations (e.g. Sens-Schönfelder & Wegler, 2006; Brenguier *et al.*, 2008), because coda waves propagate along longer paths and thus are more sensitive to

small subsurface changes than direct waves (Figure 1.1). Monitoring small changes is important for geological hazard early warning. For example, changes in soil saturation can trigger landslides (Iverson, 2000) and thus monitoring the soil stiffness changes can provide a diagnostic signal before the hazard happens (e.g. Mainsant *et al.*, 2012). When imaging small changes in the subsurface, one usually makes assumptions about the wavefield composition (body or surface waves) in the coda (e.g. Obermann *et al.*, 2015). Importantly, three types of body waves (P, SV and SH) exist and interact such as P-to-P, P-to-SV and P-to-SH scattering (e.g. Sato *et al.*, 2012), in addition to interacting with different types of surface waves such as P-to-Rayleigh, SV-to-Rayleigh and SH-to-Rayleigh scattering (e.g. Maeda *et al.*, 2008); these different types of surface waves can also interact with each other such as Rayleigh-to-Rayleigh and Rayleigh-to-Love scattering (Snieder, 1986a). Thus the energy ratio between any two types of waves evolves with time, and studying the interactions is important for imaging of the small changes and applying the time-lapse monitoring method in practice.

My Ph.D. research covers the three ambient seismic areas mentioned above: investigation of subsurface structure, estimation of ambient seismic source distributions and the time-lapse monitoring with coda waves. I divide the chapters in the following ways.

1.1 A comprehensive comparison between the refraction microtremor and seismic interferometry method for phase velocity estimation

This chapter comes from Xu *et al.* (2017) and covers a comparison between two commonly used near-surface (depth<200 m) passive-source surface-wave methods, refraction microtremor (ReMi, Louie, 2001) and seismic interferometry (SI). We identify artifacts in the SI and ReMi methods and explain the origins of these artifacts theoretically. We determine that SI provides a more accurate estimation of surface-wave phase velocities than ReMi.

1.2 On the reliability of direct Rayleigh-wave estimation from multicomponent crosscorrelations

This chapter comes from Xu & Mikesell (2017) and covers estimation of Rayleigh-wave phase velocities from multicomponent crosscorrelations. In the SI method, one commonly uses vertical-component data. However, one can also use radial component data where the radial component is parallel to a line or great circle path connecting two sensors. We refer to the vertical- and radial-component crosscorrelations as multicomponent SI. We observe that the vertical component possesses a same sensitivity to seismic sources in all directions, while the radial component is more sensitive to in-line sources than out-of-line sources. We demonstrate that the multicomponent

crosscorrelations can provide more accurate estimations of Rayleigh-wave phase velocities than the vertical crosscorrelations.

1.3 Rayleigh-wave multicomponent crosscorrelation-based source strength distribution inversion. Part 1: theory and numerical examples

This chapter comes from Xu *et al.* (2019) and covers estimation of seismic source strength distributions by applying the full-waveform inversion theory to Rayleigh-wave multicomponent crosscorrelations. In the full-waveform inversion theory, source sensitivity kernels are necessary for the inversions, and one can derive source sensitivity kernels from different misfit functions. We physically explain two types of source sensitivity kernels: one derived from traveltime misfits and the other from waveform misfits. We then use these kernels to invert for source distributions in synthetic tests. We determine that the waveform misfits provide better estimations of source distributions than the traveltime misfits; we also demonstrate that multicomponent crosscorrelations better constrain the inversion than vertical-component crosscorrelations alone.

1.4 Rayleigh-wave multicomponent crosscorrelation-based source strength distribution inversion. Part 2: a complete workflow for real seismic data

This chapter covers a complete workflow for estimating seismic source distributions from real seismic data through the source inversion in Chapter 4. Although the source inversion theory is well developed, many challenges still exist in real data processing, such as how to select high-quality crosscorrelations, how to isolate targeted sources and how to estimate source spectral densities. Moreover, some processing procedures commonly used in the SI studies of structures are inappropriate for the source estimation method because these procedures can bias the source estimation. We present solutions to the challenges and explain appropriate processing procedures in the workflow. We demonstrate the whole workflow with a field data example from CO_2 degassing in Hartoušov, Czech Republic.

1.5 Estimation of primary microseism source distributions around Antarctica

We apply the whole workflow in Chapter 5 to seismic recordings in Antarctica to estimate the primary microseism source distribution around Antarctica in February 2010. The primary microseism (PM) is due to the interaction between sea currents and the seafloor, and ranges in frequency between 0.04 Hz and 0.09 Hz. Thus, the PM is an important physical phenomenon in ocean studies and provides the signals for

ambient seismic noise tomography. We use the vertical component data and achieve good C_{ZZ} waveform fits from our PM source estimation. We compare our estimation to sea ice data from the same month and observe that our estimated sources are mainly distributed outside of the floating sea ice around Antarctica. This spatial relationship fits the blocking effect of sea ice on microseism generations and deserves further investigations.

1.6 Monte Carlo simulations of multiply scattered body and Rayleigh waves in elastic media

We use a Monte Carlo simulation method to simulate multiply-scattered P and Rayleigh waves in an elastic homogeneous media. This research is helpful for studying the temporal evolution of energy ratios between multiply-scattered body and surface waves in coda waves and thus is important for coda-wave time-lapse monitoring methods. The simulations provide an equipartition energy ratio which matches the theoretical prediction from a homogeneous halfspace. We also incorporate a free surface into the simulation. This research is a first step to a complete modeling of coupled body- and surface-wave multiply scattering in elastic media.

CHAPTER 2:

A COMPREHENSIVE COMPARISON BETWEEN THE REFRACTION MICROTREMOR AND SEISMIC INTERFEROMETRY METHOD FOR PHASE VELOCITY ESTIMATION

This chapter has been published as: Xu, Z., Dylan Mikesell, T., Xia, J., & Cheng, F. (2017). A comprehensive comparison between the refraction microtremor and seismic interferometry methods for phase-velocity estimation. Geophysics, 82(6), EN99-EN108.

2.1 Summary

Passive-source seismic-noise based surface-wave methods are now routinely used to investigate the near-surface geology in urban environments. These methods estimate the shear-wave velocity of the near surface, and two methods that use linear recording arrays are seismic interferometry (SI) and refraction microtremor (ReMi). These two methods process noise data differently and thus can yield different estimates of the surface-wave dispersion, the data used to estimate the shear-wave velocity. In

this paper we systematically compare these two methods using synthetic data with different noise source distributions. We arrange sensors in a linear survey grid, which is conveniently used in urban investigations (e.g. along roads). We find that both methods fail to correctly determine the low frequency dispersion characteristics when out-line noise sources become stronger than in-line noise sources. We also identify an artifact in the ReMi method and theoretically explain the origin of this artifact. We determine that SI combined with array-based analysis of surface waves is the more accurate method to estimate surface-wave phase velocities because SI separates surface waves propagating in different directions. Finally, we propose a solution to eliminate the ReMi artifact that involves the combination of SI and the τ-p transform, the array processing method that underlies the ReMi method.

2.2 Introduction

Geologic hazards in the near surface, such as faults and sink holes, pose large risks to human lives and property. Hence geologic characterization of the near-surface in urban areas is important for accurate hazard assessment. People commonly use ambient seismic noise in geologic investigations (e.g. Shapiro *et al.*, 2005; Pan *et al.*, 2016) because ambient seismic noise contains surface waves, which hold information about the shear modulus of the Earth. Surface waves at different frequencies are used to characterize different scales of Earth structure; 0.02-0.5Hz is used for crustal studies (e.g. Yao *et al.*, 2006; Lin *et al.*, 2008) and 1-5Hz is used for near-surface studies (e.g. Halliday *et al.*, 2008; Cheng *et al.*, 2015). Although 2D arrays provide more accurate phase velocity estimation (e.g. Garofalo *et al.*, 2016), it is often more convenient to use one-dimensional (1D) linear arrays in urban areas, e.g. an array laid along the side of a road. With a linear array, the raw noise data is often processed using the

refraction microtremor (ReMi) method (Louie, 2001) or seismic interferometry (SI) (e.g. Nakata *et al.*, 2011; Cheng *et al.*, 2015). In this paper we compare both of these approaches for 1D arrays, starting with SI.

Seismic interferometry is used to estimate the Green's function between two sensors (Snieder, 2004) from the ambient seismic field. When an array of sensors exists, one can generate a virtual shot record by applying SI to a single sensor (i.e. the virtual source) and all other sensors in the array (e.g. Bakulin & Calvert, 2006). The surface-wave part of the Green's function is most commonly recovered (e.g. Bensen *et al.*, 2007; Lin *et al.*, 2008) because surface waves dominate Earth's ambient seismic field. Seismic interferometry has often been formulated in the time domain and is equivalent to the spatial autocorrelation method (SPAC) in the frequency domain when noise sources are evenly distributed (e.g. Nakahara, 2006; Tsai & Moschetti, 2010; Haney *et al.*, 2012).

When an array is present and virtual shot records are created by SI, the phase-velocity dispersion characteristics of the surface waves, can be estimated by applying array-based velocity analysis (e.g., McMechan & Yedlin, 1981; Song *et al.*, 1989; Park *et al.*, 1998) to the virtual shot record (e.g. Xu *et al.*, 2013). A common array-based method used in surface wave analysis is *multichannel analysis of surface waves* or *MASW* (Park *et al.*, 1999). Array-based methods are used to image the surface-wave dispersion in the frequency-velocity (f-v) domain and are preferred to two station methods because the array helps to distinguish the fundamental mode from higher-mode surface waves (Xia *et al.*, 2003). This distinction is important because higher modes can affect the accuracy of the surface-wave phase velocity measurement (e.g. Luo *et al.*, 2015). For near-surface applications of SI combined with array-based

velocity analysis, we refer the reader to Cheng *et al.* (2015) and Xu *et al.* (2016) and the references therein.

Another approach that uses raw seismic noise to estimate surface wave dispersion is ReMi. This is a 1D array-based method that directly utilizes passive-source surface waves found in the ambient seismic field. The basic idea of ReMi (Louie, 2001) is to apply the τ-p transform (McMechan & Yedlin, 1981) to passive-source surface waves in noise records. The τ-p data are then transformed to the f-v or f-p domain to pick the phase velocity. During the picking, one needs to be careful because the true phase velocity lies somewhere between the coherence maximum and the first increase in coherence above the noise level (e.g. Louie, 2001; Strobbia & Cassiani, 2011). This is different from the array-based methods used in SI, where the maximum coherence in the dispersion image is picked. Because of its simple implementation, the ReMi method has found wide-spread use in engineering applications and near-surface geology surveys (e.g. Scott *et al.*, 2004; Civilini *et al.*, 2016). However, there is no clear theoretical basis for where to pick the phase velocity in the ReMi-derived dispersion image. Moreover, up to now it is not clear which method, SI or ReMi, is more suitable in the urban noise environment.

Although both of these methods assume that noise sources are evenly distributed in space, the processing procedures of the two methods are different, and thus the two methods will likely yield different results. There has been no comprehensive study that compares these two methods. Therefore, we compare these two methods to determine which method more accurately estimates phase-velocity dispersion in the urban noise environment. We compare SI and ReMi for classic noise source distributions in urban areas, where strong noise sources are unevenly distributed and

the recording array is linear. We first introduce the underlying physics of these two methods, and then we apply these two methods to three synthetic data sets and compare results. Results based on the traditional ReMi method show an artifact in this noise environment, which we explain in the *Discussion*. We further the comparison with a field data example, and finally, we compare and contrast the accuracy of the two methods and propose some best practices for the ReMi method.

2.3 Methods

2.3.1 Seismic interferometry and array-based velocity analysis

Researchers have shown that we can accurately recover surface waves by using seismic interferometry both theoretically (Snieder, 2004; Halliday & Curtis, 2008) and in practice (Shapiro *et al.*, 2005; Bensen *et al.*, 2007). In solid-Earth geophysics, researchers usually calculate surface-wave phase velocities with methods that use two stations (e.g. Yao *et al.*, 2006; Lin *et al.*, 2008). In near-surface geophysics, researchers commonly use arrays to calculate surface-wave phase velocities (e.g. Xu *et al.*, 2013). Because near-surface geology is complex, higher-mode surface waves often arise. Array-based methods provide the ability to separate different mode surface waves in the f-v domain (Xia *et al.*, 2003). Thus researchers often combine seismic interferometry and array-based methods to investigate the near-surface geology (e.g. Cheng *et al.*, 2015).

We use crosscorrelation seismic interferometry and array-based velocity analysis in this paper. We crosscorrelate time windows of data and then stack to build virtual shot gathers (e.g. Halliday *et al.*, 2008). We apply velocity analysis directly to these

surface-wave virtual shot gathers, instead of individual empirical Green's functions. We note that there is a constant phase difference of $\pi/2$ between a crosscorrelation and its corresponding empirical Green's function (Snieder, 2004), but the phase difference between two adjacent crosscorrelations remains constant. Velocity analysis is based on phase differences between adjacent channels in a shot gather (Xia, 2014), so it is convenient for us to omit transforming crosscorrelations to empirical Green's functions, either by the Hilbert transform or the derivative of the crosscorrelation function (e.g. Lin *et al.*, 2008; Haney *et al.*, 2012). One can do velocity analysis with different strategies (e.g. McMechan & Yedlin, 1981; Park *et al.*, 1998; Xia *et al.*, 2007; Luo *et al.*, 2008); we use the phase-shift method (Park *et al.*, 1998) to image surface-wave dispersion in this paper. This method is a frequency-wavenumber (f-k) transform applied to a one-dimensional array. The relationship between this method and the more traditional two-dimensional f-k transform is covered in Appendix A.

2.3.2 ReMi

The fundamental method underlying ReMi is the τ-p transform. Because there are passive-source surface waves in the ambient seismic field, one can characterize the surface-wave velocity by applying the τ-p transform along a linear array. The surface waves are assumed to propagate through the array in all directions, and therefore one applies the τ-p transform in two-directions (i.e. forwards and backwards along the linear array), as proposed in the original ReMi method (Louie, 2001). We now present the complete ReMi derivation because this background is needed to discuss the ReMi artifact.

In the ReMi method, the ambient seismic noise data $A(x,t)$ is transformed from the space-time (x-t) domain to the τ-p domain, assuming waves propagate from left

to right across the array, as

$$m_{left}(p,\tau) = \sum_{x_{min}}^{x_{max}} A(x, t = \tau + px), \tag{2.1}$$

where t represents time, x is the offset between a sensor and the first sensor on the left side of the linear array, τ is the zero-offset intercept time, and p is the slowness. We then take the Fourier transform in the τ direction to achieve $m_{left}(p, f)$, where f represents frequency. We repeat the above procedures in the other direction, assuming propagation from right to left, and we sum the power spectra of these two $m(p, f)$ transforms to create $S(p, f)$:

$$S(p,f) = m_{left}(p,f)m^*_{left}(p,f) + m_{right}(p,f)m^*_{right}(p,f), \tag{2.2}$$

where * represents the complex conjugate. We then transform $S(p, f)$ from the p-f domain to f-v domain with the mapping v=1/p. Therefore, the ReMi method actually constitutes a two-direction τ-p transform. This is the common practice (e.g. Scott *et al.*, 2004; Richwalski *et al.*, 2007; Civilini *et al.*, 2016). If only in-line noise sources exist, the energy maximum at each frequency in the f-v domain indicates the real phase velocity (e.g. Strobbia & Cassiani, 2011); however, if out-line noise sources also exist, the energy maximum is an overestimation of the phase velocity (Louie, 2001) (i.e. an apparent velocity). Therefore in practice, one picks the steepest point between the maximum and the departure from the background noise at each frequency (e.g. Louie, 2001; Civilini *et al.*, 2016) to generate a dispersion curve. In this paper, we pick both the steepest point and the maximum when using ReMi for a comparison with the true phase velocity.

Example	N1	N2
1	500	0
2	500	500
3	500	1000

Table 2.1: In-line ($N1$) and out-line ($N2$) noise source number for the three synthetic examples.

2.3.3 Numerical Simulation

We compare the SI and ReMi approaches using three synthetic examples and a field-data example. We introduce the synthetic examples in this section and present the field-data example in a later section. To mimic the urban environment, we consider an uneven noise source distribution in the three synthetic examples. In practice, noise sources are unevenly distributed (Yang & Ritzwoller, 2008; Yao & Van Der Hilst, 2009) and noise commonly occurs on one side of the sensors in urban environments (Nakata, 2016; Cheng *et al.*, 2016). In the first example, noise sources are distributed to the right-side of the linear receiver array in the in-line direction, defined to be in the direction of the linear array. This noise source distribution is commonly observed (e.g. Xu *et al.*, 2016). Because out-line noise sources can also exist, we use both in-line and out-line noise sources in the other two synthetic examples. In the second example, the in-line and out-line noise sources have the same strength, and in the third example, the out-line noise sources are twice as strong as the in-line sources.

We define the in-line and out-line noise sources by their spatial distribution and activation time. The in-line noise sources are randomly distributed within an angle range from -$\pi/12$ to $\pi/12$ (Figure 2.1). The out-line noise sources are randomly distributed within an angle range from $\pi/4$ to $5\pi/12$ (Figure 2.1). We use the number of noise sources as a proxy for the source strength. The number of in-line noise sources

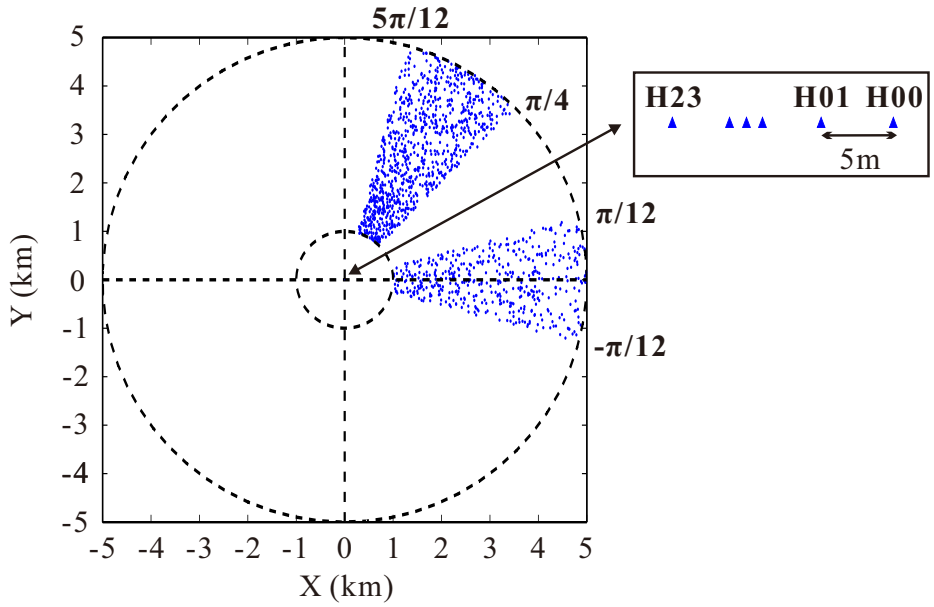

Figure 2.1: This figure illustrates the location of geophones and noise sources. Blue triangles represent geophones near the origin; blue dots represent noise sources. The in-line and out-line noise sources are located away from the origin between 1km and 5km. See text for details about the distribution.

is $N1$, and the number of out-line noise sources is $N2$ (Table 2.1). These in-line and out-line noise sources are randomly activated during a 1-hour recording time.

We adopt the ambient noise numerical simulation method proposed by Lawrence *et al.* (2013) to simulate vertical component data. We model the fundamental-mode Rayleigh waves, and all noise sources emit a 10Hz Ricker wavelet with a 1-s delay from the activation time. The Earth model has two layers (Table 2.2) and is from Bonnefoy-Claudet *et al.* (2006). There are 24 geophones named H00, H01 to H23 (blue triangles arrayed from right to left near the origin in Figure 2.1); the interval between geophones is 5m.

Layer number	Vp (m/s)	Vs (m/s)	Density (g/cm^3)	Thickness (m)
1	1350	200	1.9	25
2	2000	1000	2.5	∞

Table 2.2: The two-layer Earth model parameters used in the simulation.

2.4 Synthetic examples

We apply SI and ReMi to the three synthetic models (Table 2.1). We divide the raw data into 60s windows; we crosscorrelate these windows and stack the crosscorrelations. Then we construct virtual shot gathers (Figure 2.2) and create dispersion images (Figure 2.3a,e,i) by applying phase-shift velocity analysis to the acausal part of these gathers. We also apply ReMi to the entire 3600s of raw data to create dispersion images for each model (Figure 2.3b,f,j).

2.4.1 Example 1

We apply SI and ReMi to calculate surface-wave phase velocities when there are only in-line noise sources (N1=500, N2=0; Figure 2.3a, b). We use SI to create a virtual shot record (Figure 2.2a) and then do velocity analysis. Due to the fact that the in-line noise source distribution does not satisfy the SI requirement that noise sources be evenly distributed around the array, there is a $\pi/4$ phase shift in the in-line noise source Green's function compared to the 3D Green's function when noise sources are distributed evenly (Lin *et al.*, 2008). This phase difference, however, does not adversely affect the velocity analysis (Figure 2.3a) because the phase-shift method measures only phase differences between adjacent geophones, not absolute phase.

In this noise source distribution, the surface waves propagate along the linear sensor array (Figure 2.1) from right to left only. In this situation, the wave propagation satisfies the τ-p transform assumption that a plane wave travels along the

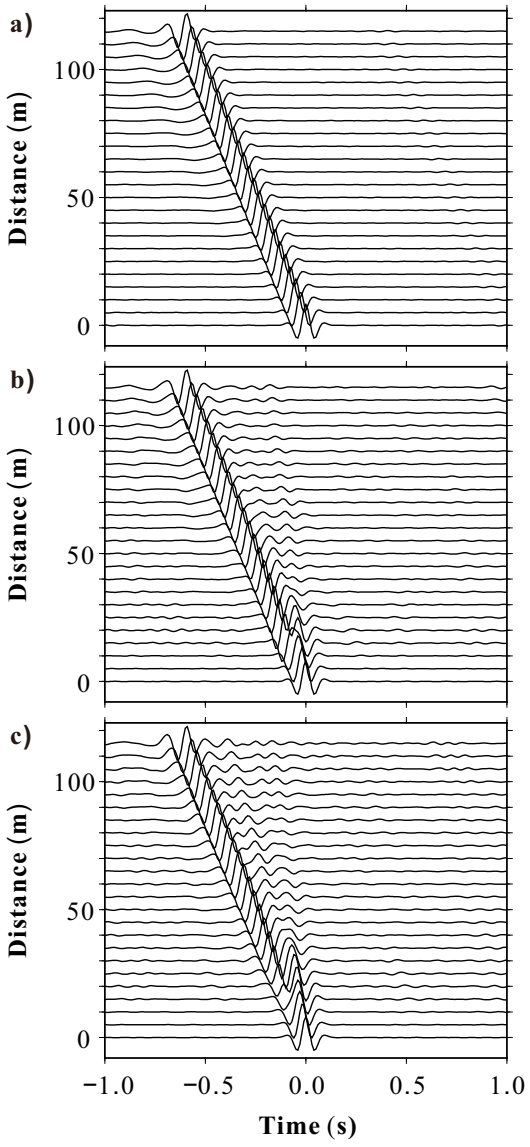

Figure 2.2: The virtual shot gathers for each synthetic source distribution model (Table 2.1). a) N1=500, N2=0; b) N1=500, N2=500; c) N1=500, N2=1000. We crosscorrelate station H0 with all other stations, H1 to H23. As the out-line sources increase in strength, artifacts begin to appear in the virtual shot gathers with fast apparent velocities.

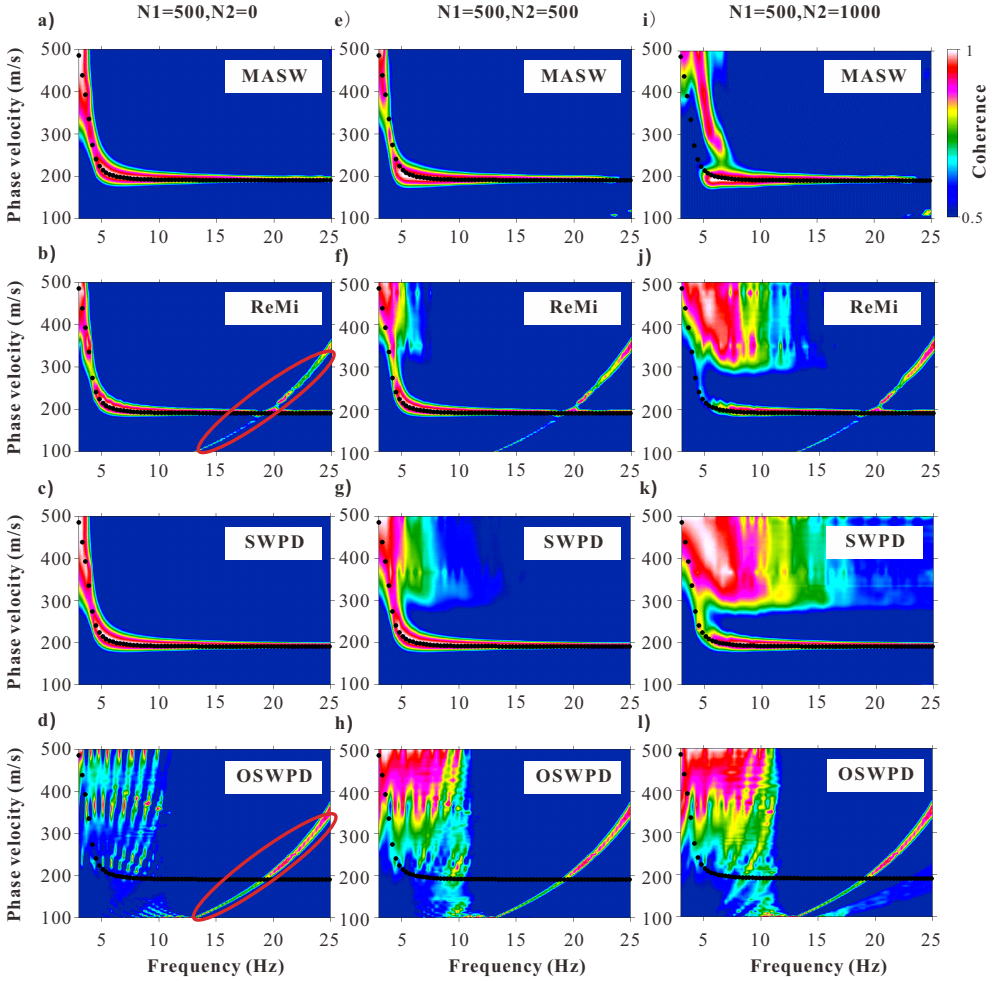

Figure 2.3: Dispersion images for the three synthetic examples (Table 2.1). We apply velocity analysis to the virtual shot gathers using the phase-shift method (Park *et al.*, 1998) to create a,e,i (seismic interferometry velocity analysis, SIVA). We apply ReMi to the raw synthetic data to create b,f,j. We use surface-wave propagation-direction (SWPD) ReMi to create c,g,k, and we use opposite surface-wave propagation-direction (OSWPD) ReMi to create d,h,l. Red ellipsoids in b and d highlight the artifact. Black dots represent theoretical Rayleigh-wave phase velocities (Haskell, 1953). All dispersion images in this paper are normalized per frequency.

linear array; therefore, the true surface-wave phase velocity is given by the maximum of the dispersion trend (Figure 2.3b) in the f-v domain. However, there is an artifact in the ReMi result (indicated by the red ellipsoid in Figure 2.3b). We note that we applied the τ-p transform in two directions, from right to left and from left to right (Equation 2). Thus the dispersion image is a combination of these two τ-p transforms. To investigate this artifact, we present these two transform results separately (Figure 2.3c,d). We find that if we only use ReMi in the surface-wave propagation direction, from right to left here, we observe the correct energy trend in the f-v domain without the artifact (Figure 2.3c). The artifact only exist when we apply ReMi from left to right, which is opposite the actual surface-wave propagation direction (Figure 2.3d). From here on, we call these two one-direction ReMi methods "surface-wave propagation-direction (SWPD) ReMi" and "opposite surface-wave propagation-direction (OSWPD) ReMi". We theoretically explain the reason this artifact exists in the *Discussion*; prior to this we will finish the investigation of the noise source distribution.

2.4.2 Example 2

In the model with out-line noise sources (N1=N2=500), the dispersion image (Figure 2.3e) is extremely similar to the previous model (Figure 2.3a). This is because the stationary-phase sources (Snieder, 2004) still dominate the virtual source reconstruction. The noise sources in the stationary-phase zone constructively interfere for the surface waves (e.g. Yao & Van Der Hilst, 2009), and hence we reconstruct clear surface waves in the virtual shot gather (Figure 2.2b). We note that there are also weak high-velocity waves in this virtual shot gather due to incomplete cancellation over the truncated out-line and in-line noise source distributions. These high-velocity

waves appear as spurious energy in the f-v domain, but this energy trend is weak and lower than the amplitude threshold we apply in Figure 2.3. Thus the trend does not appear in the f-v domain plot.

The dispersion estimate from ReMi is not as clear as SI over the low frequencies. The energy trends in ReMi (Figure 2.3f,g) show higher velocities than the theoretical surface-wave phase velocities. This difference is due to the out-line surface waves (Louie, 2001). Moreover, the velocity difference increases as frequency decreases, and the dispersion energy smearing increases as the frequency decreases. At frequencies less than 5Hz, the energy trends are smeared and considerably less focused compared to the SI result (Figure 2.3e). There are also identical artifacts in the ReMi and the OSWPD ReMi results (Figure 2.3f,h).

2.4.3 Example 3

We begin to observe a more biased surface-wave phase velocity trend when the out-line noise source strength increases beyond the in-line sources; here we model the out-line noise as two times the in-line noise strength (N1=500, N2=1000). The high-velocity waves in the virtual shot gather (Figure 2.2c) increase in amplitude, and after we apply velocity analysis to the virtual shot gather, a spurious energy trend appears at frequencies less than 5 Hz in the f-v domain (Figure 2.3i). This energy trend shows a shift toward higher velocities. The correct surface-wave dispersion trend does actually exist, but the trend is too weak to pass the amplitude threshold we apply to the image. In this case, one would misidentify phase velocities at low frequency if the maximum energy in the dispersion image is used to determine the pick. Thus it is difficult to calculate correct surface-wave phase velocities for frequencies less than 5Hz. We will discuss further why the spurious energy trend is strong in the *Discussion*. In

the ReMi method, the energy trend becomes even more smeared than in Example 2 due to the stronger out-line noise sources. Thus one will also pick inaccurate phase velocities for the low frequencies in the ReMi results. The artifact also exists in the ReMi and OSWPD ReMi results (Figure 2.3j,l).

2.4.4 Phase velocity dispersion errors

In order to quantify the accuracy of the two methods in our synthetic examples we calculate the average error between the picked phase velocities and the theoretical values (black dots in Figure 2.3). We pick phase velocities as 1) the maximum energy in the SI dispersion images, 2) the maximum energy in the ReMi dispersion images and 3) the largest gradient (i.e. steepest point) along a single frequency in the ReMi dispersion images. We use two methods for ReMi so as to compare with previous literature (e.g. Louie, 2001). We compute the error as

$$\epsilon = \frac{1}{N}\sum_{i}^{N}\frac{|c(f_i) - c_{theory}(f_i)|}{c_{theory}(f_i)}, \tag{2.3}$$

where N is the number of the picked phase velocities, $c(f_i)$ is the picked phase velocity at frequency f_i, and $c_{theory}(f_i)$ is the theoretical value. We calculate the error between 3-5Hz and then all frequencies (3-25Hz, Table 2.3) because the energy trend fits the theoretical values above 5Hz in all examples.

In the case of only in-line noise (Example 1), SI, ReMi (maximum) and SWPD ReMi (maximum) give accurate ($\epsilon < 5\%$) phase-velocity estimates below 5Hz. The small error that we do observe is due to the limited receiver-array aperture. ReMi (steepest) and SWPD ReMi (steepest) provide phase velocities with large error ($\epsilon > 20\%$) because the steepest-point picking rule (Louie, 2001; Civilini *et al.*, 2016) is not appli-

Method	N1=500 N2=0	N1=500 N2=500	N1=500 N2=1000
	(3-5Hz / 3-25Hz)	(3-5Hz / 3-25Hz)	(3-5Hz / 3-25Hz)
SI (maximum)	3.44 / 1.35	10.51 / 2.60	74.92 / 3.05
ReMi (maximum)	4.23 / 5.12	16.13 / 7.92	86.88 / 29.55
ReMi (steepest)	21.45 / 9.51	15.19 / 9.50	15.55 / 10.67
SWPD (maximum)	2.53 / 1.16	14.46 / 1.75	91.95 / 14.72
SWPD (steepest)	28.21 / 8.47	22.60 / 7.16	22.31 / 6.95

Table 2.3: The average error (ϵ) between the picked phase velocities and the theoretical values (black dots in Figure 2.3) below 5Hz (left) and between 3Hz to 25 Hz (right). We calculate the error with Equation 2.3 in percentage. SWPD represents the surface-wave propagation-direction ReMi.

cable in this case. The maximum of the τ-p transforms defines the true velocity. We neglect computing the error in OSWPD ReMi because the artifact is entirely wrong. In the case of equal strength in-line and out-line sources (Example 2), the SI approach results in smaller average errors than any of the ReMi approaches. This is due to the ability of SI to focus the wavefield in the virtual shot record prior to creating the f-v domain image, in essence suppressing the spurious energy that has a fast apparent velocity. When the noise sources are dominantly out-line (Example 3), we observe that SI, ReMi (maximum) and SWPD ReMi (maximum) have large errors below 5Hz; however, ReMi (steepest) and SWPD ReMi (steepest) provide results with smaller errors, which demonstrates the initial reasoning of the steepest-point picking approach. In this case, no 1D velocity analysis method can provide accurate phase velocities in the lower frequencies, which is critical to constrain deep area shear velocities (Louie, 2001). Finally, the artifact in ReMi affects the auto-picking process and explains why the averaged errors in the SWPD results are smaller than the ReMi results over the entire frequency band (Table 2.3).

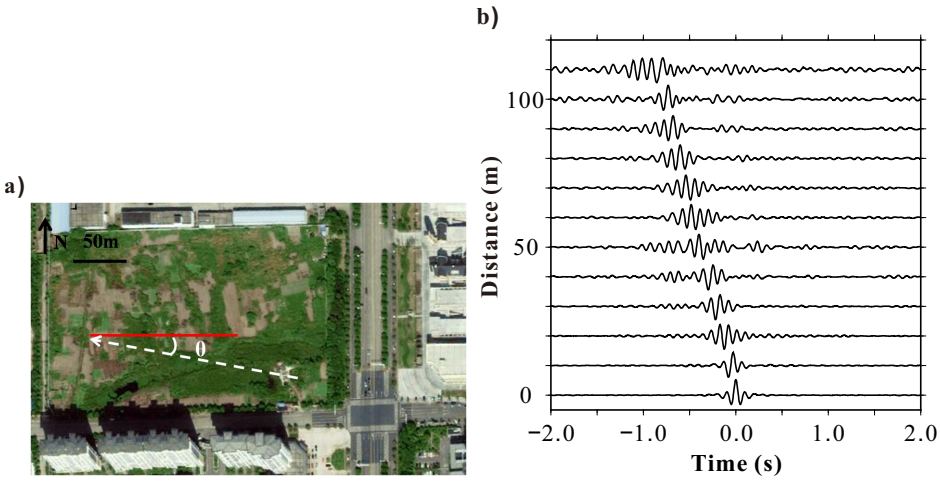

Figure 2.4: a) Map of the experiment field. The field is near roads. The red line represents the geophone array. The white dashed arrow represents the dominate ambient seismic noise energy propagation direction (Cheng *et al.*, 2016); θ is the angle between the ambient seismic energy propagation direction and the array.b) The virtual source is the geophone on the far right of the array.

2.5 A field-data example

We acquired ambient seismic noise data in the city of Nantong, China. We placed twelve 2.5 Hz vertical-component geophones along with RefTek digitizers in a linear array (the red solid line in Figure 2.4a). The sampling rate is 500Hz, and the interval between two adjacent geophones is 10m. The line is almost perpendicular to a main road, and beamforming results indicate that the angle (θ) between the dominate passive-source surface-wave propagation direction and the receiver line is less than $\pi/6$ (Cheng *et al.*, 2016). We divided the 2-hours of raw data into 60s windows; then we removed the mean and linear trend in each window. We crosscorrelated every window of the right-most geophone and the other geophones and then stacked the crosscorrelations. The acasual part of this virtual shot record (Figure 2.4b) is

Method	ϵ (%)
SI (maximum)	2.85
ReMi (maximum)	36.18
ReMi (steepest)	5.27
SWPD (maximum)	10.89
SWPD (steepest)	7.87

Table 2.4: The errors associated with the picked phase velocities (Figure 2.5a,b,c). We calculate the error (ϵ) with Equation 2.3 in percentage and use the Cheng *et al.* (2016) velocities as the theoretical values. SWPD represents the surface-wave propagation-direction ReMi.

dominated by a single surface wave mode. This asymmetric virtual shot record further confirms that most of the passive-source surface waves propagated along the array from right to left, as indicated by the beamforming.

We create dispersion images from the acausal part of the virtual shot gather (Figure 2.4b) with the phase-shift method and by applying ReMi to the raw data. Seismic interferometry provides a more focused energy trend (Figure 2.5a) than ReMi (Figure 2.5b,c,d) and results in a smaller error than ReMi (Table 2.4). Here we use phase velocities corrected for the noise source distribution (Cheng *et al.*, 2016) as the theoretical velocity values in the error estimation. The artifact (indicated by the red ellipsoid in Figure 2.5b) also exists in the ReMi results (Figure 2.5b,d). The artifact, however, does not exist in the SWPD ReMi result (Figure 2.5c). Hence the SWPD ReMi result provides a cleaner and more continuous energy trend in the f-v domain than the traditional ReMi method and results in reduced error (Table 2.4).

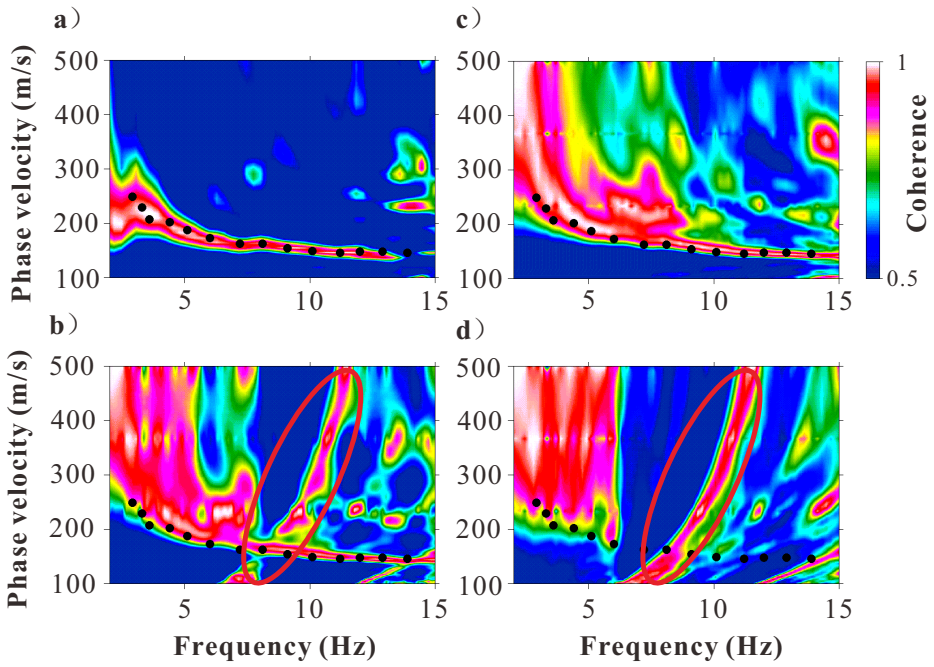

Figure 2.5: Surface-wave dispersion images based on ambient noise data recorded in Nantong, China. a) We apply the phase-shift method to the acausal virtual shot gather (Figure 2.4b). We also apply ReMi (b), SWPD ReMi (c) and OSWPD ReMi (d) to the raw data. The energy trends in a,b,c represent the Rayleigh wave. Two red ellipsoids indicate the artifact. Black dots represent source-corrected Rayleigh-wave phase velocities from Cheng *et al.* (2016).

2.6 Discussion

2.6.1 The spurious energy in seismic interferometry

Spurious energy in the virtual shot record begins to dominate in the f-v domain when the out-line sources are stronger than the in-line sources (N1=500, N2=1000, Figure 2.3i). We observe that this dominance occurs at frequencies less than 5Hz, and we explain this observation based on the noise source contributions in the framework of SI. We first introduce the Green's function that is recovered from noise, where the far-field approximation to the surface-wave Green's function in a laterally homogeneous media can be written as

$$G(H_A, H_B, \omega) - G^*(H_A, H_B, \omega) \approx \frac{j}{4\pi\rho} \int_0^{2\pi} e^{j\omega r cos\theta/c} d\theta, \tag{2.4}$$

where H_A and H_B are the two sensors being crosscorrelated, r is the distance between these two sensors, j is the imaginary unit, ω is angular frequency, θ is the noise source angle and c is the surface-wave phase velocity (Fan & Snieder, 2009). $G(H_A, H_B, \omega)$ is the causal Green's function and $G^*(H_A, H_B, \omega)$ is the acasual Green's function. Here $rcos\theta$ is an apparent distance, and $\omega rcos\theta/c$ indicates the surface-wave phase at ω due to noise sources distributed in the angle θ.

Surface-wave signals in crosscorrelations or empirical Green's functions come from coherent noise sources (Xu *et al.*, 2013). The phase of these surface-wave signals is determined by the distance difference between the noise source and the two sensors, H_A and H_B. Hence, noise source locations with the same phase lie along hyperbolas with foci at these two sensors. In the far field, these hyperbolas approximate straight lines (Figure 2.6). Noise sources in the $2N\pi$ iso-phase hyperbolas (blue lines

in Figure 2.6) are maximums in the real part of the integrand in Equation 2.4 (Figure 2.7); noise sources in the $(2N+1)\pi$ iso-phase hyperbolas (red lines in Figure 2.6) are minimums in the real part of the integrand in Equation 2.4 (Figure 2.7). Noise source energy along different angles will destructively interfere and cancel when the real (and imaginary) part of the integrand oscillates rapidly (Fan & Snieder, 2009). When the out-line energy in our synthetic examples lies in these zones of oscillation, these sources cancel each other in SI and the energy is not present in the virtual shot records, nor in the f-v domain. Hence, there is frequency-dependent spurious energy.

When the frequency is less than 5Hz, the hyperbolas in the out-line direction are sparser, or more separated, than at high frequencies (Figure 2.6), and the real part of the integrand does not oscillate as quickly (Figure 2.7a). Therefore some out-line noise energy remains after applying SI. We attribute the spurious energy trends in frequencies less than 5Hz (Figure 2.3i) to this slow oscillation of the phase. As the frequency increases, the iso-phase hyperbolas become more dense (Figure 2.6b,c), which means the real part of the integrand oscillates more rapidly (Figure 2.7b,c). As a result, the cancellation of out-line noise energy will be more effective, and there is no spurious energy trend at frequencies above 5Hz (Figure 2.3f).

2.6.2 The artifact in ReMi

We find that, even in the simplest case of in-line noise sources, there is artifact in the dispersion image when we apply the traditional two-direction ReMi method (Figure 2.3b, f and j). This artifact is also present in almost all other published work and has been interpreted as f-k aliasing (e.g. Louie, 2001), but as evident in our analysis, this artifact only exists because we adopt ReMi in the opposite surface-wave propagation direction (Figure 2.3d, h and l). If we apply ReMi in only the surface-

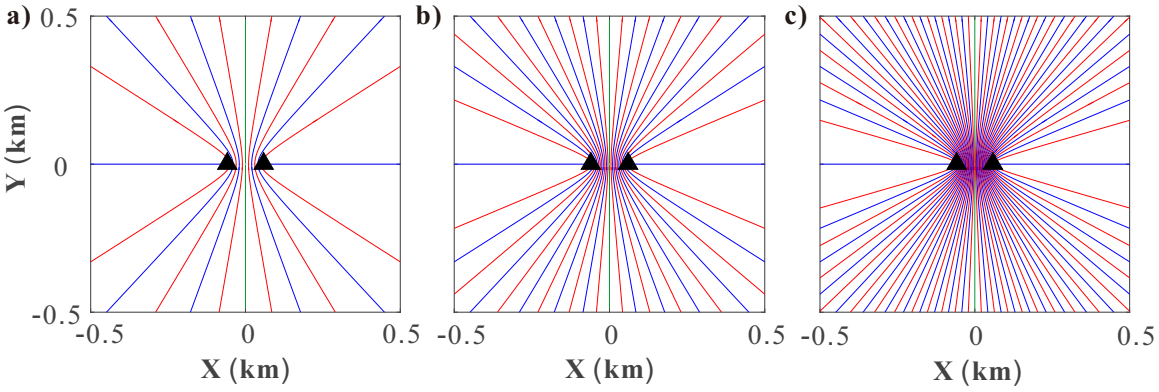

Figure 2.6: Three examples of iso-phase hyperbola for three different frequencies: a) 5Hz, b) 10Hz and c) 20Hz. Red lines represent $(2N-1)\pi$ phase; blue lines represent $2N\pi$ phase ($N = 1, 2, 3\ldots$). Here the surface-wave phase velocity is 200m/s. The two black triangles represent the two sensors. The distance between these two sensors is 120m. One is located in X=60m, Y=0; the other is located in X=-60m, Y=0.

wave propagation direction, the artifact does not exist (Figure 2.3c, g and k). Thus, we investigate this artifact further to determine the origin as it pertains to ReMi theory.

We first present the τ-p transform in the frequency domain. We transform Equation 2.1 to the frequency domain:

$$m(p,f) = \int m(p,\tau)e^{-j2\pi f\tau}d\tau = \sum_{x_{min}}^{x_{max}} \int d(x, t=\tau+px)e^{-j2\pi ft}e^{j2\pi fpx}dt, \qquad (2.5)$$

where d represents a (virtual) shot gather and we have interchanged the order of the summation and the integral. Evaluating the integral leads to

$$m(p,f) = \sum_{x_{min}}^{x_{max}} d(x,f)e^{j2\pi fpx}. \qquad (2.6)$$

Equation 2.6 is the basic equation for the phase-shift method (Park *et al.*, 1998). Thus

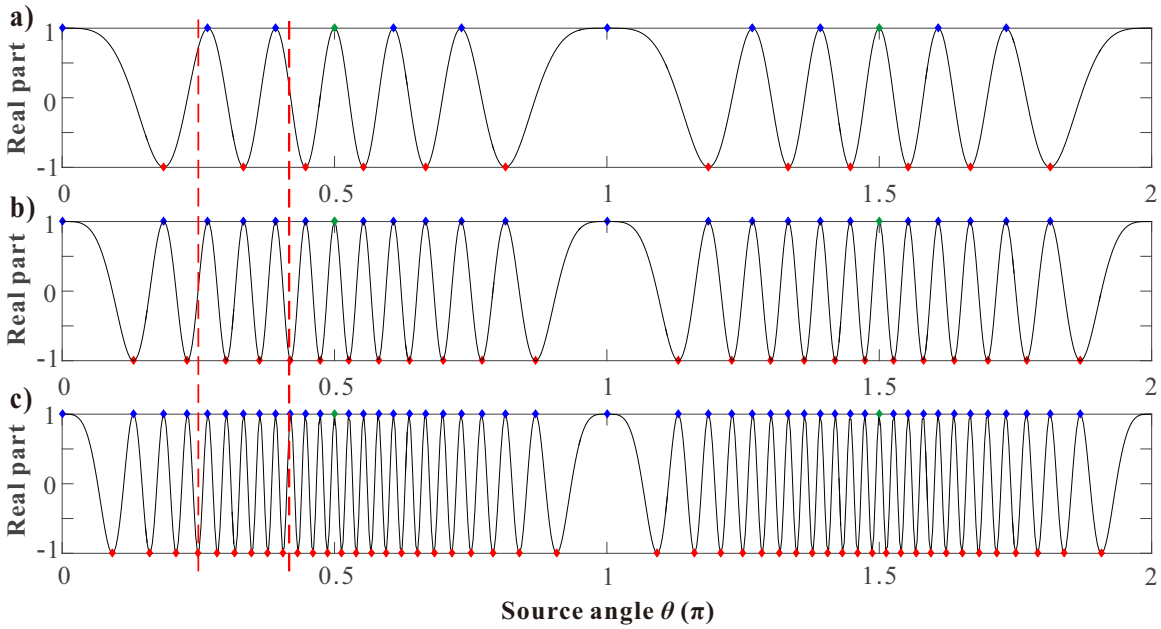

Figure 2.7: The real part of the integrand in Equation 2.4 for the three frequencies in Figure 2.6: a) 5Hz, b) 10Hz and c) 20 Hz. Surface-wave phase velocities are all 200m/s. Blue diamonds represent the sources on blue iso-phase hyperbola in Figure 2.6; green diamonds correspond to green lines in Figure 2.6; red diamonds represent the sources on red iso-phase hyperbola in Figure 2.6. Red dash lines represent the angle range for out-line noise sources, from $\frac{\pi}{4}$ to $\frac{5\pi}{12}$.

the τ-p transform has as good resolution as the phase-shift method (Shen *et al.*, 2015). We will use this spectral f-p equation (Equation 2.6) in the remaining discussion.

We focus here only on the surface-wave phase in the dispersion measurement (Park *et al.*, 1998; Xia, 2014), and thus we neglect the amplitude part in d so that

$$d(x, f) = e^{j(\phi_0 - 2\pi f p_0 \Delta x)}, \tag{2.7}$$

where ϕ_0 represents initial phase, x represents the receiver location, $\Delta x = x - x_0$ is the source-receiver offset, where x_0 is the source location (often 0), and p_0 represents the surface-wave slowness at frequency f. This gives the correct phase for a surface wave propagating from x_0 to x; we note that if the surface wave propagates in the other direction, Δx in Equation 2.7 becomes $\Delta x = x_{max} - x$. If we apply the spectral f-p equation to a (virtual) shot gather in the direction opposite to the actual surface-wave propagation direction, Equation 2.6 becomes

$$m(p, f) = \sum_{x_{min}}^{x_{max}} e^{j(\phi_0 - 2\pi f p_0 (x_{max} - x))} e^{j2\pi f p x} = e^{j(\phi_0 - 2\pi f p_0 x_{max})} \sum_{x_{min}}^{x_{max}} e^{j2\pi f x (p + p_0)}, \tag{2.8}$$

where $e^{j(\phi_0 - 2\pi f p_0 x_{max})}$ is a constant value for the gather. Equation 2.8 is the equation of the artifact, and this artifact in the τ-p transform leads to the artifact in the traditional two-directional ReMi method.

Because the sensors in a linear array are commonly distributed at the same spatial interval, Equation 2.8 can be rewritten as:

$$m(p, f) = e^{j(\phi_0 - 2\pi f p_0 x_{max})} \sum_{n=1}^{N} e^{j2\pi f (n-1) dx (p + p_0)}, \tag{2.9}$$

where N is the number of the sensors and dx is the receiver spacing. If $dx(p+p_0) = 1/f$, Equation 2.9 reduces to $m(p,f) = e^{j(\phi_0 - 2\pi f p_0 x_{max})}$, which is a maximum in the dispersion image. Moreover, the artifact will appear not only when $dx(p+p_0)$ is equal to $1/f$, but also when $dx(p+p_0)$ is equal to any integer times $1/f$. This artifact was recognized by Turner (1990) in wave records (Figure 2.8). To demonstrate that this is indeed the equation of the artifact, we applied both the τ-p and the phase-shift methods to the acausal virtual shot record in Example 1 (Figure 2.2a), but in the direction opposite the actual surface wave propagation direction. We also compute the artifact using Equation 2.8 and compare the results to two virtual shot record examples (Figure 2.9). The artifact is identical in all three images, although we see variations in amplitude. Besides this artifact, the results of the τ-p and the phase-shift methods are not identical due to stacking in different domains.

2.6.3 Improvements to the SI and ReMi Methods

The spurious waves in SI and the artifact in ReMi arise from a lack of knowledge about noise-source distribution, and the smearing in the f-v domain when the noise sources are stronger from the out-line direction all lead to frequency dependent bias in phase velocity estimates from 1D arrays. Park & Miller (2008) present a solution to this problem whereby they scan over all azimuths to account for apparent velocities of out-line energy propagating across the 1D array. Using two-dimensional (2D) arrays, the source direction(s) can actually be determined, and this has been done in f-k analysis applied to ReMi (e.g. Strobbia & Cassiani, 2011) and SI (e.g. Nakata *et al.*, 2016). If one can determine the source angle with f-k analysis, then a correction can be made to the phase velocity to correct any bias (e.g. Cheng *et al.*, 2016). Alternatively, if one knows that both out-line and in-line noise sources exist, one can mute the spurious

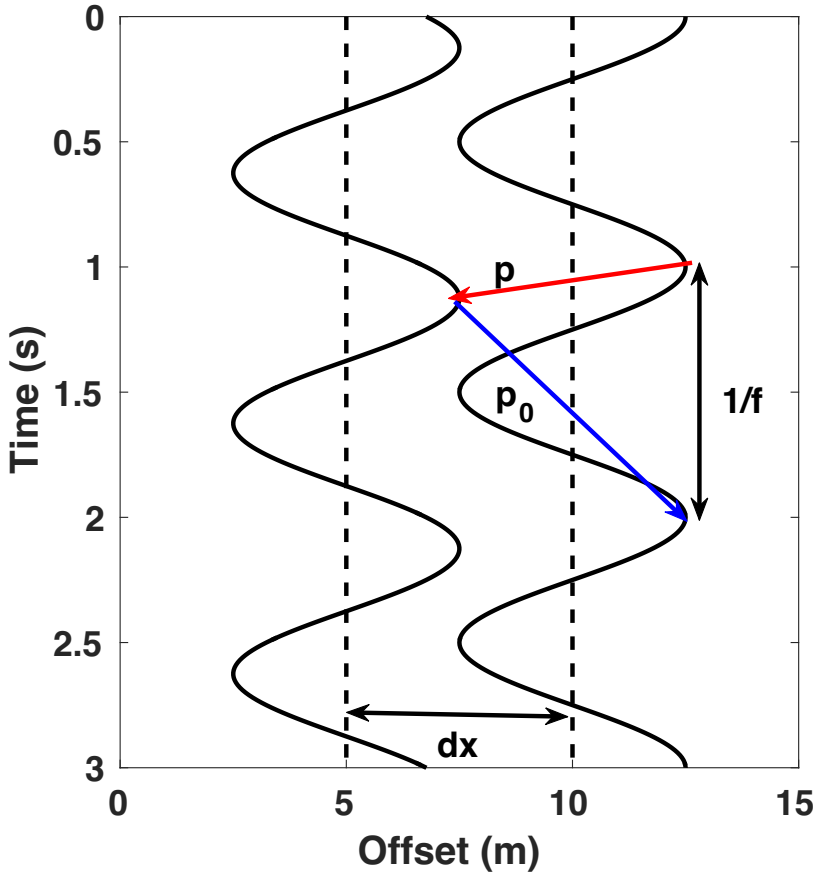

Figure 2.8: An illustration of the artifact in ReMi. For a monochromatic wave (T=$1/f$) recorded on two receivers separated by distance dx, multiple slowness values will sum constructively during velocity analysis. A slowness value of zero would be represented by a horizontal line. Here, the blue line represents a positive slowness value (p_0), which is in the actual surface-wave propagation direction. The red line represents a negative slowness (p), or conversely, a slowness in the direction opposite to the actual surface-wave propagation direction. Both slowness values would have high amplitudes in the f-p domain, but only p_0 would be real.

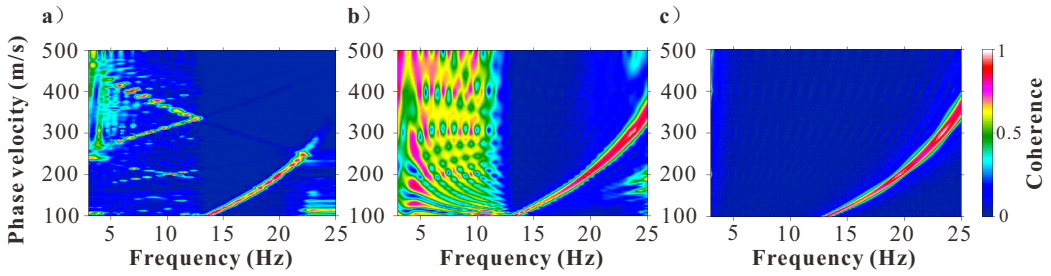

Figure 2.9: a) We apply the τ-p transform to the acausal virtual shot gather (Figure 2.2a) in the direction opposite the surface-wave propagation direction. b) We also apply the phase-shift method in that direction. c) We plot Equation 2.8 in the f-v domain with the same discretization as in a) and b).

waves in the crosscorrelations (Figure 2.2c) prior to velocity estimation. Or if multi-component data exists, the spurious waves in SI (Figure 2.3i) can be suppressed if one applies SI to the radial components, which are more sensitive to in-line noise sources than out-line noise sources compared to vertical components (Xu & Mikesell, 2017). Finally, it is worth noting that a separate problem arises when sources lie near the linear recording array and the incident plane wave assumption is not valid. A solution to this is given by Park & Miller (2008), whereby a cylindrical wave f-v transform is used rather than a plane wave transform. Even in this instance though, biases remain at low frequencies due to the influence of non-stationary phase noise sources.

Regarding the ReMi artifact, if one knows that noise sources are only distributed to one side of the geophone array, one can avoid the artifact in ReMi by applying ReMi only in the surface-wave propagation direction instead of both directions. In this study we use crosscorrelations, not f-k analysis, to identify the surface-wave propagation direction (Figure 2.2,2.4b) and to separate the left- and right-going wavefields. Therefore, with ReMi and the surface-wave propagation direction taken from crosscorrelations, the artifact can be eliminated to improve continuity of the entire

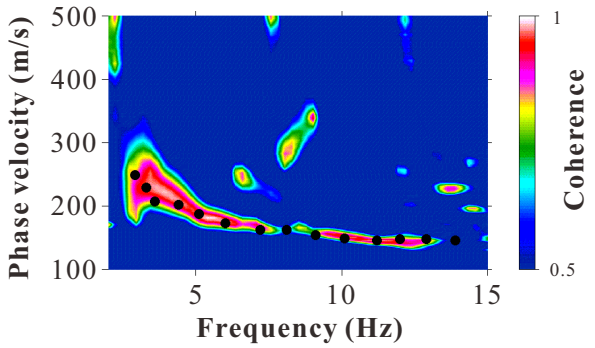

Figure 2.10: The τ-p transform applied to the virtual shot gather in Figure 2.4b in the direction of surface-wave propagation. We achieve a surface-wave dispersion image that is similar to the phase-shift result (Figure 2.5a). Black dots represent the surface-wave phase velocities from Cheng *et al.* (2016).

dispersion image (Figure 2.3c,g,k,2.5c). If noise sources are distributed on both sides of the array, in order to eliminate the ReMi artifact, one must first separate left and right propagating waves and then apply the τ-p transform. Seismic interferometry acts to separate the surface waves into the causal and acausal parts, depending on left or right propagation directions, respectively. Therefore we can apply the ReMi or the τ-p transform directly to the casual or acasual part of crosscorrelations that contains strong surface waves (Figure 2.4b) instead of raw noise records. Because we have demonstrated that the τ-p transform (McMechan & Yedlin, 1981) in the frequency domain is equivalent to the phase-shift method (Park *et al.*, 1998), one should expect to achieve very similar dispersion images using either the τ-p (Figure 2.10) or phase-shift (Figure 2.5a) methods, which indeed is the case. However, ambiguity remains as to whether one should pick the maximum or the steepest point in the energy increase in the f-v domain. Choosing the steepest point appears to work sometimes and other times not. Therefore, in the case that only a linear array is available, we suggest SI followed by phase-shift or τ-p velocity analysis applied to the side of the virtual

shot record with the dominant surface wave energy. In this way, SI first gathers the coherent energy from the stationary-phase sources, and then the maximum in the dispersion image can be picked, avoiding this ambiguity in the ReMi method.

2.7 Conclusion

We compare two approaches that use linear recording arrays to estimate surface-wave phase-velocity dispersion from passive noise sources. We identify limitations in the accuracy of estimation when the surface waves are generated by non-uniformly distributed passive sources. This noise source distribution is meant to mimic the highly heterogeneous source distribution one might find in an urban setting during near-surface shear-wave velocity estimation experiments. We determine that accurate surface-wave phase velocities can be estimated with SI and array-based velocity analysis if out-line noise sources are not stronger than in-line noise sources. The SI derived results provide more focused energy trends in the f-v domain and smaller errors than the results of traditional ReMi. Therefore we recommend to use seismic interferometry and array-based velocity analysis in this noise environment. We also identify an artifact in the dispersion image if the traditional two-direction ReMi method is applied to the data. This is regardless of the noise source direction, and to avoid this artifact, one needs to determine the main passive-source surface-wave propagation direction and then apply the surface-wave propagation-direction ReMi. Otherwise, one can first separate the left and right propagating surface wavefields with SI and then apply velocity analysis independently to the causal and acausal virtual shot gathers. Either the τ-p or the phase-shift method can be applied during velocity analysis; we have shown that the two are equivalent.

CHAPTER 3:

ON THE RELIABILITY OF DIRECT RAYLEIGH-WAVE ESTIMATION FROM MULTICOMPONENT CROSSCORRELATIONS

This chapter has been published as: Xu, Z., & Mikesell, T. D. (2017). On the reliability of direct Rayleigh-wave estimation from multicomponent cross-correlations. Geophysical Journal International, 210(3), 1388-1393.

3.1 summary

Seismic interferometry (SI) is routinely used to image and characterize underground geology. The vertical component crosscorrelations (C_{ZZ}) are often analyzed in this process; although one can also use radial component and multicomponent crosscorrelations (C_{RR} and C_{ZR}, respectively), which have been shown to provide a more accurate Rayleigh-wave Green's function than C_{ZZ} when sources are unevenly distributed. In this letter we identify the relationship between the multicomponent crosscorrelations(C_{ZR} and C_{RZ}) and the Rayleigh-wave Green's functions to show another point of view as to why C_{ZR} and C_{RR} are less sensitive than C_{ZZ} to the non-stationary phase source energy. We demonstrate the robustness of C_{RR} with a synthetic seismic noise data example. These results provide a compelling reason as

to why C_{RR} should be used to estimate the dispersive characteristics of the direct Rayleigh wave with SI when the signal-to-noise ratio is high.

3.2 Introduction

Characterizing underground geological structure is important for a variety of applications (e.g. geological hazard assessment, resource exploration, contaminant monitoring, etc.). Nowadays one commonly uses seismic interferometry (SI) to characterize elastic and anelastic properties of the subsurface. Vertical component (Z) data are often used to compute C_{ZZ} crosscorrelations (e.g. Shapiro *et al.*, 2005), where C_{ZZ} indicates that the vertical channel at both stations is used. From C_{ZZ}, one can estimate an approximate fundamental-mode Rayleigh-wave Green's function (G_{ZZ}) if the seismic sources are distributed evenly (Snieder, 2004; Roux *et al.*, 2005) or if the wavefield is diffuse (Lobkis & Weaver, 2001; Weaver & Lobkis, 2006). However, seismic sources are usually not evenly distributed, nor is the wavefield diffuse (Mulargia, 2012), and C_{ZZ} leads to a biased estimate of G_{ZZ} (e.g. Halliday & Curtis, 2008; Yao & Van Der Hilst, 2009; Froment *et al.*, 2010). One can correct the biased G_{ZZ} using multi-dimensional deconvolution (Wapenaar *et al.*, 2011), the C^3 method (Stehly *et al.*, 2008; Froment *et al.*, 2011), information about the source distribution (e.g. Yao & Van Der Hilst, 2009; Nakata *et al.*, 2015), or signal processing methods (e.g. Baig *et al.*, 2009; Stehly *et al.*, 2011; Melo *et al.*, 2013). One can also use radial component (R) data to retrieve G_{RR} or a combination of vertical and radial components to retrieve G_{ZR} (e.g. Campillo & Paul, 2003; Lin *et al.*, 2008; Stehly *et al.*, 2009), where the R direction is the in-line direction between the two receivers. van Wijk *et al.* (2011) (empirically) and Haney *et al.* (2012) (theoretically) determined that C_{ZR} and C_{RZ} are less sensitive than C_{ZZ} to out-of-line sources, where out-of-line sources mean the

non-stationary phase sources. Stationary-phase sources are defined as sources that constructively interfere to produce the Green's function during correlation; these are sources that have an absolute phase difference less than $\pi/4$ when compared to the real Green's function.

In this letter, we investigate the reliability of crosscorrelations affected by an uneven source-energy distribution. Truncating the boundary of sources in seismic interferometry leads to coherent noise (i.e. artifacts or spurious arrivals) (e.g. Snieder *et al.*, 2006; Mikesell *et al.*, 2009). We investigate why C_{ZR} and C_{RR} are more robust than C_{ZZ} to estimate the fundamental-mode Rayleigh wave from a theoretical standpoint and determine why previous studies often find that C_{ZZ} has the largest signal-to-noise ratio (SNR). We first review the relationship between the fundamental-mode Rayleigh-wave Green's function and the crosscorrelation function. We then analyze how the source-energy distribution contributes to the crosscorrelation and the estimate of the Green's functions. We find that C_{ZR} and C_{RR} attenuate the non-stationary phase source energy and provide more reliable Rayleigh-wave Green's functions than C_{ZZ}. We further the discussion with a synthetic data example where seismic noise sources are unevenly distributed. We consider how the uneven noise-source distribution affects the virtual shot records and coherent and incoherent noise, as well as the resulting Rayleigh-wave dispersion images. We demonstrate that coherent noise is present prior to the direct wave arrival, and therefore, this type of noise is often not take into account when the signal-to-noise ratio of correlations is computed using incoherent noise that arrives after the direct wave.

3.3 The Green's functions and multicomponent crosscorrelations

Under the far-field assumption, one can use crosscorrelations to approximate the elastic-wave Green's function as

$$G_{im}(r_A, r_B, \omega) - G^*_{im}(r_A, r_B, \omega) \approx -2j\omega \oint_S \frac{1}{\rho c} G^*_{ip}(r_A, r_S, \omega) G_{mp}(r_B, r_S, \omega) dS, \quad (3.1)$$

where $G_{im}(r_A, r_B, \omega)$ is the Green's function representing the ith component of particle displacement at location r_A due to a point force in the m direction at r_B, the asterisk denotes the complex conjugation, S represents the surface where sources are located, r_S represents the source location, ω is the angular frequency, j is the imaginary unit, ρ is the density and c is the phase velocity (Wapenaar & Fokkema, 2006). Here sources are uncorrelated (e.g. Lobkis & Weaver, 2001). In a homogeneous medium, and again under the far-field assumption, the vertical component fundamental-mode Rayleigh-wave Green's function can be written as (e.g. Fan & Snieder, 2009; Haney *et al.*, 2012)

$$G_{ZZ}(r) = \sqrt{\frac{1}{8\pi\omega r/c}} e^{j(\omega r/c + \pi/4)}, \quad (3.2)$$

where r is the distance between the source and receiver. Regardless of the source direction (i.e. subscript p in Equation 3.1), if two sensors record in the Z direction,

Equation 3.1 becomes

$$G_{ZZ}(r_A, r_B, \omega) - G^*_{ZZ}(r_A, r_B, \omega) \approx \frac{-j}{4\pi\rho} \oint_S \sqrt{\frac{1}{r_{SA} r_{SB}}} e^{j\omega(r_{SB} - r_{SA})/c} \delta(z) dS, \qquad (3.3)$$

where r_{SA} is the distance between the source r_S and the receiver r_A (Figure 3.1), and $\delta(z)$ indicates that all sources are distributed on the $z = 0$ plane, which is the ground surface.

The integrand in Equation 3.3 is the C_{ZZ} crosscorrelation for the source at r_S. When the source is far from the two sensors, $r_{SB} - r_{SA} \approx r\cos(\theta)$ and $r_{SA} \approx r_{SB} \approx r_S$. Because $dS = r_S dz d\theta$, Equation 3.3 can be written as

$$G_{ZZ}(r_A, r_B, \omega) - G^*_{ZZ}(r_A, r_B, \omega) \approx \frac{-j}{4\pi\rho} \int_0^{2\pi} e^{j\omega r\cos(\theta)/c} d\theta, \qquad (3.4)$$

where the integrand now is the phase of C_{ZZ} for a point source in the θ-direction. Following the same logic, and using

$$G_{RZ}(r) = \frac{H}{V} \sqrt{\frac{1}{8\pi\omega r/c}} e^{j(\omega r/c - \pi/4)}, \qquad (3.5)$$

where H/V is the ratio of the horizontal-to-vertical motion (e.g. Haney *et al.*, 2012), we can write

$$G_{ZR}(r_A, r_B, \omega) - G^*_{ZR}(r_A, r_B, \omega) \approx \frac{-j}{4\pi\rho} \frac{H}{V} \int_0^{2\pi} \cos(\theta) e^{j[\omega r\cos(\theta)/c - \pi/2]} d\theta, \qquad (3.6)$$

$$G_{RZ}(r_A, r_B, \omega) - G^*_{RZ}(r_A, r_B, \omega) \approx \frac{-j}{4\pi\rho} \frac{H}{V} \int_0^{2\pi} \cos(\theta) e^{j[\omega r\cos(\theta)/c + \pi/2]} d\theta, \qquad (3.7)$$

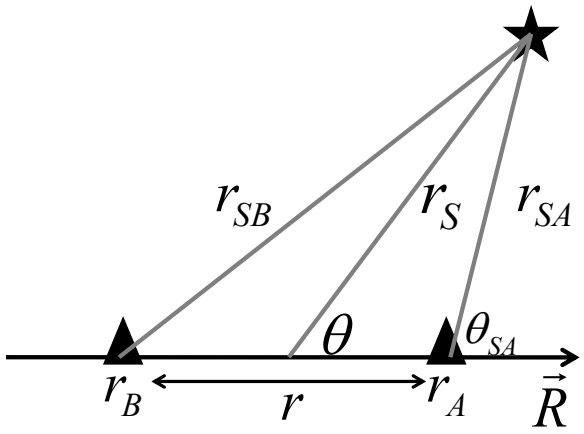

Figure 3.1: Diagram of the location of a point source and the receivers. The black star represents a point source; the black triangles represent the receivers. The R direction is parallel to the line linking the two sensors, r_A and r_B.

$$G_{RR}(r_A, r_B, \omega) - G^*_{RR}(r_A, r_B, \omega) \approx \frac{-j}{4\pi\rho}\left(\frac{H}{V}\right)^2 \int_0^{2\pi} \cos^2(\theta) e^{j\omega r\cos(\theta)/c} d\theta. \qquad (3.8)$$

The integrands in Equations 3.6, 3.7 and 3.8 are C_{ZR}, C_{RZ} and C_{RR} for a point source along the θ azimuth, respectively. Because $G_{RZ}(r_A, r_B, \omega) - G^*_{RZ}(r_A, r_B, \omega) = e^{j\pi}[G_{ZR}(r_A, r_B, \omega) - G^*_{ZR}(r_A, r_B, \omega)] = -[G_{ZR}(r_A, r_B, \omega) - G^*_{ZR}(r_A, r_B, \omega)]$, G_{ZR} possesses the same information as G_{RZ}. The actual source direction (subscript p in Equation 3.1) is not important; rather the recording direction (subscript m) plays the role of the source during correlation. Thus the Rayleigh waves can be generated by either vertical or horizontal sources (e.g. Nishida *et al.*, 2008).

3.4 The significance of the source angle

The source angle contributes to the three different kinds of crosscorrelations, C_{ZZ}, C_{ZR} and C_{RR}, in different ways. One can assess the role of the source angle by considering the integrands of the crosscorrelations (e.g. Fan & Snieder, 2009). The

source distribution area can be divided into two parts: a stationary-phase area (near $\theta = 0, \pi, 2\pi$ in Figure 3.2a) and a non-stationary phase area (the rapid oscillation area in Figure 3.2a). The sources in the stationary-phase area are important for retrieving the Green's functions; they contribute significantly to the integral in Equation 3.1 (Snieder, 2004; Snieder *et al.*, 2008; Mikesell *et al.*, 2012). If the sources are evenly distributed, the integrands of the C_{ZZ}, C_{ZR} and C_{RR} oscillate evenly in the non-stationary phase area and completely cancel the non-stationary phase energy in the integral from 0 to 2π. However, we are interested in the sources in the non-stationary phase area; thus we consider an isolated number of sources in small angular range.

At a constant receiver separation the stationary-phase area increases as frequency decreases; therefore, more sources can contribute to retrieval of the low frequency Green's function. However, the integrand of crosscorrelations (Equation 3.4, 3.6 and 3.8) oscillates slower as frequency decreases (Figure 3.3). Therefore, if the sources only exist in some small part of the non-stationary phase area, frequency-dependent energy will remain after the integration and lead to spurious waves (i.e. artifacts) in the retrieved G_{ZZ} (e.g. Yang & Ritzwoller, 2008). In contrast, at high frequencies the integrand oscillates rapidly (Figure 3.3), and the non-stationary phase source energy cancels over small angular ranges (Xu *et al.*, 2017). If we consider the integrands of C_{ZR} and C_{RR} (Figure 3.2b and c, respectively), we observe an interesting relationship between source angle and the amplitude of the integrand.

The non-stationary phase sources are spatially down weighted in the C_{ZR} and C_{RR} crosscorrelations due to the occurrence of the $\cos\theta$ in Equations 3.6 and 3.8. For each source, the Rayleigh-wave energy is projected to the R direction and decreases from the maximum to 0 as the source angle increases from $\theta = 0$ to $\pi/2$. Therefore

the integrand amplitude of C_{ZR} and C_{RR} is reduced in the non-stationary phase area compared to the amplitude of C_{ZZ} (Figure 3.2). Furthermore, the C_{RR} amplitudes are down weighted more than C_{ZR} outside the stationary-phase area due to the $\cos^2\theta$ term. Because of the projection in the R direction, C_{RR} is theoretically the most robust Rayleigh-wave estimation for uneven source distributions. Haney *et al.* (2012) pointed out that the $\cos\theta$ term acts as a spatial filter for the C_{ZR} and C_{RZ} components in the spatial autocorrelation (SPAC) method. The idea of the spatial filter does not only apply to C_{ZR}, but also to C_{RR} (Figure 3.2).

The envelopes of the integrands also demonstrate that C_{ZR} and C_{RR} attenuate the non-stationary phase energy equally for all frequencies (Figure 3.3). The stationary-phase energy in C_{RR} and C_{ZR} is preferentially weighted more than the non-stationary phase energy, and thus act as a spatial filter on the source distribution. This spatial filter is identical for different frequencies (Figure 3.3), different inter-station distances and different phase velocities because $\cos\theta$ is independent of these parameters. Furthermore, the filter does not affect the stationary-phase sources because $\cos\theta$ and $\cos^2\theta$ vary slower than the integrand (Figure 3.3). Finally, in the limit that the frequency goes to zero, or the inter-sensor distance goes to zero, the correlation function becomes an autocorrelation, and all space becomes the stationary-phase area. In that case, the spatial filter no longer plays a significant role in the accuracy of the retrieved Green's function.

3.5 A synthetic-noise source example

The integral on the right hand side of Equation 3.1 also represents the crosscorrelation between noise records of two receivers, r_A and r_B, if the noise sources are independent of each other (i.e. mutually uncorrelated) (Wapenaar & Fokkema, 2006). One can

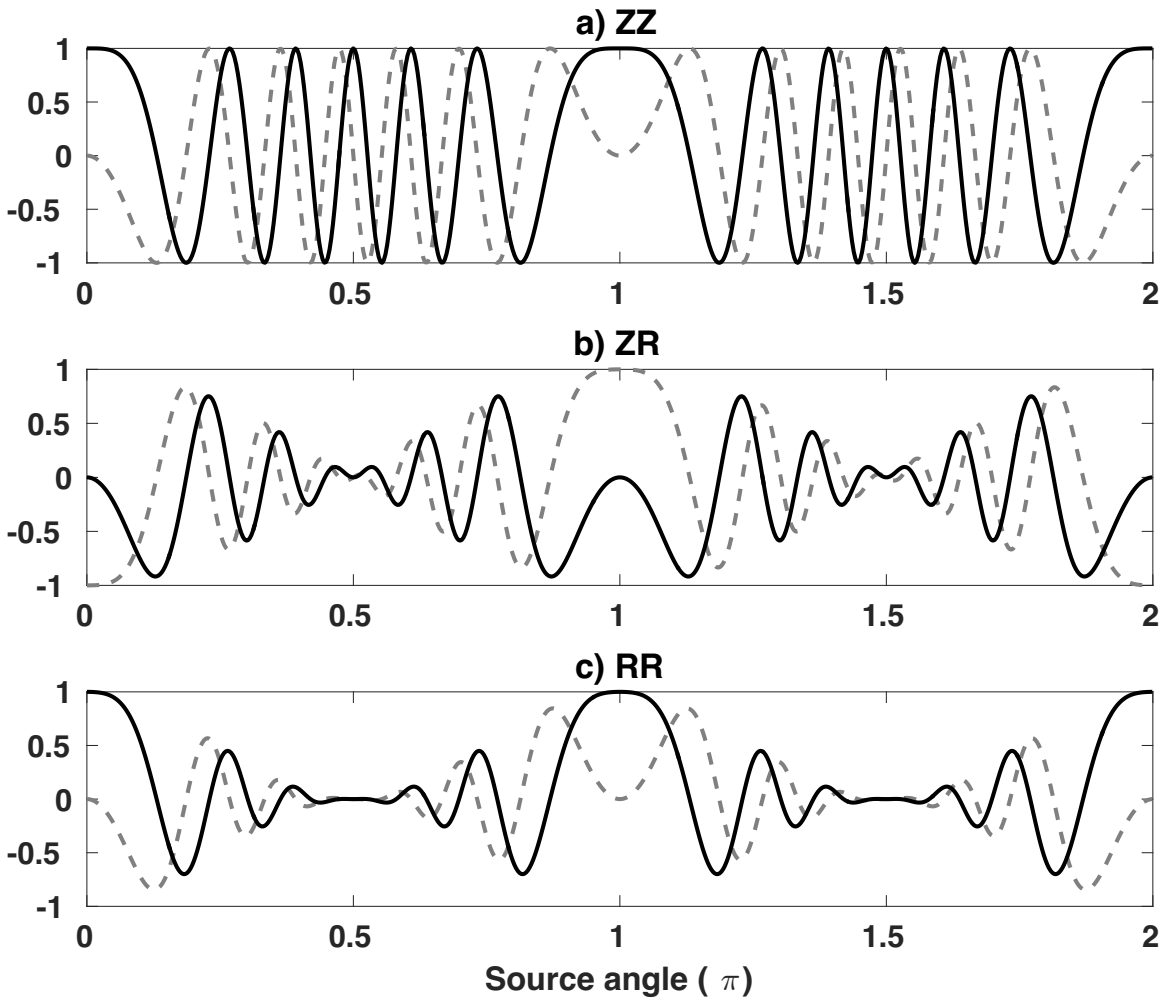

Figure 3.2: The amplitudes of the integrands of C_{ZZ}, C_{ZR} and C_{RR} (Equations 3.4, 3.6 and 3.8) change with the source angle (θ). The black solid line represents the real part of the integrand, and the gray dashed line represents the imaginary part. These examples are computed with a frequency (ω) of 5Hz, a phase velocity (c) of 200m/s, and an inter-station distance (r) of 120m.

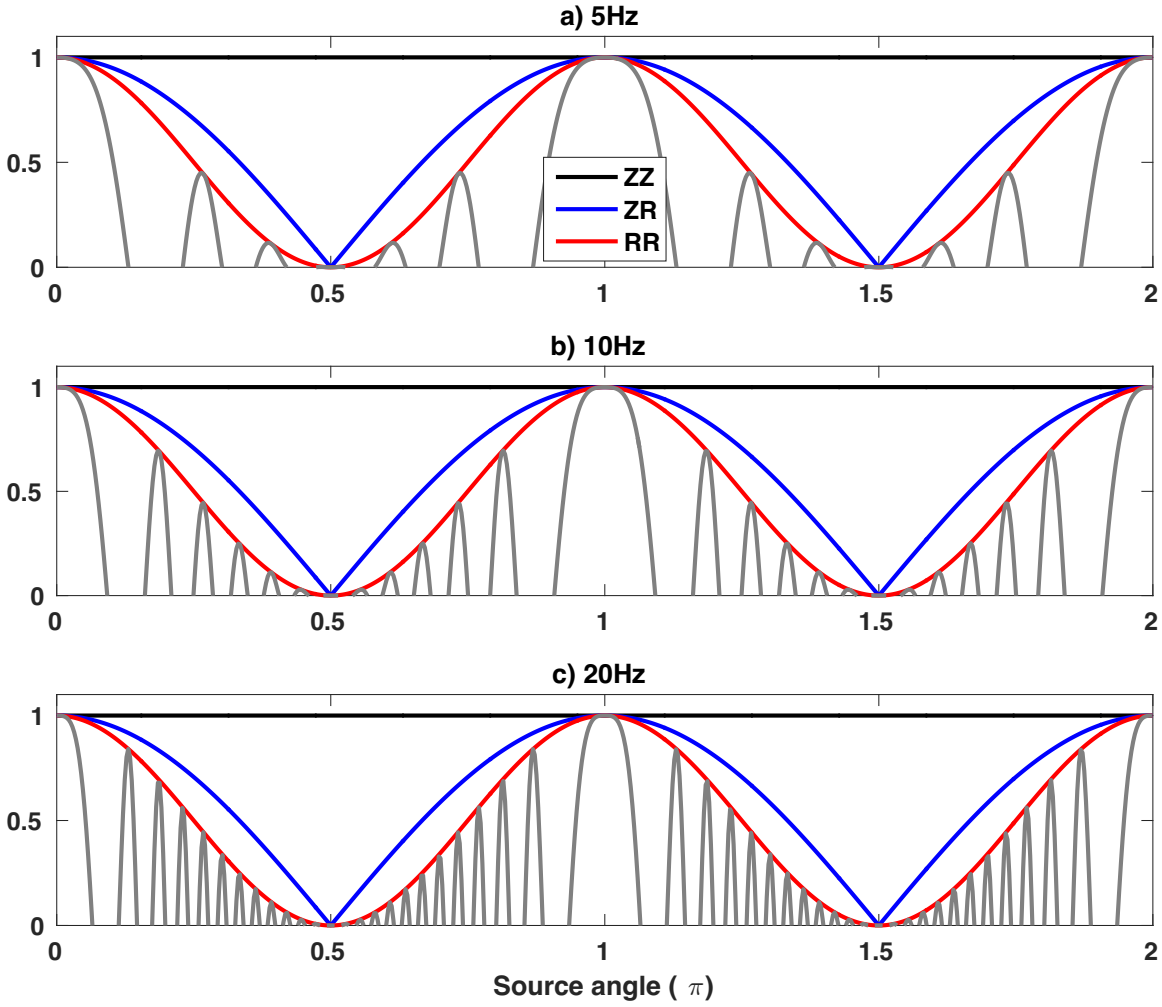

Figure 3.3: The envelope of the integrand of C_{ZZ} (black line), C_{ZR} (blue line) and C_{RR} (red line) at 5Hz (a), 10Hz (b) and 20Hz (c). The envelope is the L_2 norm of the real and imaginary part of the integrands in Equation 3.4, 3.6 and 3.8. The gray line is the real part of the integrand of C_{RR} weighted by $\cos^2\theta$. The oscillation rate of the phase of C_{ZZ} and C_{ZR} is identical to C_{RR}, and the phase varies much faster than the weighting term. Here we assume the phase velocity is 200m/s and the inter-sensor distance is 120m.

Table 3.1: The two-layer Earth model parameters used in the simulation.

Layer number	Vp (m/s)	Vs (m/s)	Density (kg/m^3)	Thickness (m)
1	1350	200	1900	25
2	2000	1000	2500	∞

then use Equation 3.1 to estimate the Rayleigh-wave Green's functions G_{ZZ}, G_{ZR} and G_{RR} from seismic noise (e.g. Halliday & Curtis, 2008). We demonstrate the reliability of C_{ZZ}, C_{ZR} and C_{RR} with a synthetic example, where noise sources are unevenly distributed. We compute virtual shot records along a linear array from correlations of the noise. The noise sources are randomly distributed within two angle ranges (Figure 3.4): from $-\pi/12$ to $\pi/12$ (the stationary-phase area) and from $\pi/4$ to $5\pi/12$ (the non-stationary phase area). The number of noise sources is used as a proxy for the noise energy strength, and the non-stationary phase noise energy is twice as strong as the stationary-phase noise energy in this example.

The Earth model we use has two layers (Table 3.1) and is from Bonnefoy-Claudet *et al.* (2006). All noise sources emit the same wavelet, and we model only the fundamental-mode Rayleigh wave. Each noise source is randomly activated during a 1-hour recording time. We simulate the response for every source using the algorithm proposed by Michaels & Smith (1997) and project the response to the Z and R components of the sensors. Then we stack all of these source projections to create a 1-hour long synthetic noise recording at each of the 24 geophones, which are 5 m apart from each other (Figure 3.4).

We assess the accuracy of the three crosscorrelations by comparing virtual shot records and comparing the Rayleigh-wave phase-velocity dispersion images to the true dispersion. We build virtual shot records (Figure 3.5a, b and c) from indi-

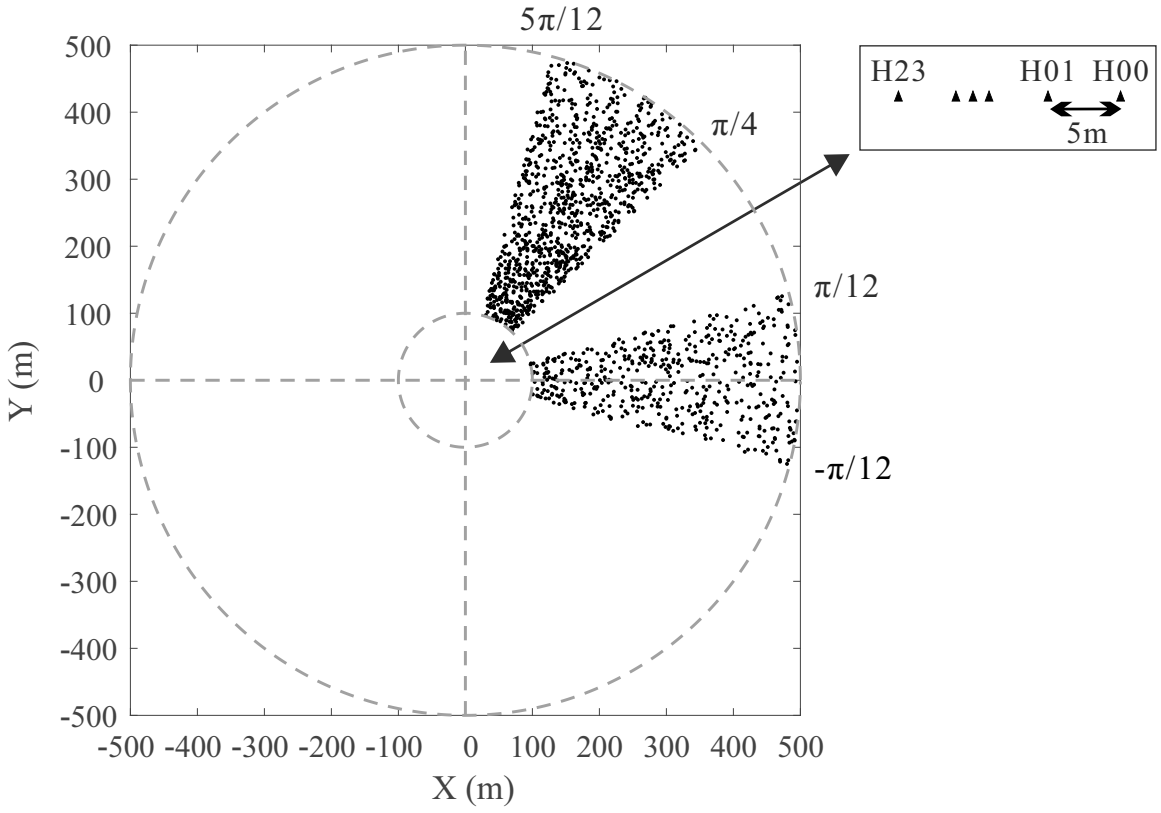

Figure 3.4: The experiment geometry indicates the location of noise sources (dots) and geophones (triangles). The noise sources are located away from the origin between 100m and 500m. See text for more details.

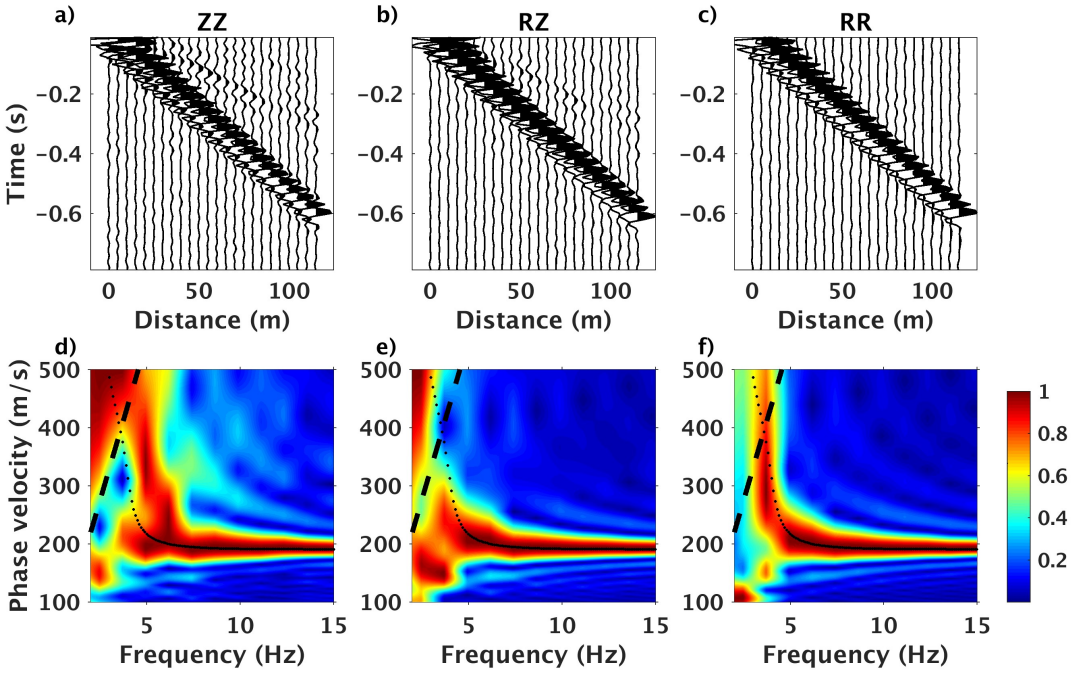

Figure 3.5: C_{ZZ}, C_{RZ} and C_{RR} virtual shot records (a,b,c) and the corresponding phase-velocity dispersion images (d,e,f). The dominant energy trends in a,b,c represent the Rayleigh wave. Black dots represent theoretical Rayleigh-wave phase velocities (Haskell, 1953) in d,e,f. The black dash lines in d,e,f, indicate the resolvable image area, where the wavelength is less than the array length. All dispersion images are normalized per frequency.

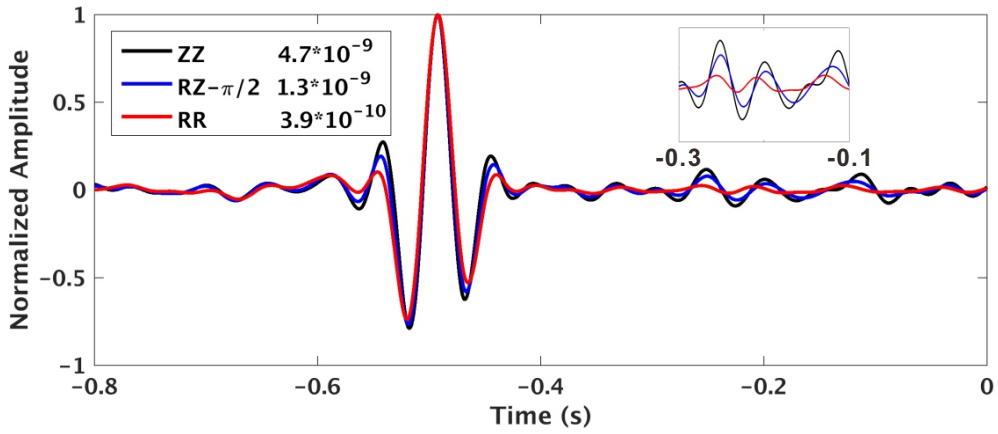

Figure 3.6: The amplitude normalized C_{ZZ}, C_{RZ} and C_{RR} functions between receivers H00 and H020. The inset shows a zoom of the spurious energy time window from $-0.1s$ to $-0.3s$. A $\pi/2$ phase shift has been applied to C_{RZ} to facilitate the comparison with C_{ZZ} and C_{RR}. The values in the legend indicate the maximum amplitude of each crosscorrelation function.

vidual crosscorrelations (e.g. Halliday *et al.*, 2008) and then map the data to the frequency-velocity domain using the phase-shift method (Song *et al.*, 1989) to generate phase-velocity dispersion images (Figure 3.5d, e and f). The virtual shot records and the dispersion images indicate that C_{RR} is the most robust among the three crosscorrelations. The dominate waveforms in the three crosscorrelations are from the stationary-phase area noise sources, and the high-velocity spurious wave before the main waveform is due to the non-stationary phase area noise energy. We find that C_{RR} contains lower-amplitude spurious waves than C_{ZR} and C_{ZZ} (Figure 3.6). The spurious waves in C_{ZZ} lead to the spurious energy trends at frequencies less than 7 Hz (Figure 3.5d), which is fully discussed in Xu *et al.* (2017). We also find that C_{ZR} does not provide accurate information below 5 Hz (Figure 3.5e). However, we observe accurate Rayleigh-wave phase velocities in the frequency-velocity domain of the C_{RR} below 5 Hz (Figure 3.5f), which matches the theoretical prediction in Section 3.4.

3.6 Discussion

Although C_{ZR} and C_{RR} attenuate non-stationary sources, the amplitudes of these two crosscorrelations are determined by the H/V ratio (Equation 3.6 and 3.8). The H/V ratio is normally less than 1; therefore, the C_{ZZ} amplitude is normally larger than C_{ZR} and C_{RR}. In our synthetic data example, the 3-15 Hz frequency-averaged H/V ratio is 0.41, the standard deviation is 0.21, and the C_{RR} peak amplitude is an order of magnitude smaller than the C_{ZZ} peak amplitude (Figure 3.6). Relative to the maximum amplitude of each correlation, the coherent noise (Figure 3.6, t >-0.4 s and inset) is much larger in C_{ZZ} than C_{RR}, while the incoherent noise (Figure 3.6, t <-0.6 s) is approximately the same. Therefore, when discussing notions of signal-to-noise ratio (SNR), one needs to consider both coherent and incoherent noise. Artifacts due to an uneven source distribution should be considered coherent noise, while random fluctuations should be considered incoherent noise.

In most studies, authors compute SNR as the ratio between the maximum Rayleigh wave amplitude and the incoherent noise (e.g. Bensen *et al.*, 2007; Lin *et al.*, 2008). The incoherent noise is measured based on a window of data after the direct arrival (e.g. Bensen *et al.*, 2007; Lin *et al.*, 2008). If we assume that the random fluctuation (i.e. incoherent noise) amplitude is the same on the Z component and the R component, then the SNR of C_{ZR} and C_{RR} will be less than that of C_{ZZ} any time the Rayleigh wave H/V ratio is less than 1. Thus in practice, people observe (compute) that C_{ZZ} has a higher SNR than C_{ZR} and C_{RR} (e.g. Lin *et al.*, 2008). However, this SNR metric does not take into account the coherent noise that precedes the direct Rayleigh wave. One approach to monitor the coherent noise is to use a continuous SNR computation method (e.g. Larose *et al.*, 2007; Clarke *et al.*, 2011).

Finally, C_{ZR} and C_{RR} can also aid the identification of fundamental and higher-model surface waves when the two surface-wave dispersion curves are very close in the frequency-velocity domain (Boué *et al.*, 2016; Ma *et al.*, 2016). The fact that Rayleigh wave modes have different H/V ratios and particle motions enables one to identify (e.g. Boaga *et al.*, 2013) and separate these modes (e.g. Gribler *et al.*, 2016) to improve the reliability of dispersion estimation.

3.7 Conclusion

We present the relationships between the fundamental-mode Green's functions (G_{ZZ}, G_{ZR} and G_{RR}) and crosscorrelation functions (C_{ZZ}, C_{ZR} and C_{RR}) within the far-filed approximation. When estimating the fundamental-mode Rayleigh-wave Green's functions, the C_{ZZ} crosscorrelation weights source energy equally from all directions. In contrast, the C_{ZR} and C_{RR} crosscorrelations attenuate source energy in the non-stationary phase area for all frequencies and thus act as spatial filters on the source distribution. Therefore, more accurate Green's functions (i.e. fewer spurious arrivals or reduced coherent noise) are retrieved from C_{ZR} and C_{RR} compared to C_{ZZ} when the source energy is unevenly distributed. We demonstrate the validity of this theoretical inference with a synthetic seismic noise example. Those interested in characterizing velocity structure from ambient noise Rayleigh waves should use C_{RR} whenever possible to limit the effect of non-homogeneous noise source distributions on the frequency-dependent direct-wave phase velocity. Finally, we note that the analysis presented here pertains to the direct-wave Rayleigh wave; we have neglected how the multicomponent crosscorrelations influence scattered waves.

CHAPTER 4:

RAYLEIGH-WAVE MULTICOMPONENT CROSSCORRELATION-BASED SOURCE STRENGTH DISTRIBUTION INVERSION. PART 1: THEORY AND NUMERICAL EXAMPLES

This chapter has been published as: Xu, Z., Mikesell, T. D., Gribler, G., & Mordret, A. (2019). Rayleigh-wave multicomponent cross-correlation-based source strength distribution inversion. Part 1: Theory and numerical examples. Geophysical Journal International, 218(3), 1761-1780.

4.1 Summary

Crosscorrelation-based seismic interferometry is commonly used to retrieve surface-wave Green's functions from ambient seismic noise recordings. This approach requires that seismic sources are isotropically distributed in all directions around two receivers. However, this assumption is rarely valid in practice. Thus full-waveform inversion theory has recently been applied to seismic noise crosscorrelation functions, functions that include both source and structure information. Source information (like locations

and strengths) are essential for accurate structure information estimation. In this paper, we explain physically two types of source sensitivity kernels: one derived from traveltime misfits and the other derived from waveform misfits. We use these kernels for source inversion, and demonstrate the benefits of using multicomponent crosscorrelations in this source estimation process.

4.2 Introduction

One nowadays commonly crosscorrelates ambient seismic recordings of two sensors to retrieve the surface-wave Green's functions between the two sensors (e.g. Snieder, 2004). Assuming the crosscorrelation function is the band-limited Green's functions, one can estimate subsurface geologic structures (e.g. Shapiro *et al.*, 2005). The crosscorrelation method, or seismic interferometry, requires that seismic sources are isotropically distributed in all directions around two receivers (e.g. Wapenaar & Fokkema, 2006). However, this assumption is rarely valid in practice. An anisotropic source distribution will bias the retrieved Green's functions and the resulting subsurface geologic inferences (e.g. Yang & Ritzwoller, 2008; Yao & Van Der Hilst, 2009). To reduce this bias, approaches have been developed to compensate for the anisotropic source distribution. For example, one approach uses beamforming (e.g. Rost & Thomas, 2002) to estimate the seismic source direction and then uses this direction to correct the retrieved Green's function or surface-wave dispersion estimates (e.g. Nakata *et al.*, 2015; Cheng *et al.*, 2016). When using beamforming, one assumes that the underground is isotropic and laterally homogeneous. This assumption for the subsurface structures is also not always valid. For anisotropic seismic source distributions and laterally heterogeneous subsurface structures, it has been proposed not to use the seismic crosscorrelations to approximate Green's functions, but instead to

apply full-waveform inversion theory to the seismic crosscorrelations (Tromp *et al.*, 2010; Fichtner, 2015). The seismic crosscorrelations include both source distribution and subsurface structure information. If one wants to estimate the subsurface structure, one has to first (e.g. Nakata *et al.*, 2015; Cheng *et al.*, 2016), or simultaneously (e.g. Yao & Van Der Hilst, 2009; Harmon *et al.*, 2010), unravel the anisotropic source information.

Source distribution estimation can aid studies of the dynamic processes that generate ambient seismic noise. For example, high-frequency (>1 Hz) ambient seismic noise can be used to monitor underground hydrothermal acoustic sources (e.g. Cros *et al.*, 2011) and microseismic sources at the exploration scale (e.g. Corciulo *et al.*, 2012); 5-20 s period ambient seismic noise can be used to study the primary and secondary microseisms (e.g. Tian & Ritzwoller, 2015; Juretzek & Hadziioannou, 2016); 100 s period can be used to study the Earth hum (e.g. Rhie & Romanowicz, 2006; Nishida & Fukao, 2007; Traer & Gerstoft, 2014; Ardhuin *et al.*, 2015).

Rayleigh waves dominate ambient seismic noise. Multicomponent Rayleigh-wave data can bring benefits for estimating both source distributions and subsurface structure. The important multicomponent data for Rayleigh waves are the vertical (Z) and radial (R) components, where the R direction is parallel to a line or great-circle path between two sensors. If we assume vertical-force seismic sources, the $Z-Z$ component crosscorrelation (C_{ZZ}) is sensitive to the seismic sources in all directions, while the $R-R$ component crosscorrelation (C_{RR}) is more sensitive to in-line seismic sources than out-of-line sources (e.g. Haney *et al.*, 2012; Xu & Mikesell, 2017). Multicomponent data can also help to characterize Rayleigh waves more accurately than only the Z component data (e.g. Boaga *et al.*, 2013; Gribler *et al.*, 2016) and

constrain the shear-wave velocity inversions (e.g. Arai & Tokimatsu, 2004). In this paper, we focus on source estimation rather than structure estimation.

There are mainly two methods for locating seismic sources, an imaging method and an adjoint-based inversion method. When using the imaging method, one applies time reversal to recorded seismic waveforms and then finds the location where the reversed waveforms are most similar to each other. This method includes backprojection (e.g. Ishii *et al.*, 2005), reverse-time migration (e.g. Artman *et al.*, 2010) and matched-field processing (e.g. Cros *et al.*, 2011). These approaches do not involve so-called inversion, as compared to the adjoint-based inversion method. The adjoint-based inversion method combines time reversal and iterative optimization (e.g. Liu *et al.*, 2004). When using either of these two methods, one assumes that the subsurface structure is known and then solves for the source parameters (e.g. location or moment tensors). Thus we study multicomponent crosscorrelations in the context of ambient noise full-waveform inversion in this paper.

We adopt full-waveform inversion theory to estimate seismic source distributions. We compare the use of traveltime and waveform information in inversion, and we discuss the source sensitivity kernels for C_{ZZ} and C_{RR}. We present the complete inversion scheme in Section 4.3. In Section 4.4, we present the kernels for a single frequency and a frequency band, and we explain the physics behind these kernels. We then apply the multicomponent source kernels in three synthetic data examples and estimate the source distributions (Section 4.5). Finally, we discuss factors that affect the accuracy of the inversions in Section 4.6.

4.3 Crosscorrelation inversion scheme

We use full-waveform inversion theory to estimate seismic source distributions. In an inversion process, we define a misfit function to measure the difference between the synthetic and observed data (Section 4.3.1). The observed data in this paper are observed Rayleigh-wave crosscorrelations. We compute synthetic crosscorrelations using a forward modelling process based on the source model parameters, i.e. the source strength distribution (Section 4.3.2). We then update the source model parameters with an inversion method that minimizes the misfit function (Section 4.3.4). This is a common strategy in non-linear inverse problems (e.g. Aster *et al.*, 2011)

4.3.1 Misfit functions

One can define the misfit function (χ) based on physical properties of waveforms, for example traveltimes (e.g. Luo & Schuster, 1991; Dahlen *et al.*, 2000), envelopes (e.g. Fichtner *et al.*, 2008; Bozdağ *et al.*, 2011) or raw waveforms (e.g. Tromp *et al.*, 2005). Here we use two L_2–norm misfit functions: Rayleigh-wave waveform crosscorrelation difference (Equation 4.1) and Rayleigh-wave traveltime difference (Equation 4.2). We define the waveform misfit function as

$$\chi = \frac{1}{2} \sum_{mn} \sum_{r_A r_B} \int [w(t)(C_{mn}(r_A, r_B, t) - C^o_{mn}(r_A, r_B, t))]^2 dt \tag{4.1}$$

where $w(t)$ is a time window, and $C_{mn}(r_A, r_B, t)$ and C^o_{mn} are the synthetic and observed crosscorrelations, respectively. The crosscorrelations are between sensor r_A and r_B; m, n represent the components, vertical (Z) or radial (R), from each of the two sensors, respectively. We use the time window to focus on certain parts of the observed crosscorrelations (e.g. Maggi *et al.*, 2009; Fichtner *et al.*, 2017). We define

the traveltime misfit function following Luo & Schuster (1991) as

$$\chi = \frac{1}{2} \sum_{mn} \sum_{r_A r_B} (T_{syn}(r_A, r_B) - T_{obs}(r_A, r_B))^2, \tag{4.2}$$

where T_{syn} and T_{obs} represents the traveltime of the main Rayleigh-wave waveform in the synthetic and observed crosscorrelations, respectively. Luo & Schuster (1991) and Dahlen *et al.* (2000) describe how to measure the traveltime difference, $T_{syn} - T_{obs}$. We restate this measurement procedure in Appendix B.1. In this paper, we call the source inversions using the waveform and the traveltime misfit functions as the waveform inversion and the traveltime inversion, respectively.

4.3.2 Forward modelling process

We need synthetic data to calculate the misfit function. We compute synthetic crosscorrelations from a source distribution with the forward modelling process. People have discussed the whole forward modelling process explicitly (e.g. Wapenaar & Fokkema, 2006; Tromp *et al.*, 2010; Fichtner *et al.*, 2017). We here review the main steps in the forward modelling process implemented in the frequency domain. We first write the seismic record at one sensor (r_A) due to many sources as

$$U_{mp}(r_A, \omega) = \int_V G_{mp}(r_A, r_s, \omega) F_p(r_s, \omega) dr_s, \tag{4.3}$$

where $G_{mp}(r_A, r_s, \omega)$ is the Green's function representing the mth component displacement response at location r_A due to a point force in the p direction at the source position r_s, ω is the angular frequency, and $F_p(r_s, \omega)$ is the the source wavelet

spectrum. We then crosscorrelate two sensor (r_A and r_B) records as

$$\begin{aligned} C_{mn}(r_A, r_B, \omega) &= U_{mp}(r_A, \omega) U^*_{np}(r_B, \omega) \\ &= \int_V G_{mp}(r_A, r_s, \omega) G^*_{np}(r_B, r_s, \omega) S_p(r_s, \omega) dr_s, \end{aligned} \tag{4.4}$$

where the asterisk represents complex conjugation. Here we assume that all seismic sources are independent, thus

$$S_p(r_s, \omega) = F_p(r_s, \omega) F^*_p(r_s, \omega). \tag{4.5}$$

We note that the source strength, S_p, should be nonnegative for all frequencies.

The forward modelling process is computationally expensive. Equation 4.4 requires one simulation for one point force source at r_s in the p direction. If we have many seismic sources like traffic, we have to conduct many simulations. Therefore people have proposed to decrease the computation by using wavefield reciprocity (e.g. Tromp *et al.*, 2010; Ermert *et al.*, 2017). With the reciprocity (e.g. Aki & Richards, 2002),

$$G_{mp}(r_A, r_s) = G_{pm}(r_s, r_A), \tag{4.6}$$

and we can modify the forward simulations by activating seismic sources at sensors (r_A), instead of at real seismic sources (r_s). The number of sensors is normally less than the number of potential seismic sources in the source grid. This decreases the forward computation dramatically.

4.3.3 Fréchet derivative with respect to source strength

Source inversion requires the Fréchet derivative of the misfit function due to perturbations in the source distribution (e.g. Fichtner, 2015; Sager *et al.*, 2018). Here we review the steps to derive the Fréchet derivative. First, we write the perturbation of the misfit function due to a perturbation in the synthetic crosscorrelation as (e.g. Fichtner, 2015)

$$\delta\chi(r_A, r_B) = \int_\omega \delta C_{mn}(r_A, r_B, \omega) f d\omega, \tag{4.7}$$

where f is the adjoint source. The adjoint source is derived from the misfit function, and we show how we derive the traveltime and waveform adjoint sources in Appendices B.1 and B.2.

We then write the perturbation of the synthetic crosscorrelation (Equation 4.4) with a first-order term as

$$\begin{aligned}\delta C_{mn}(r_A, r_B, \omega) = &\int_V G_{mp}(r_A, r_s, \omega) G^*_{np}(r_B, r_s, \omega) \delta S_p(r_s, \omega) dr_s \\ &+ \int_V \delta[G_{mp}(r_A, r_s, \omega) G^*_{np}(r_B, r_s, \omega)] S_p(r_s, \omega) dr_s,\end{aligned} \tag{4.8}$$

where the first part in the right hand side is for perturbations in the source, and the second part is for perturbations in the Green's functions. These two parts provide Fréchet source and structure derivatives (Fichtner, 2015). We focus on the source derivative in this paper; thus we assume that the subsurface structure and the Green's functions are known, such that $\delta[G_{mp}(r_A, r_s, \omega) G^*_{np}(r_B, r_s, \omega)] = 0$. This assumption is common in source studies (e.g. Liu *et al.*, 2004; Ishii *et al.*, 2005; Artman *et al.*, 2010). We thus write the perturbation of the crosscorrelation with respect to source

strength perturbations as

$$\delta C_{mn}(r_A, r_B, \omega) = \int_V G_{mp}(r_A, r_s, \omega) G^*_{np}(r_B, r_s, \omega) \delta S_p(r_s, \omega) dr_s. \tag{4.9}$$

We then write the Fréchet derivative of the misfit function due to perturbations in the source strength by combining Equations 4.7 and 4.9 as

$$\delta\chi(r_A, r_B) = \int_\omega \int_V G_{mp}(r_A, r_s, \omega) G^*_{np}(r_B, r_s, \omega) \delta S_p(r_s, \omega) f dr_s d\omega, \tag{4.10}$$

$$= \int_\omega \int_V K_{mn}(r_A, r_B, \omega) \delta S_p(r_s, \omega) dr_s d\omega, \tag{4.11}$$

where

$$K_{mn}(r_A, r_B, \omega) = G_{mp}(r_A, r_s, \omega) G^*_{np}(r_B, r_s, \omega) f. \tag{4.12}$$

K_{mn} is called the source kernel (e.g. Fichtner *et al.*, 2017). The kernel indicates the sensitivity of the misfit function to the source strength at r_s, $S_p(r_s, \omega)$. In practice, it is often assumed that the spectral shapes for all sources (S_p) are similar (e.g. Ermert *et al.*, 2017). Thus we assume that $S_p^0 N = S_p$, where S_p^0 is the assumed source spectrum and N is a ratio. N is always positive due to Equation 4.5. Finally, we rewrite Equations 4.11 and 4.12 as

$$\delta\chi(r_A, r_B) = \int_\omega \int_V K_{mn}(r_A, r_B, \omega) \delta N(r_s) dr_s d\omega \tag{4.13}$$

with

$$K_{mn}(r_A, r_B, \omega) = G_{mp}(r_A, r_s, \omega) G^*_{np}(r_B, r_s, \omega) S^0_p f \tag{4.14}$$

$$= [G_{mp}(r_A, r_s, \omega) F^0_p][G_{np}(r_B, r_s, \omega) F^0_p]^* f, \tag{4.15}$$

where $S^0_p = F^0_p (F^0_p)^*$. Equation 4.15 is convenient to use because we can easily compute synthetic seismic recordings ($G_{mp} F^0_p$) with the same numerical simulations used to create synthetic crosscorrelation functions. Thus in the following context, we use $N(r_s)$ as the source strength distribution model and use Equation 4.15 to calculate source sensitivity kernels.

4.3.4 Inversion strategy

We use a gradient-descent strategy (e.g. Ermert *et al.*, 2017), which is an iterative method. The traveltime misfit function (Equation 4.2) is a non-linear problem and thus requires an iterative method. We can, however, minimize the waveform L2–norm misfit function (Equation 4.1) using direct methods because the source strengths are linearly related to the crosscorrelation waveforms in the frequency domain (Equation 4.4). While it is useful to recognize this last point, the waveform misfit function can be too large to solve with linear inversion methods directly due to the potential for a large number of waveforms and source locations. Thus iterative methods are a better option for the sake of memory in such large problems (e.g. Aster *et al.*, 2011), and we choose to solve the waveform misfit function with the same iterative method as the traveltime mistfit function. Another way to address this problem is using the adjoint operator (e.g. Thorson & Claerbout, 1985), for example, the matched-field processing method (e.g. Cros *et al.*, 2011; Corciulo *et al.*, 2012) and microseismic reverse-time

migration (e.g. Artman *et al.*, 2010). We discuss the link between the waveform inversion and the matched-field processing and reverse-time migration methods in Appendix B.3.

In the waveform inversion, we sum the kernels among all sensor pairs in a frequency band $[\omega_1, \omega_2]$ as

$$K = \sum_{mn} \sum_{r_A r_B} \int_{\omega_1}^{\omega_2} K_{mn}(r_A, r_B, \omega) d\omega. \tag{4.16}$$

If we only use vertical data, K is a summed K_{ZZ} among all sensor pairs; if we use both C_{ZZ} and C_{RR}, $K = K_{ZZ} + K_{RR}$ among all sensor pairs. We then multiply the summed kernel (K) with a step size (p) to update the source distribution in the ith iteration as

$$N_{i+1}(r_s) = N_i(r_s) - pK. \tag{4.17}$$

However, if we subtract the product (pK) directly, negative source strength values may appear. A negative source strength is not physical because of Equation 4.5. Thus we need to make sure that the updated source strengths are nonnegative. To achieve this, we apply a positivity constraint (Johansen, 1977) to the inversion, where $\delta ln[N(r_s)] = \delta N(r_s)/N(r_s)$. Rearranging this relationship and replacing $\delta N(r_s)$, Equation 4.13 becomes

$$\delta\chi(r_A, r_B) = \sum_{mn} \sum_{r_A r_B} \int_{\omega} \int_{V} K_{mn}(r_A, r_B, \omega) N(r_s) \delta ln[N(r_s)] dr_s d\omega, \tag{4.18}$$

where ln is the natural logarithm. We then update the source strength distribution as

$$ln[N_{i+1}(r_s)] = ln[N_i(r_s)] - pN_i(r_s)K, \tag{4.19}$$

which is equivalent to

$$N_{i+1}(r_s) = N_i(r_s)e^{-pN_i(r_s)K}, \tag{4.20}$$

and where the exponential term is always positive, thus ensuring the source model will always be positive as long as the starting model is positive.

We choose the step size (p) from many potential step size values. We update the source strength distribution (N_i) using Equation 4.20 and the potential step sizes (e.g. $p = 10^{-6}, 10^{-5}, ...10^{-1}$). For each step size, we have an updated source distribution model (N_{i+1}), and we compute synthetic crosscorrelations using Equation 4.4. We then calculate the corresponding misfit function. Among these misfit values, we choose the step size that gives the minimum misfit. If the minimum misfit is less than an update criteria (C_u), we adopt the step size and update the source model; if not, we do not update this iteration and instead expand the frequency band. Details about the inversion are presented in Section 4.5.

4.4 Rayleigh-wave source kernels

We present and describe the source kernels for Rayleigh waves of multicomponent crosscorrelations (C_{ZZ} and C_{RR}). In calculating the kernels, we require synthetic seismic recordings and adjoint sources (Equation 4.15). We use a homogeneous elastic halfspace model (Table 4.1 True model) and use SPECFEM3D (Komatitsch & Tromp, 2002) to simulate the synthetic seismic recordings. We set the model to be a 3km-length cube. We set the top surface of the cube to be a free surface and the other surfaces to be perfectly-matched layers. We discretize the whole cube into 30 m-length cubes. In one simulation, the time step is 0.0005 s and we propagate signals for 5000 time steps (i.e. 2.5 s). We simulate Z and R component data on the two receivers (r_A

Table 4.1: The homogeneous and isotropic elastic Earth model parameters used in the simulation.

Model	Vp (m/s)	Vs (m/s)	Density (kg/m^3)	Thickness (m)
True	2800	1500	2300	∞
Higher	3800	2000	2300	∞
Lower	1900	1000	2300	∞

and r_B) due to 6720 vertical-point-force sources on the free surface (Figure 4.1a). Each source emits a 10 Hz Ricker wavelet with an amplitude factor of 10^{15} in SPECFEM3D (F_z in Equation 4.5, also F_z^0 in Equation 4.15). Following Section 4.3.2, we do 4 simulations ($Z-$ and $R-$ direction point forces at each receiver), and record at the 6720 seismic source locations. We compute C_{ZZ} and C_{RR} (Equation 4.4). The phase of C_{ZZ} is identical to that of C_{RR} (Figure 4.1b).

We focus on the sensitivity kernels for synthetic data in this section to study the kernel structure. Therefore we use two modified misfit functions:

$$\chi(r_A, r_B) = T_{syn} \tag{4.21}$$

and

$$\chi(r_A, r_B) = \frac{1}{2}\int [w(t)C_{mn}(r_A, r_B, t)]^2 dt. \tag{4.22}$$

These two misfit functions indicate the traveltime and energy for main waveforms in the synthetic crosscorrelations, respectively (Fichtner *et al.*, 2017). The corresponding adjoint sources are presented in Appendix B.1 and B.2. The corresponding source kernels determine how source strength changes affect the traveltime or waveform energy.

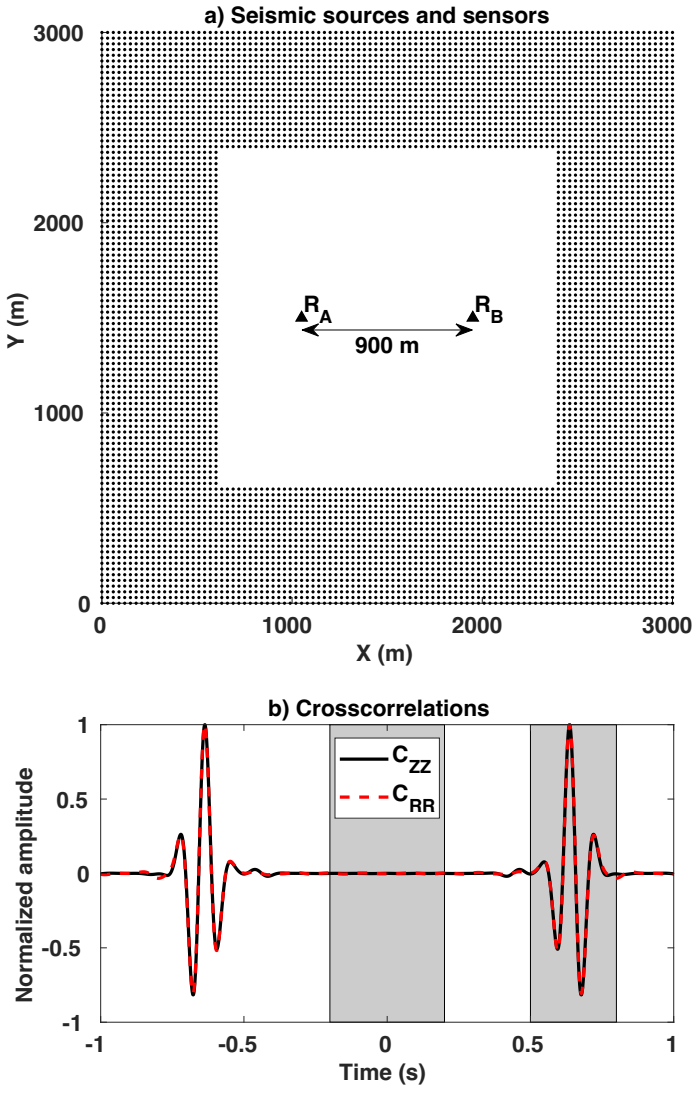

Figure 4.1: a) Diagram of locations of the 6720 point sources and two receivers on the free surface. The black points represent point sources; the two black triangles represent the two receivers, r_A and r_B. b) The vertical-vertical (C_{ZZ}) and radial-radial (C_{RR}) crosscorrelation between the two receivers due to all sources in a). The two crosscorrelations are normalized by each maximum amplitude. The two gray blocks indicate two time windows, $-0.2 \sim 0.2$ and $0.5 \sim 0.8$ s.

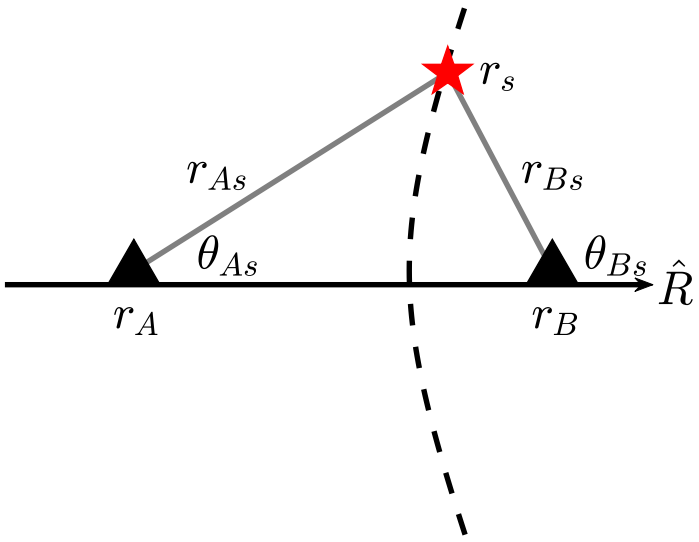

Figure 4.2: Diagram of the location of a point source (star) and two sensors (triangles). The dashed hyperbola indicates potential source locations, where $r_{As} - r_{Bs}$ is constant. The radial direction, $\hat{R}$, is parallel to the line linking the two sensors, r_A and r_B.

4.4.1 Monochromatic source kernels

We now describe the monochromatic crosscorrelation source kernels from a physical point of view. In a homogeneous and isotropic medium, under the far-field assumption, the vertical-component fundamental-mode Rayleigh-wave Green's function due to a vertical point force can be written as (e.g. Fan & Snieder, 2009):

$$G_{ZZ}(r,\omega) = \sqrt{\frac{1}{8\pi\omega r/c}} e^{-i(\omega r/c + \pi/4)}, \tag{4.23}$$

where ω is the angular frequency, i is the imaginary unit, c is the surface-wave phase velocity and r is the distance between source and receiver. The negative sign in the exponential part of Equation 4.23 is due to the Fourier transform convention we use (Appendix B.4). If we consider a vertical-point-force seismic source on the free

surface at r_s, the surface-wave crosscorrelation between two sensors (r_A and r_B) can be written as

$$C_{ZZ}(r_A, r_B, \omega, r_s) = \frac{1}{8\pi\omega/c}\sqrt{\frac{1}{r_{As}r_{Bs}}}e^{-i\omega(r_{As}-r_{Bs})/c}. \tag{4.24}$$

Following the same logic, and using

$$G_{RZ}(r, \omega) = \frac{H}{V}\sqrt{\frac{1}{8\pi\omega r/c}}e^{-i(\omega r/c-\pi/4)}, \tag{4.25}$$

where H/V is the ratio of the horizontal-to-vertical motion (e.g. Haney *et al.*, 2012), we can write

$$C_{RR}(r_A, r_B, \omega, r_s) = \left(\frac{H}{V}\right)^2 \frac{1}{8\pi\omega/c}\sqrt{\frac{1}{r_{As}r_{Bs}}}cos(\theta_{As})cos(\theta_{Bs})e^{-i\omega(r_{As}-r_{Bs})/c}, \tag{4.26}$$

where θ_{As} is the angle between the surface-wave propagation path and the radial direction (Figure 4.2). The phase of the Rayleigh wave is $-\omega(r_{As} - r_{Bs})/c$ in Equation 4.24 and 4.26. These phases remain constant if $r_{As} - r_{Bs}$ remains constant; $r_{As} - r_{Bs}$ will be constant if r_s is on a hyperbola with foci at r_A and r_B (Figure 4.2). Thus a certain phase corresponds to a hyperbola, comprised of r_s locations. For C_{ZZ} and C_{RR}, we focus on two specific phases:

$$-\frac{\omega(r_{As} - r_{Bs})}{c} = \phi_{obs} + 2N\pi, \tag{4.27}$$

and

$$-\frac{\omega(r_{As} - r_{Bs})}{c} = \phi_{obs} + (2N - 1)\pi, \tag{4.28}$$

where ϕ_{obs} is the phase of the observed waveform at $N = 0, \pm1, \pm2, \pm3...$ and frequency ω. The two phases lead to two kinds of hyperbolas (Figure 4.3): $\phi_{obs} + 2N\pi$ phase leads to the same phase (ϕ_{obs}); the $\phi_{obs} + (2N-1)\pi$ leads to the opposite phase ($\phi_{obs} \pm \pi$). These hyperbolas are determined by the value of ϕ_{obs}, which also change with frequency (e.g. Xu *et al.*, 2017).

These two kinds of crosscorrelations contribute ±1 to the amplitude spectrum, but 0 to the phase spectrum of the Rayleigh wave in C_{ZZ} over the time window $w(t)$. If we increase or decrease the source strength along one of these hyperbolas, the arrival time of the Rayleigh waveform will not change because the corresponding phase spectrum does not change; however, the waveform energy will increase or decrease, respectively. This is because the sources along the hyperbola generate waveforms with exactly the same phase and arrival time. Therefore the hyperbola is located along the zero value in the traveltime kernels, and along the maxima and minima of the waveform-energy kernels (Figure 4.3). Chmiel *et al.* (2018) observed similar source kernels with dense active-source seismic recordings and calculated the surface-wave phase velocities by fitting hyperbolas to the kernels using Equations 4.27 and 4.28.

We point out that the traveltime and waveform kernels for RR are stronger in the in-line areas than out-of-line areas (Figures 4.3b and 4.3d). This azimuthal effect is due to the $cos(\theta_{As})cos(\theta_{Bs})$ term in Equation 4.26. Xu & Mikesell (2017) observed this effect and noted that this effect is frequency independent. The *cos* term can change sign with the receivers. Therefore the RR kernels can also change the sign of the kernel values, even if r_s moves along the same hyperbola as seen in Figure 4.3b and 4.3d. The absolute amplitude difference in the sensitivities between ZZ and RR kernels is due to the H/V ratio (Equation 4.26). Depending on the subsurface model,

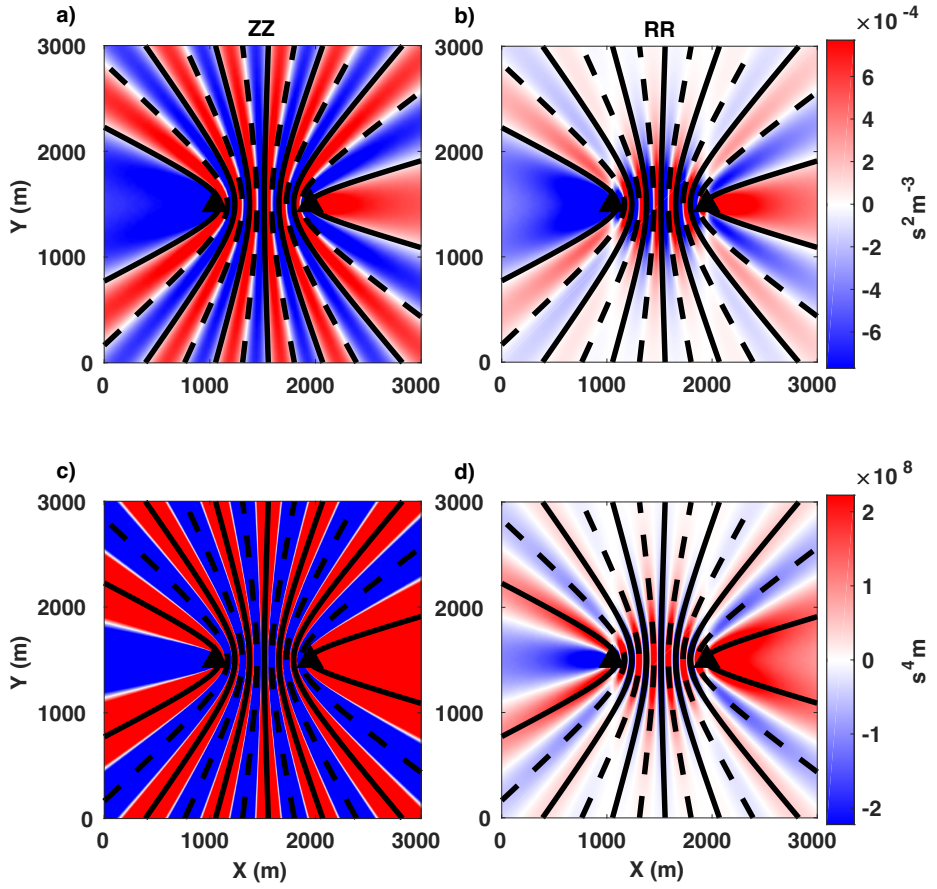

Figure 4.3: Traveltime (top row) and waveform-energy (bottom row) source kernels computed at each grid node for 5 Hz direct Rayleigh waves in the causal parts of C_{ZZ} (left column) and C_{RR} (right column). The solid hyperbolas represent $2N\pi$ phase and the dashed represent $(2N-1)\pi$. The direct Rayleigh-wave time window is from 0.5 s to 0.8 s in Figure 4.1. These hyperbolas are asymmetric due to the value of ϕ_{obs} in Equations 4.27 and 4.28.

this indicates that either the ZZ or RR kernel could dominate the stacked kernel (Equation 4.16) at a particular frequency depending on the H/V ratio.

4.4.2 Multi-frequency source kernels

We stack the monochromatic source kernels over a frequency band, during which monochromatic kernels interfere with each other. In areas where these kernels share common sensitivity, the magnitude of sensitivity increases due to stacking. In other areas, the kernels destructively interfere and the magnitude decreases. Therefore, we observe that the direct Rayleigh waves in C_{ZZ} and C_{RR} are sensitive to sources in the in-line areas (Figure 4.4a, 4.4b, 4.4e, and 4.4f), the so-called stationary-phase zone (e.g. Snieder, 2004). In this case we observe the majority of the sensitivity on the right-hand side of the model because we use a time window around the causal direct Rayleigh waves (Figure 4.1b). If we increase the in-line source strength, the traveltime and waveform energy will increase. This expectation fits the sensitivity sign in the in-line areas (Figure 4.4a, 4.4b, 4.4e, and 4.4f). For arrivals near the zero-time location (Figure 4.1b), we observe that both ZZ and RR taveltime and waveform-energy kernels are sensitive to seismic sources between the two sensors (Figure 4.4c, 4.4d, 4.4g, and 4.4h).

We also observe the azimuthal effect in the RR kernels. Compared to the ZZ source kernels (Figure 4.4a, 4.4c, 4.4e, and 4.4g), the RR source kernels (Figure 4.4b, 4.4d, 4.4f, and 4.4h) possess less sensitivity to sources on the sidelobe areas. Thus for direct Rayleigh waves, we can use RR to focus on in-line seismic sources (Figure 4.4b and 4.4f) and decrease the error in Rayleigh-wave dispersion measurements due to anisotropic source distributions (e.g. van Wijk *et al.*, 2011; Haney *et al.*, 2012; Xu & Mikesell, 2017). For Rayleigh waves near the zero point in crosscorrelations, where

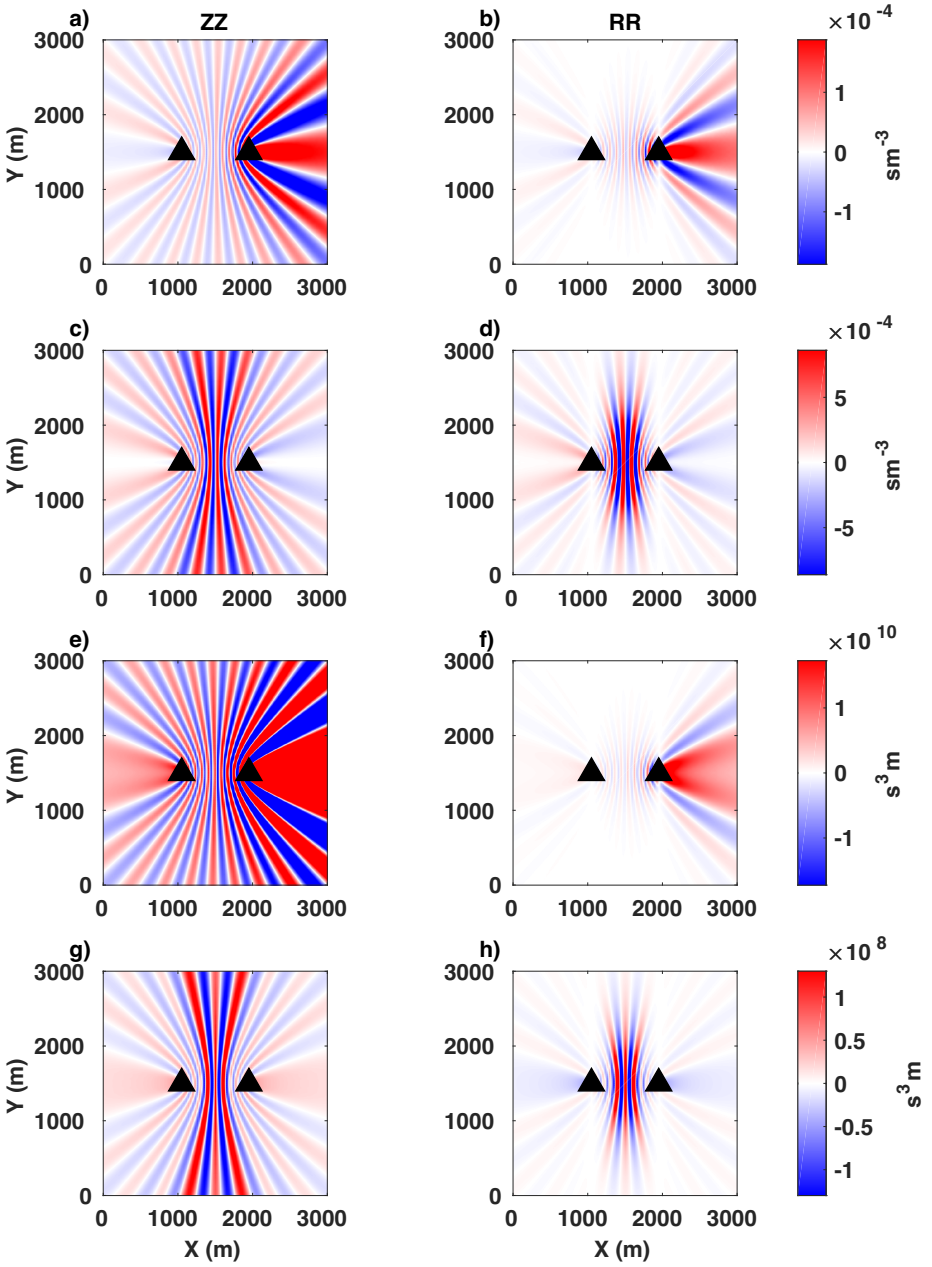

Figure 4.4: 2-8 Hz traveltime (a,b,c,d) and waveform-energy (e,f,g,h) source kernels for Rayleigh waves in C_{ZZ} (left) and C_{RR} (right). a,b,e,f are for direct Rayleigh waves (0.5 s to 0.8 s in Figure 4.1b); c,d,g and h are for early-arrival Rayleigh waves (-0.2 s to 0.2 s in Figure 4.1b).

seismic sources occur between sensors, RR should help to locate the sources better than ZZ (Figure 4.4d and 4.4h vs 4.4c and 4.4g).

4.5 Source Estimation Synthetic examples

We present three synthetic source inversion examples to demonstrate that multicomponent crosscorrelations (C_{RR} and C_{ZZ}) better estimate anisotropic source distributions than C_{ZZ}. We use 9 sensors in a square array in all examples. The smallest distance between two adjacent sensors is 450 m. We assume that all seismic sources are distributed on the free surface. In the first two examples, the seismic sources occur within the array area, with the sources distributed outside of the array in the third example. Each source emits a 10 Hz Ricker wavelet with an amplitude factor of 10^{15}. The subsurface is the same homogeneous medium (Table 4.1 True model) as in Section 4.4. We assume that we know the subsurface structure and the source wavelet in the inversions. Thus we simulate the observed and synthetic crosscorrelations following Section 4.4. We use the simulated wavefield to calculate the source kernels (Equation 4.15). We use both C_{ZZ} and $C_{ZZ} + C_{RR}$ in the inversions with waveform and traveltime misfit functions (Equation 4.1 and 4.2). In using $C_{ZZ}+C_{RR}$ in misfit functions, we weight the crosscorrelaions by normalizing the amplitudes of C_{ZZ} and C_{RR} by the corresponding C_{ZZ} and C_{RR} waveform maxima of all sensor pairs, respectively. We do this to both synthetic and observed data using their respective maxima. As a consequence, we scale the ZZ and RR waveform kernels by the synthetic C_{ZZ} and C_{RR} waveform maxima, respectively. We conducted the inversions without scaling the kernels and achieved similar results; however, to keep the system of equations self-consistent the kernels should be scaled in the same way the waveforms are scaled.

We present the entire inversion algorithm as pseudocode (Algorithm 1). We adopt the frequency band extension strategy (e.g. Virieux & Operto, 2009). We use a large time window in the waveform inversion (Table 4.2) because in the crosscorrelations the Rayleigh waves can arrive between time zero and the direct-wave arrival time, depending on the different source locations (e.g. Wapenaar & Fokkema, 2006). This time-windowing strategy is in contrast to global earthquake seismology where we have accurate predictions of arrival times for body waves and Rayleigh waves (e.g. Maggi *et al.*, 2009). If we use a narrow time window in the waveform inversion, artifacts appear outside the narrow time windows. However, the narrow time window works well for the traveltime inversion, because the traveltime inversion simply move waveforms forward or backward in time and thus no artifacts appear. We use the same frequency band to calculate the waveform source kernels and waveform misfit (Equation 4.1). We measure the traveltime misfits (Equation 4.2) over the whole frequency band because this measurement is more robust than in narrow frequency bands. We set the initial source strength at each sensor location to be zero,so we can avoid singularity in receivers. We smooth the source strength distributions in the traveltime inversions (see Algorithm 1), but not in the waveform inversions, because the traveltime source kernels possess narrower sensitivity bands than the waveform kernels (Figure 4.3 and 4.4). In practice, it is common to smooth the model parameters or gradients in wave-equation based tomography (e.g. Tape *et al.*, 2007) and active-source waveform inversion (e.g. Groos *et al.*, 2017). The inversion results are normalized by the maximum source strength, because we focus on relative source strength distributions, instead of absolute strength distributions.

Algorithm 1 Inversion algorithm

Normalize observed crosscorrelations by global maximums in C_{ZZ} and C_{RR};
for ith iteration **do**
    forward source distribution model on N_i using Equation 4.4 and normalize crosscorrelations;
    calculate the misfit, χ_i, over time window using Equation 4.1 (waveform) or Equation 4.2 (traveltime);
    calculate adjoint source, f, using Equation B.15 (waveform) or Equation B.9 (traveltime);
    calculate the kernel, K, using Equation 4.15;
    for each step size, p_j **do**
        update N_i with p_j using Equation 4.20, (smoothing the updated source model with a 30 m 2D Gaussian filter in the traveltime inversion);
        forward model using source distribution and Equation 4.4;
        normalize crosscorrelations;
        calculate the misfit, χ_j;
    find the minimum misfit, $min(\chi_j)$, and the corresponding p_j ;
    if $min(\chi_j) < C_u\chi_i$ **then**
        update N_i and achieve N_{i+1} using Equation 4.20,(smoothing the updated source model with a 30 m 2D Gaussian filter in the traveltime inversion);
    else
        extend frequency band
    In the last frequency band
    if $|N_{i+1} - N_i|/|N_i| < C_s$ **then**
        stop inversion

Table 4.2: Traveltime and waveform inversion scheme details

	Traveltime	Waveform
Frequency band used in calculating misfit function and kernel	2-4/6/8/12/16 Hz	
Time window	0.6 s centered at the peak of crosscorrelation	-1 to 1 s
Crosscorrelation normalization term	Maximum in all C_{ZZ} or C_{RR}	
Smooth source strength per iteration	Yes	No
Update criteria, C_u	100%	99%
Stop criteria, C_s	0.01	0.01

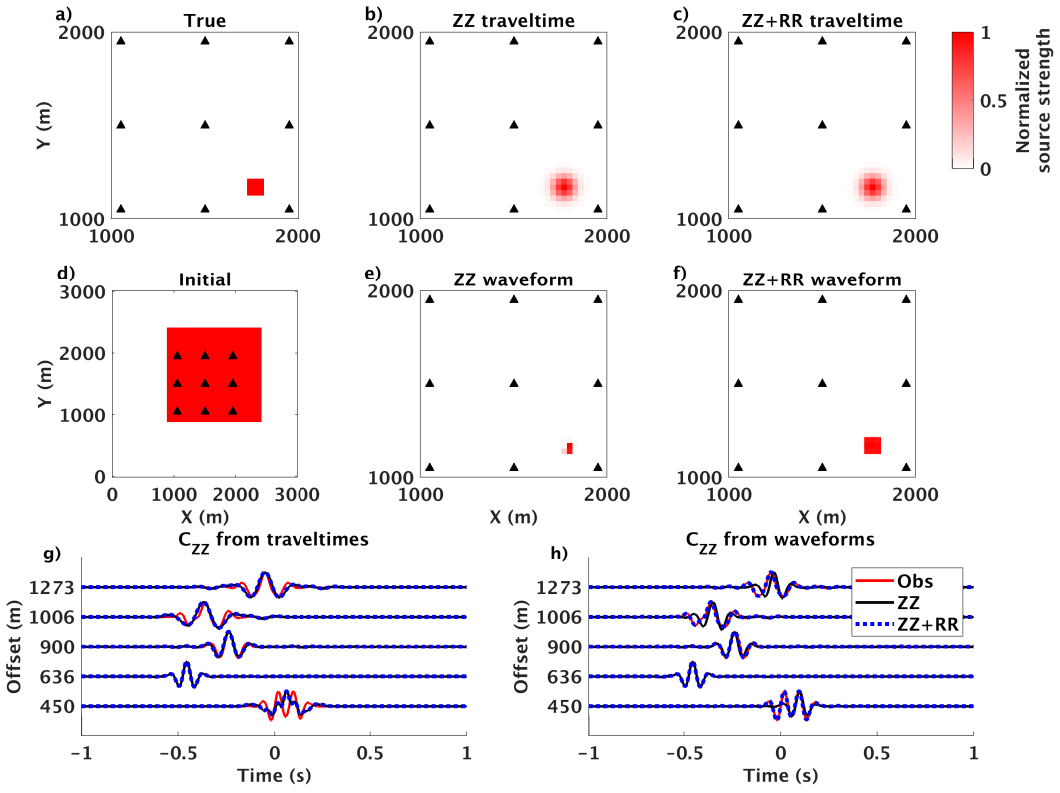

Figure 4.5: One source within array inversion results and the corresponding C_{ZZ} waveforms. a) The true source strength distribution is zeros everywhere except an in-array source area (square). Triangles are receivers. From the initial seismic source distribution model (d), we invert with the ZZ traveltimes (b), $ZZ + RR$ traveltimes (c), ZZ waveforms (e), and $ZZ+RR$ waveforms (f). We plot the synthetic C_{ZZ} based on the traveltime inversion results in (g) and the waveform inversion results in (h), along with the observed C_{ZZ}. Each waveform here is normalized by its maximum amplitude for comparison. Note that the initial source strength (d) at each receiver location is zero and is masked by the triangles.

4.5.1 Example 1: One source within array

The sensors surround one source area in this case (Figure 4.5a). The inversion results (Figure 4.5b, 4.5c, 4.5e, and 4.5f) estimate the source locations and strengths accurately, although the initial source distribution model (Figure 4.5d) is far from the true source model. We observe that the inverted source distribution from the waveform inversion (Figure 4.5e and 4.5f) are closer to the true source distribution than from the traveltime inversion (Figure 4.5b and 4.5c); the synthetic waveforms (Figure 4.5h) from the waveform inversion results also fit the observed C_{ZZ} better. This is because the waveforms contain not only traveltime information, but also information such as relative amplitudes. Thus, the waveform inversion performs better than the traveltime inversion. We note that the multicomponent data does not improve the source distribution estimation when we only use traveltime information. The $ZZ + RR$ traveltime inversion gives a similar source estimation to the ZZ inversion. However, multicomponent data do help constrain the waveform inversion. In the waveform inversions, $ZZ + RR$ better estimates the source shape than ZZ alone. Moreover, the synthetic C_{ZZ} waveforms from the multicomponent inversion are closer to the waveforms of the observed C_{ZZ} (Figure 4.8g and h).

4.5.2 Example 2: Two sources within array

Two sources in the array make the observed crosscorrelation waveforms more complex than in the one-source case. We observe that more arrivals exist in the crosscorrelations from the two-source area (Figure 4.6h) than from one-source area (Figure 4.5h). We use the same initial source model as in the one-source case. The initial source strength model is far away form the true source model, so the corresponding synthetic waveforms are not similar to the observed waveforms. As the traveltime in-

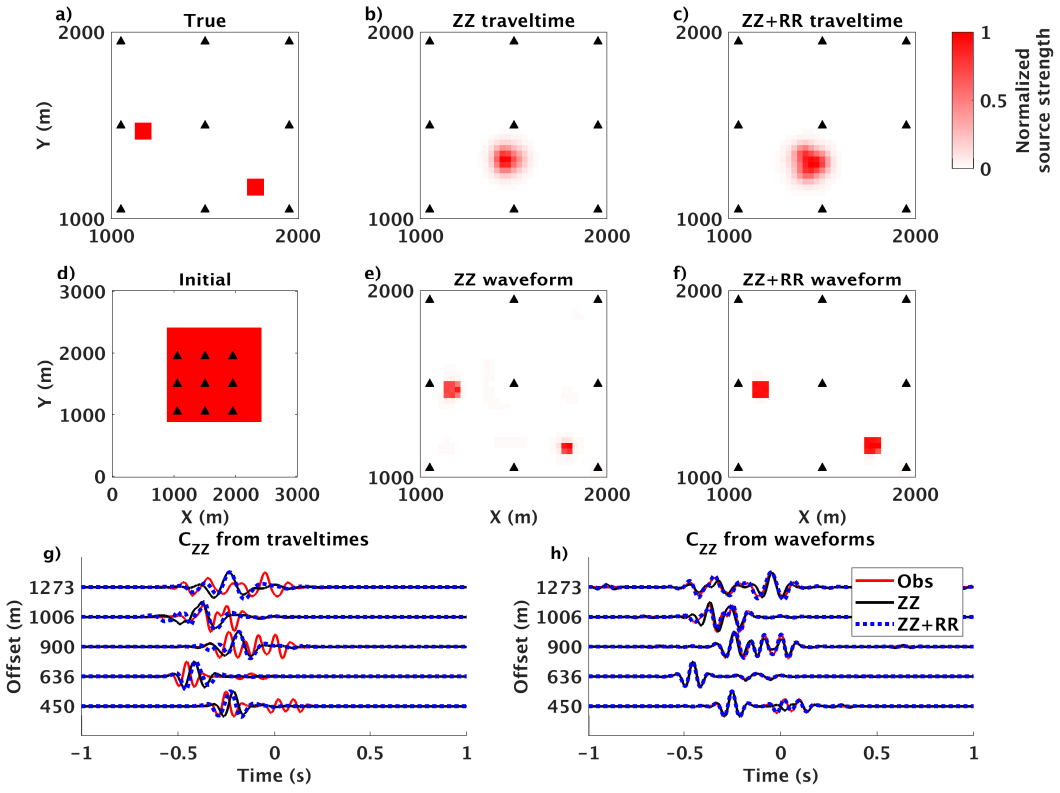

Figure 4.6: Two sources within array inversion results and the corresponding waveforms. a) The true source strength is zeros everywhere except two source areas (squares) within the array (triangles). From the same initial source distribution model (d) as in Figure 4.5, we invert the ZZ traveltimes (b), $ZZ + RR$ traveltimes (c), ZZ waveforms (e), and $ZZ + RR$ waveforms (f). We plot the synthetic C_{ZZ} based on the traveltime inversion results in (g) and the waveform inversion results in (h), along with the observed C_{ZZ}. Each waveform here is normalized by its maximum amplitude for comparison. Note that the initial source strength (d) at each receiver location is zero and is masked by the triangles.

version mainly moves waveforms on the time axis, the synthetic waveforms from the traveltime inversion do not fit the observed data. For complex waveforms in the observed data (Figure 4.6g), where there are more than one arrival, we determine that the synthetic data from the traveltime inversions will not fit the observed data. Thus the traveltime inversion gives incorrect, single-location estimations (Figure 4.6b and 4.6c). However, the waveform inversion can handle the complex observed data because the waveform inversion can fit multiple arrivals. We estimate accurate source locations and relative strengths with the waveform inversion, and the synthetic C_{ZZ} from the inversion results fit the observed C_{ZZ} well (Figure 4.6h). $ZZ+RR$ waveform inversion recovers the source shapes better than ZZ waveform inversion.

4.5.3 Example 3: Sources outside of array

Seismic sources lie outside of the array in this example. Thus neither method perfectly recovers the source shape as in the two previous examples (Figure 4.7). With the traveltime inversions, we determine that the inversion accurately provides an estimation of the directions of source locations, along with artifacts inside the array (Figure 4.7b and 4.7c), while the waveform inversion recovers the source location decently well (Figure 4.7e and 4.7f). Although the $ZZ + RR$ waveform inversion gives a similar result as the ZZ waveform inversion, the final misfit for $ZZ + RR$ is less than for ZZ (Figure 4.8f).

4.5.4 Analysis of inversion results

We observe that in the traveltime inversion examples, multicomponent data do not help to resolve the source distribution. In Example 1, $ZZ + RR$ gives a simiar misfit over the whole frequency band (2-16 Hz) as ZZ (Figure 4.8a). We ignore interpretation of Example 2 because the traveltime inversion does not work for this

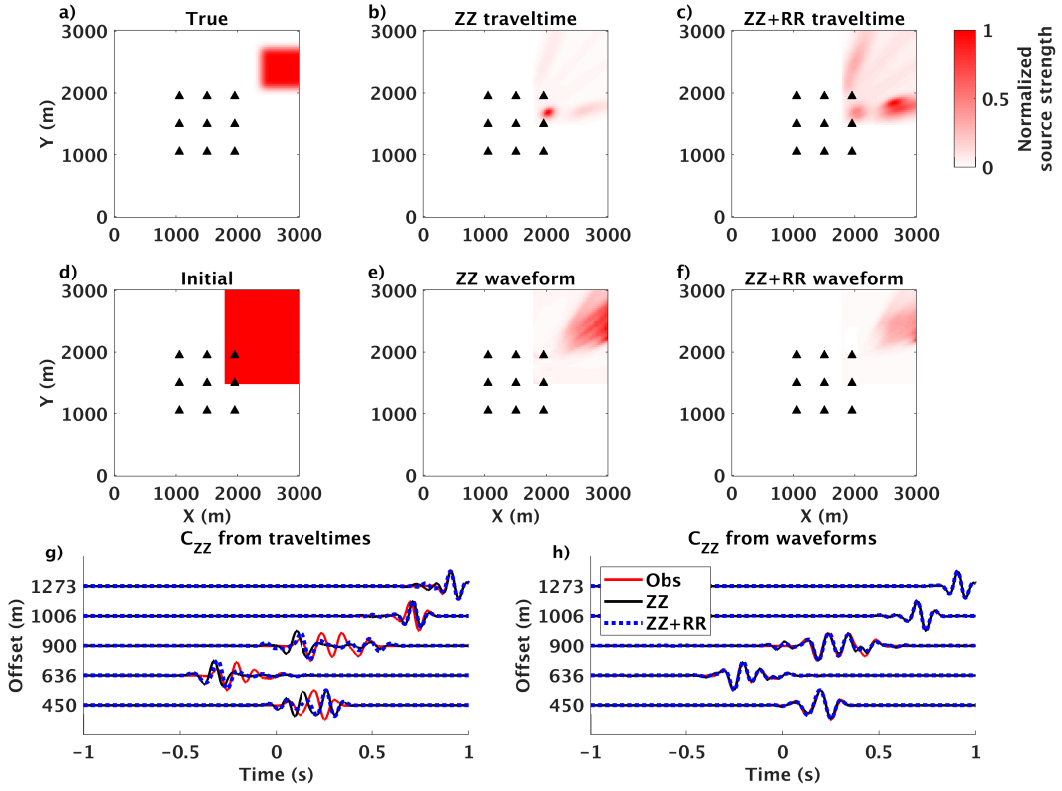

Figure 4.7: Source out-of-array inversion and the corresponding waveforms. a) The true source strength is zeros everywhere except the out-of-array source area (square). From an initial source model (d), we invert the ZZ traveltimes (b), $ZZ + RR$ traveltimes (c), ZZ waveforms (e), and $ZZ+RR$ waveforms (f). We plot the synthetic C_{ZZ} based on the traveltime inversion result in (g) and based on the waveform inversion result in (h), along with the observed C_{ZZ}. Each waveform here is normalized by its maximum amplitude for comparison.

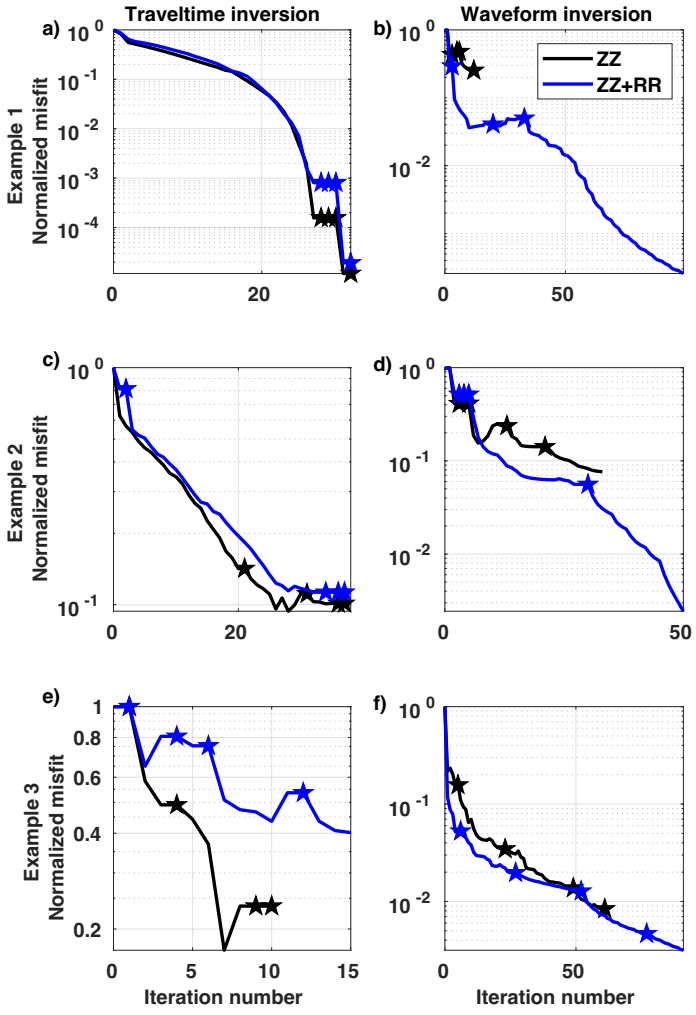

Figure 4.8: Traveltime and waveform inversion misfit comparisons. We show Example 1 (a and b), Example 2 (c and d), and Example 3 (e and f). The stars indicate when we extend the frequency bands (Table 4.2). We show the misfits over the whole frequency band, 2-16 Hz, relative to the initial misfit at each iteration.

case as we explain in Section 4.5.2. When sources are outside of the array, $ZZ + RR$ gives a weaker artifact inside the array (Figure 4.7c) than does ZZ, but still neither traveltime inversion gives a correct result.

The multicomponent data improve the waveform inversion in all three examples. $ZZ + RR$ better estimates the source shapes for in-array sources and gives lower misfits than ZZ regardless of whether sources are in the array or not (Figure 4.8b, 4.8d and 4.8f). In Example 3, we observe that $ZZ + RR$ provides a similar estimation of seismic source distribution and a close misfit to ZZ (Figure 4.8f).

We also present seismic source estimation using matched-field processing (MFP) on the three examples (Figure B.2). The MFP results recover true source locations, but also many artifacts. We demonstrate that MFP is equivalent to a waveform source kernel where the initial source strengths are zeros everywhere (Appendix B.3). These artifacts are suppressed by the waveform inversion and thus disappear in the inversion results (Figure 4.5e, 4.6e and 4.7e). One could use MFP results as an initial source model for the waveform inversion.

4.6 Discussion

In this paper we introduce the theory needed to estimate source strength distribution from crosscorrelations using multicomponent full-waveform inversion. We apply this theory to multicomponent field data in a companion paper, but here we comment on common data processing notions for completeness. To calculate ambient seismic noise crosscorrelations, one usually adopts pre-processing procedures, such as time-domain normalization, frequency-domain normalization, or various stacking procedures (e.g. Shapiro *et al.*, 2005; Yao *et al.*, 2006). The normalization procedures change the crosscorrelation waveforms and spectra (e.g. Bensen *et al.*, 2007; Groos *et al.*, 2012),

as well as the apparent source strength distribution (e.g. Fichtner, 2014). In order to estimate true source strengths, we do not use these normalization procedures. However, because the stacking procedure can mitigate random uncorrelated noise (e.g. Bensen *et al.*, 2007), in real crosscorrelations, stacking is used; keeping in mind that it is difficult to suppress the main source of noise in crosscorrelations, which is localized correlated noise.

We present noise-free examples in this paper to demonstrate the physics of the problem and the properties of the adjoints. We address the topic of noise more thoroughly in our companion paper, noting that the quality of vertical- and horizontal-component data can be improved by burying receivers below the surface (e.g. Hutt *et al.*, 2017). For clarity here, we present three simple examples of one or two seismic sources within or outside of the array. The maximum number of sources we can estimate depends on the chosen misfit function (i.e. traveltime or waveform), the array geometry (i.e. the number of sensors and the inter-sensor distance), and the complexity of the sources (if sources cancel each other, e.g. Wapenaar & Fokkema, 2006; Halliday & Curtis, 2008). Further study of the topic of how many sources can one locate is beyond the scope of this research.

We make four assumptions in the crosscorrelation source distribution inversion procedure presented here:

1. seismic sources are only distributed on the free surface;

2. seismic sources are independent from each other;

3. the subsurface velocity model is known;

4. the source spectral shapes are similar and known.

We make the first assumption because we are concerned with only fundamental mode Rayleigh waves (e.g. Halliday & Curtis, 2008). Moreover, the ambient seismic noise > 2 Hz is mainly due to human activity (e.g. Yamanaka *et al.*, 1993) and composed of surface waves. These seismic sources (e.g. traffic) usually occur on the surface or at shallow depths. We note that could use the same theory and focus on body waves in the crosscorrelations to locate seismic sources in depth. However, reverse-time migration is commonly used to locate the microseismic sources (e.g. Artman *et al.*, 2010). We present the link between the crosscorrelation source inversion and microseismic reverse-time migration in Appendix B.3. The second assumption is often made in seismic interferometry (e.g. Weaver & Lobkis, 2001). We discuss the third assumption in this section, and a discussion of the fourth assumption is provided in our companion paper, which considers field data.

Biased subsurface velocity models have been shown to lead to biased source locations (e.g. Billings *et al.*, 1994; Eisner *et al.*, 2009). We use two incorrect velocity models (Table 4.1 Higher and Lower), where one has higher and the other has lower velocities than the true velocity model. We use the same data, the same inversion strategies and the same initial source models as in Section 4.5. We observe that we do not recover accurate source locations, shapes of source areas, nor the number of source areas with the incorrect velocity models (Figure 4.9 and 4.10). This phenomenon is expected because with these incorrect velocity models, the crosscorrelations attribute the source to incorrect locations. For the same phase of a crosscorrelation, $\omega(r_{As} - r_{Bs})/c$ in Equation 4.24, if we use an incorrect velocity, the $r_{As} - r_{Bs}$ will be larger or smaller than when using true velocity. Therefore the source inversion will place sources at the wrong locations (Figure 4.9 and 4.10).

We observe that the waveform inversion for all three synthetic data achieves the lowest final misfit with the true velocity model, as does the traveltime inversion for one source within the array (Figure 4.11). This observation indicates that one can potentially estimate the source distribution and subsurface velocity structures through one inversion because the true source distribution and true subsurface velocities give a global minimum in the misfit function (Figure 4.11a, 4.11d, 4.11e, and 4.11f). In practice, one estimates the source and velocity model iteratively (e.g. Lee *et al.*, 2014) or simultaneously (e.g. Sager *et al.*, 2018). We also observe that the multicomponent data, $ZZ+RR$, constrain the estimation better because the final normalized waveform misfit for the true velocity model is the smallest and for the incorrect velocity model is larger than ZZ.

4.7 Conclusion

We estimate the anisotropic source distribution of Rayleigh waves with vertical and multicomponent crosscorrelation inversion in this paper. We assume that we know the subsurface structure. Through three synthetic examples, we show that multicomponent crosscorrelations ($C_{ZZ} + C_{RR}$) do not help the traveltime inversion, but do help to resolve seismic source distributions more accurately than only the vertical crosscorrelations (C_{ZZ}) in the waveform inversion. For the waveform inversion, both C_{ZZ} and $C_{ZZ} + C_{RR}$ provide accurate source distributions for seismic sources within array, while $C_{ZZ} + C_{RR}$ estimate the source shapes better. The $C_{ZZ} + C_{RR}$ waveform inversion gives a lower misfit than C_{ZZ} for sources within and outside of the array. We also note that the crosscorrelation waveform inversion performs better than the traveltime inversion. If the initial source model is far from the true source distribution, the traveltime inversion can not fit the observed data, and thus gives biased estima-

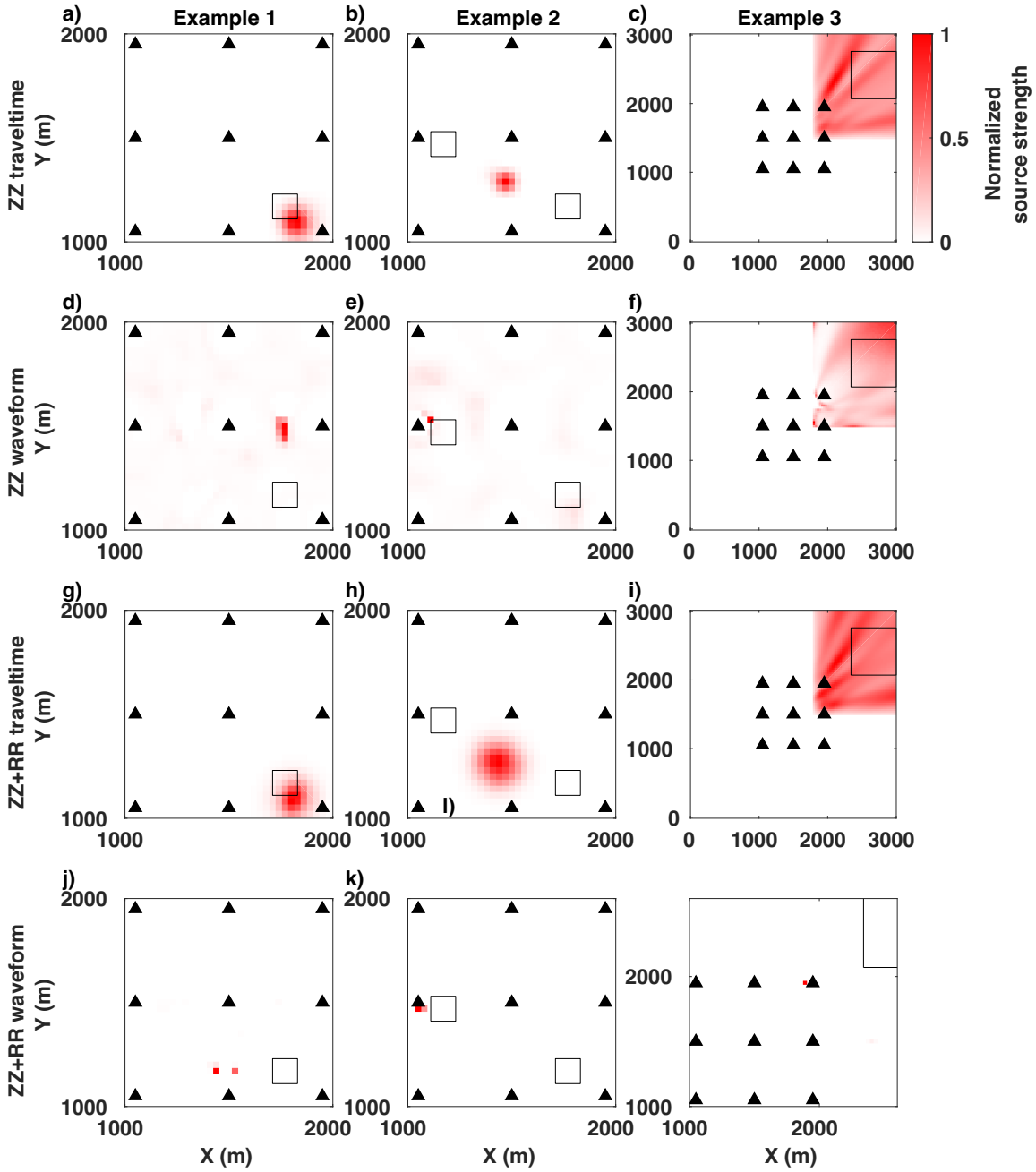

Figure 4.9: Source inversion results with a higher-velocity model (Table 4.1 higher). The black empty squares indicate the shapes and locations of the true sources. We only show the Example 3 ZZ+RR waveform result in a certain area because the source locations from the inversion are within this area. The initial models are as same as in Section 4.5.

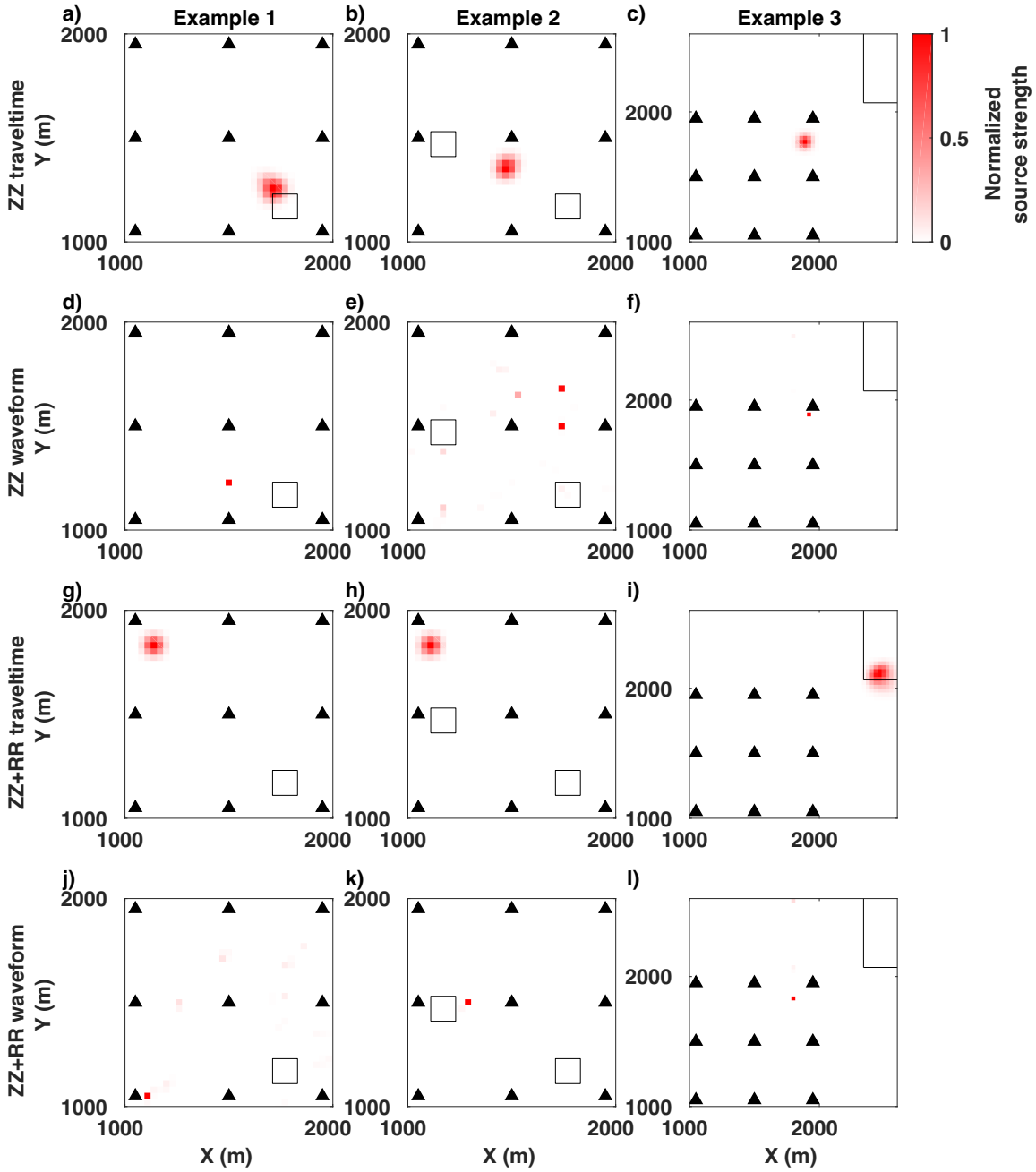

Figure 4.10: Source inversion results with a lower-velocity model (Table 4.1 lower). The black empty squares indicate the shapes and locations of the true sources. We only show the Example 3 results in a certain area because the source locations from the inversion are within this area. The initial models are as same as in Section 4.5.

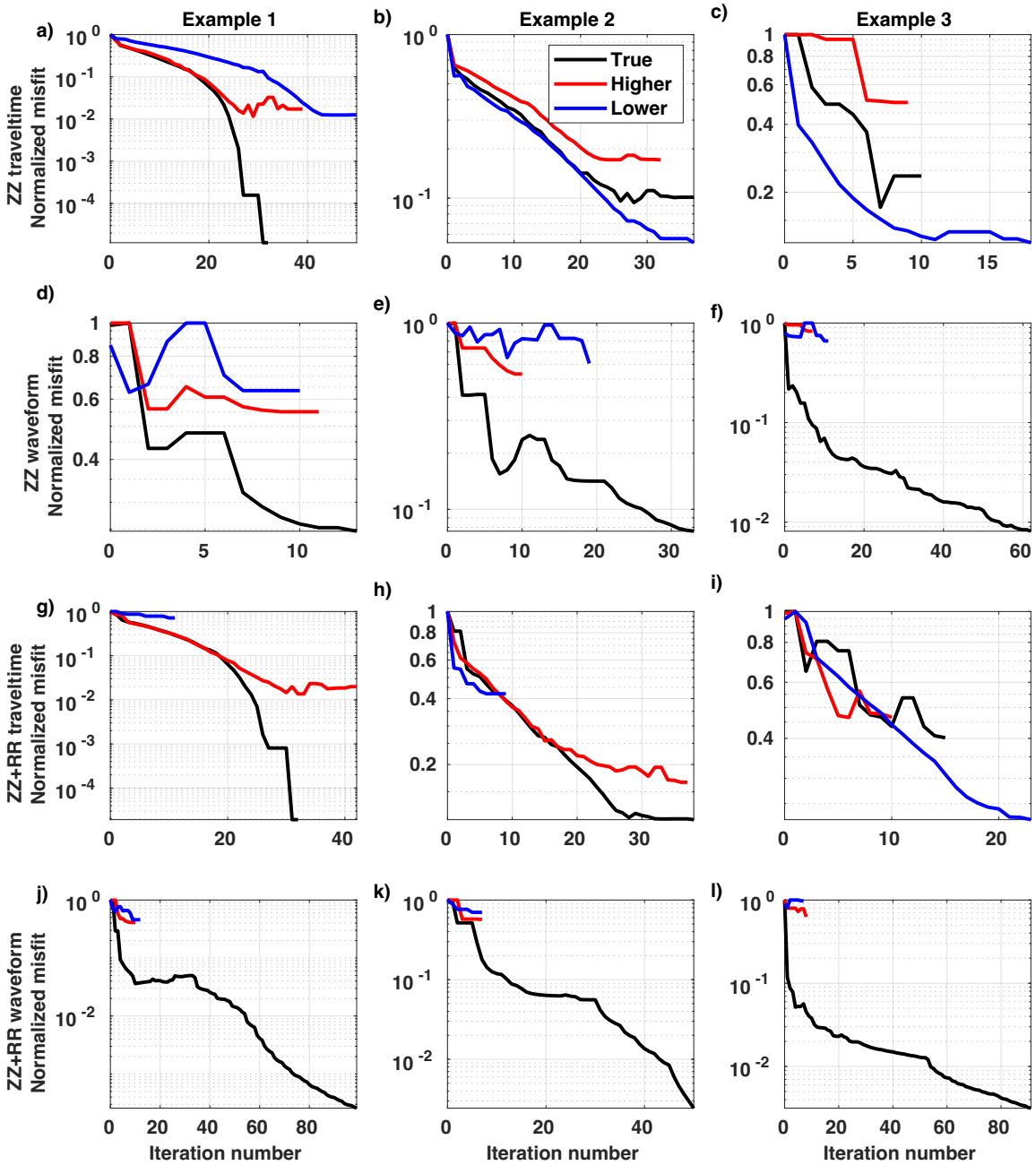

Figure 4.11: Traveltime and waveform inversion misfit curves with true, higher and lower velocity models (Table 4.1).

tions. The waveform inversion is more robust to the initial source model because the waveform inversion can fit complex observed waveforms with multiple arrivals. If sources are outside of array, the traveltime and waveform estimate rough directions instead of exact source shapes. Neither traveltime or waveform inversion works if the subsurface velocity model is incorrect. However, for the waveform inversion and the in-array one-source traveltime inversion, the true subsurface velocity model can give lower final misfit compared to incorrect velocity models. $C_{ZZ} + C_{RR}$ makes the waveform misfit difference even larger than C_{ZZ}, and thus better constrains estimation of the seismic source distribution and subsurface velocity model. The source inversion we use in this paper not only handles seismic sources located at the free surface, but also in depth.

CHAPTER 5:

RAYLEIGH-WAVE MULTICOMPONENT CROSSCORRELATION-BASED SOURCE STRENGTH DISTRIBUTION INVERSIONS. PART 2: A COMPLETE WORKFLOW FOR REAL SEISMIC DATA

This chapter has been submitted to *Geophysical Journal International*

5.1 Summary

Estimation of ambient seismic source distributions (e.g. location and strength) can aid studies of seismic source mechanisms and subsurface structure investigations. One can invert for the ambient seismic (noise) source distribution by applying full-waveform inversion (FWI) theory to seismic (noise) crosscorrelations. This estimation method is especially applicable for seismic recordings without obvious body-wave arrivals. Data preprocessing procedures are needed before the inversion, but some preprocessing procedures commonly used in ambient noise tomography can bias the ambient (noise) source distribution estimation and should not be used in FWI. Taking this into account, we propose a complete workflow from the raw seismic noise recording

through preprocessing procedures to the inversion. We present the workflow with a field data example in Hartoušov, Czech Republic, where the seismic sources are CO_2 degassing areas at Earth's surface (i.e. a fumarole or mofette). We discuss factors in the processing and inversion that can bias the estimations, such as inaccurate velocity model, anelasticity and array sensitivity. The proposed workflow can work for multicomponent data across different scales of field data.

5.2 Introduction

Knowledge of the ambient seismic source distribution (e.g. strength and location) is important in many research areas. For example, in investigating the subsurface with crosscorrelation-based seismic interferometry, one needs the source information to correct the empirical Green's functions or surface-wave dispersion curves if the seismic sources are not isotropically distributed in all directions around sensors (e.g. Yao & Van Der Hilst, 2009; Nakata *et al.*, 2015; Cheng *et al.*, 2016). When monitoring changes in the subsurface with direct waves in seismic crosscorrelations, one needs to assess or revise the monitoring results based on changes in the seismic source(s) (e.g. Delaney *et al.*, 2017; Takano *et al.*, 2019). In addition, spatial and temporal distributions of natural seismic sources (e.g. ocean microseism) can aid studies of the actual source mechanism (e.g. Cessaro, 1994; Juretzek & Hadziioannou, 2016).

To investigate the ambient (noise) seismic source distribution, one can use a traditional imaging method or an adjoint-based inversion method. The imaging methods (e.g. matched-field processing) mainly focus on the source location, and do not provide physical source properties like strength or amplitude (e.g. Cros *et al.*, 2011). In contrast, the adjoint-based inversion method can estimate both source location and strength. Tromp *et al.* (2010) and Fichtner *et al.* (2017) derived an adjoint for

crosscorrelations, and Ermert *et al.* (2017) applied this crosscorrelation adjoint to long period (over 100s) seismic crosscorrelations to study Earth's hum. For seismic sources such as tremors and ambient seismic sources, there are usually no clear body-wave arrivals in the seismic recordings and mainly traditional imaging methods have been applied to the seismic crosscorrelations (e.g. Obara, 2002; Zeng & Ni, 2010; Corciulo *et al.*, 2012), largely composed of surface waves.

To make a comparison between traditional methods and the adjoint-based inversion, Xu *et al.* (2019) show that the matched-field processing method can be written as the crosscorrelation waveform-adjoint sensitivity kernel with zero initial sources. For surface wave studies, Xu *et al.* (2019) further demonstrated that Rayleigh-wave multicomponent crosscorrelations can better constrain estimation of the source distribution compared to vertical-component crosscorrelations alone. The multicomponent data are vertical (Z) and radial (R) components, where the R direction is parallel to a line or great-circle path between two sensors. We call the crosscorrelation adjoint inversion for seismic sources as the *source inversion method* in this paper.

The source inversion method is well developed in theory, but in practice still requires preprocessing of the raw seismic recordings. Some procedures are the same as the preprocessing in ambient noise tomography (ANT, Shapiro *et al.*, 2005), such as stacking and excluding high-amplitude transient signals (i.e. earthquakes). However, there are some differences between the two sets of preprocessing procedures because the final goal of ANT is to image structure (i.e. velocity models), which is different from the source inversion method used to image source distributions. For example, if one inverts for Earth's hum, one has to remove not only earthquakes, but also the primary microseism, which is normally the signal source for ANT. In addition, the

seismic source inversion method requires known Green's functions, while the focus of ANT is to recover Green's functions. It is easy to misuse some ANT preprocessing procedures (e.g. normalization) in seismic source studies (e.g. Tian & Ritzwoller, 2015) and these procedures can bias the consequent source estimation (e.g. Fichtner *et al.*, 2017). Thus the purpose of this study is to present clear data preprocessing procedures in a workflow for the source inversion method. We use an L_2 waveform misfit function in the inversion, and we use observed ambient seismic noise data in the Hartoušov mofette field (Figure 5.1), Czech Republic, as a field data example to demonstrate the workflow. The parameters in the workflow are easy to adjust based on different field scales.

We introduce the workflow from raw seismic recordings to the source inversion. In the crosscorrelation adjoint-based inversion used here (e.g. Ermert *et al.*, 2017; Xu *et al.*, 2019), there are two major assumptions:

1. the subsurface structure is known (i.e. the Green's function);

2. all potential seismic sources share a similar shape in terms of energy spectral density.

Thus in the workflow, we need to estimate both Green's function for the subsurface media and the source energy spectral density shape (Section 5.3). We then estimate the spatial source distribution of fumaroles from the field data, and compare our estimation to a field CO_2 flux map (Section 5.4). We finally discuss the effect of inaccurate subsurface models, especially the anelastic property, and insufficient sensitivity of the data to the source estimation (Section 5.5).

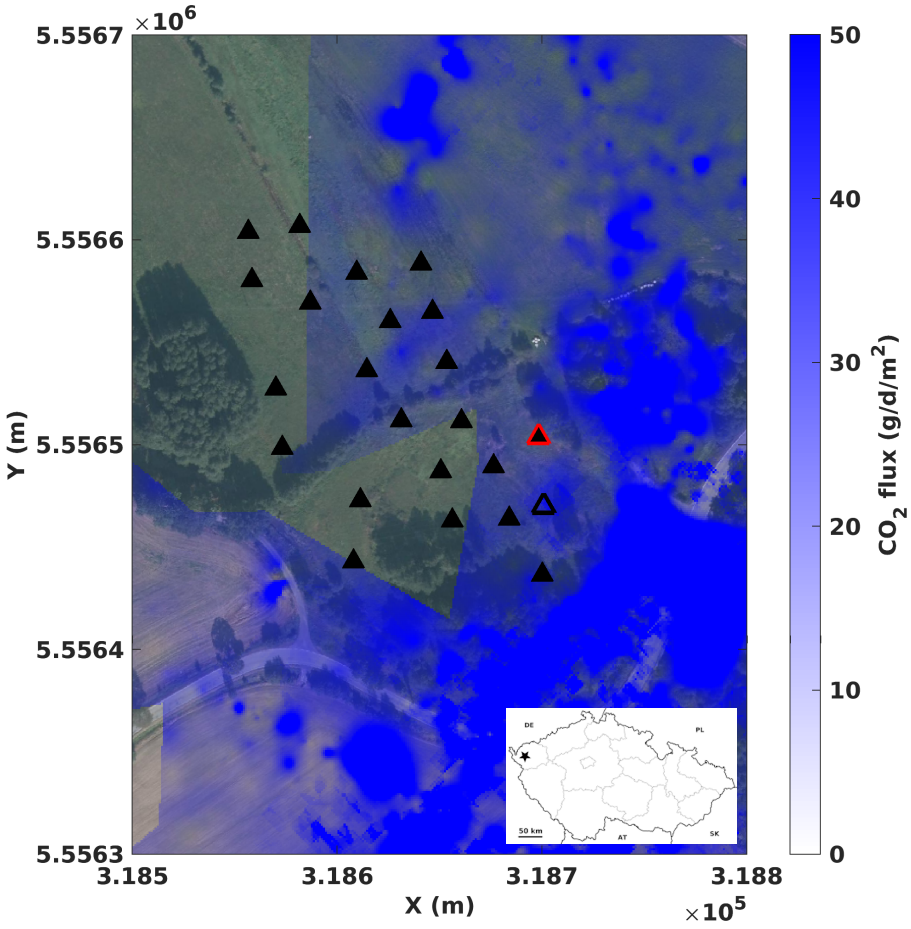

Figure 5.1: A site map of the seismic array and CO_2 gas-flux distributions. Each triangle is a geophone. The empty triangle is the noisy one. The red-edge triangle is the C601 sensor in Figure 5.3. The gas-flux data are from Nickschick *et al.* (2015) and were acquired from 2007 to 2013. The star in the inset shows the site location in Czech Repulic. The coordinates are in WGS84/UTM zone 33.

5.3 Workflow

We introduce the workflow in four steps. We first select data (i.e. observed crosscorrelations) based on a signal-to-noise ratio (SNR) criteria; process the data to isolate targeted source types (Section 5.3.1). We then estimate Green's functions (Section 5.3.2) and present a novel method to calculate source energy spectral density shape (Section 5.3.3). After these three steps, we introduce the source waveform inversion briefly (Section 5.3.4). The whole workflow is applicable for not only vertical component (Z), but also radial (R) component seismic recordings. Thus we can use Z-Z component crosscorrelations (C_{ZZ}) and/or R-R component crosscorrelations (C_{RR}) in the workflow.

5.3.1 Data selection

We refer to the crosscorrelations as the data in this source inversion method. Counter to normal ambient seismic crosscorrelations for ANT, as our focus is the ambient source location(s) and strength(s), we do not apply time-domain or frequency-domain normalization to the raw data prior to crosscorrelation because these procedures bias the source estimation result (e.g. Fichtner *et al.*, 2017). Without the common ANT processing procedures, however, the crosscorrelations for a seismic source study will be far from the true Green's functions if the source distribution is anisotropic. In this case, direct body and surface waves can arrive any time between time zero and the true (i.e. physical) direct-wave arrival time (e.g. Shapiro *et al.*, 2006; Snieder & Fleury, 2010). The events that arrive before the true direct wave are called spurious or non-physical arrivals under the assumption that the correlation approximates the Green's function (e.g. Mikesell *et al.*, 2009; Snieder & Fleury, 2010). In contrast to

ANT though, the spurious energy here is actually the important signal, used in the inversion to estimate the seismic source distribution.

In addition to so-called spurious arrivals in the correlations, noise can also be strong and thus affect the source estimation. This noise can consist of (1) uncorrelated random noise and (2) correlated noise, which can be in a similar frequency band as the targeted seismic sources. For the uncorrelated random noise, one can use stacking to suppress this noise, similar to the ANT processing (e.g. Bensen *et al.*, 2007). One can also use a SNR criterion to choose the crosscorrelations with the least uncorrelated noise among all crosscorrelations (e.g. Lin *et al.*, 2008). We propose here a SNR measurement similar to the SNR measurement algorithm in ANT (e.g. Bensen *et al.*, 2007).

We set two time windows – a signal and noise window. As stated above, the direct wave signal can arrive between time zero and the true arrival time, thus our signal window is different from the signal window in the ANT SNR algorithm, where the signal window is around the true surface-wave arrival time. We set our signal window be a wide time window that ranges from the acausal to causal times, encompassing our estimate of the slowest possible physical surface wave arrivals (-2 s to 2 s in Figure 5.2 for the fumarole example). For our noise window, we select two noise windows outside the signal window on both causal and acausal branches of crosscorrelations (-5 s to -3 s and 3 s to 5 s in Figure 5.2). The noise windows are away from the signal time window by one second in our case. We calculate the SNR as the ratio between the peak value in the signal window and the root-mean-square (RMS) value in the two noise windows. We set an SNR$>$ 15 criteria to select the crosscorrelations which we use in the source inversion method. The time parameters, such as time window

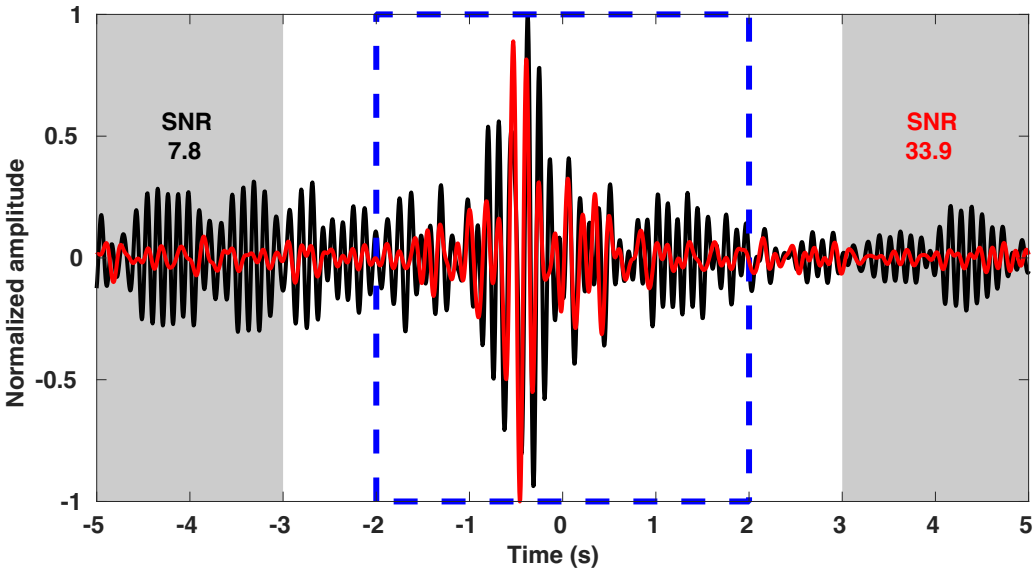

Figure 5.2: An example of the SNR measurement. The blue dashed box indicates the signal window. The two gray areas indicate the two noise windows. SNR is defined as the ratio of the peak in the signal window and the RMS in the two noise windows. We combine the recordings in the two noise windows and then calculate the RMS from the combined recordings. The black (left) and red (right) numbers in the gray areas indicate the SNR for the two waveforms, respectively. The waveforms are band-pass filtered between 3.5-10 Hz.

length, in the SNR measurements need to be adjusted based on different field data and array properties (e.g. interstation spacing).

It is also necessary to separate the correlated noise from the signal of interest as much as possible. Stacking works to suppress uncorrelated random noise, but can increase the amplitude of correlated noise (e.g. Shapiro *et al.*, 2006; Zeng & Ni, 2010). Thus the source inversion will not only image the targeted seismic source, but also any correlated noise sources. Therefore it is important to reduce or remove the correlated noise. For the continental-scale source studies like for microseisms, earthquake events are usually the strongest among all correlated sources and need to

be removed (e.g. Ermert *et al.*, 2017). At the near-surface scale, as in this fumarole example, the correlated noise is mainly due to anthropogenic activity (e.g. traffic) and tree waving. Unfortunately, these correlated noise sources and the fumaroles can both emit high-frequency (>2Hz) Rayleigh and/or body wave energy (Cheng *et al.*, 2016; Roux *et al.*, 2018; Estrella *et al.*, 2016). We avoid the trees waving by using data above the tree resonance frequency, approximately 2 Hz (e.g. Roux *et al.*, 2018), and we avoid the anthropogenic activity by using data recorded during the night when there is less anthropogenic activity compared to daytime (e.g. Yamanaka *et al.*, 1993).

We first analyze the ambient seismic recordings from 01:00 to 04:00 local time on 23 November 2016. During this time period, there are usually smaller wind speeds in inland areas than daytime (e.g. He *et al.*, 2013), and we assume that the main seismic sources during this time are fumaroles. We divide the 3-hour long raw data (01:00 - 04:00) into 60-s sections; then we remove the mean and linear trend in each section. Because all of the sensors in the array are the same, we do not need to remove the instrument response. We crosscorrelate these sections and then stack all crosscorrelations for each sensor pair. We bandpass filter the stacked crosscorrelations between 3.5 and 10 Hz. We monitor the SNR improvement as we stack more sections and find that the SNR drops dramatically around 03:30 (Figure 5.3a) in both C_{ZZ} and C_{RR}. The drop indicates that the number of station pairs with high-SNR (>15) crosscorrelations decreases. This SNR change is due to a different strong seismic source (Figure 5.3b, c), which has changed the correlation dramatically. This transient source could be human activity or another fumarole. If one looks more closely at the number of stations pairs, there are a few other small drops that are related to

other high-amplitude transient signals. We do not investigate these transient signals further, but because of this drop in SNR, we do not use the raw data after the 03:30 and study only the ambient seismic recordings from 01:00 to 03:30, a total of 2.5 hours, in this source inversion example.

We also winnow the C_{ZZ} waveforms based on the interstation distance. Small interstation-distance C_{ZZ} waveforms are less sensitive to source changes compared to large-distance waveforms (Appendix C.1). Furthermore, the ZZ sensitivity kernels do not change much with source changes when the interstation distance is small. However, due to the azimuth effect of the R component (e.g. Haney *et al.*, 2012; Xu & Mikesell, 2017; Xu *et al.*, 2019), the small-distance C_{RR} waveforms are still sensitive to source changes and help constrain source locations (Appendix C.1). Thus the small-distance C_{ZZ} waveforms do not add much benefit to the source inversion, but C_{RR} waveforms do. Therefore we ignore small-distance C_{ZZ} waveforms, but do not ignore C_{RR} waveforms with small interstation distances. In this study, we use C_{ZZ} waveforms when the interstation distance is larger than 50 m.

5.3.2 Green's function estimation

Seismic source studies commonly assume that the subsurface velocity model is known and thus use Green's functions based on the assumed velocity model. For the continental-scale source studies, one can choose a reference velocity model, like AK135 (Kennett *et al.*, 1995). However, for near-surface studies, one usually does not have a reference model and thus has to estimate the velocity model somehow. There are many approaches to estimate near-surface velocity models from ambient seismic data (e.g. Lin *et al.*, 2013; Cheng *et al.*, 2015). In this example, we estimate Rayleigh-wave phase velocities (Appendix C.2) and then use the phase velocities to calculate Green's func-

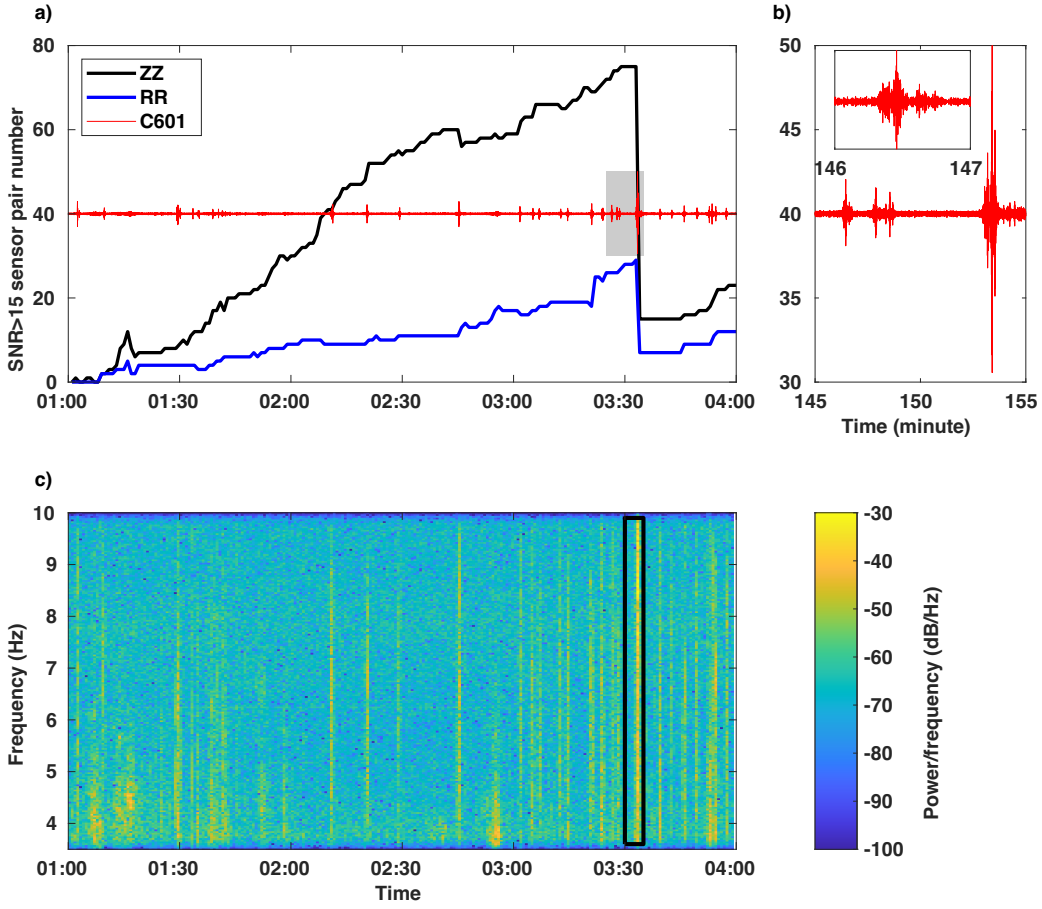

Figure 5.3: a) The number of sensor pairs with SNR>15 changes with time as we stack more time sections of correlations. The time axis is from 01:00 to 04:00 on 23 November 2016. The red line is the continuous seismic recording for the C601 geophone during this time period. The recording is bandpass filtered between 3.5 and 10 Hz. b) A zoom of the continuous recording in the gray area in a). The inset shows a zoom of the first event. c) The spectrogram of the C601 continuous recording in a) from the short-time Fourier transform; the window for the Fourier transform is 60 s. The high-power signal in the black box corresponds to the strong transient signal in b) and causes the drop in the ZZ and RR curves in a).

tions. We assume that the subsurface at the Hartoušov field is laterally-homogeneous, isotropic and elastic and thus use the far-field Rayleigh-wave Green's function from a vertical-force source to generate synthetic waveforms in the inversion:

$$G_{ZZ}(r,\omega) = \sqrt{\frac{1}{8\pi\omega r/c(\omega)}} e^{-i(\omega r/c(\omega)+\pi/4)}, \tag{5.1}$$

and

$$G_{RZ}(r,\omega) = \frac{H(\omega)}{V(\omega)} \sqrt{\frac{1}{8\pi\omega r/c(\omega)}} e^{-i(\omega r/c(\omega)-\pi/4)}, \tag{5.2}$$

where i is the imaginary unit, $c(\omega)$ is the surface-wave phase velocity, and r is the distance between the source and receiver. $H(\omega)/V(\omega)$ is the ratio of the horizontal-to-vertical motion (e.g. Haney *et al.*, 2012). These two Green's functions use the Rayleigh-wave phase velocity function from Appendix C.2 and the $H(\omega)/V(\omega)$ from Section 5.3.3. Notice that although accurate Green's functions are important for seismic source studies, our focus for this paper is the whole workflow for the source inversion, instead of estimating accurate individual Green's functions. We discuss the notion estimating both sources and structure together in Section 5.5.1.

5.3.3 Source energy spectral density estimation

We assume that all seismic sources share a similar energy spectral density shape (S_p^0). This assumption is valid in that the same types of natural ambient seismic sources possess a similar source mechanism, such as a river (e.g. Tsai *et al.*, 2012) or an ocean (e.g. Ardhuin *et al.*, 2011b). This assumption decreases the potential model space because we only need a ratio (N) to indicate the strength of each potential source (e.g. Ermert *et al.*, 2017; Xu *et al.*, 2019). To estimate S_p^0, we present a novel, data-driven approach.

We write the autocorrelation for each sensor as

$$\begin{aligned} C_{mm}(r_A, \omega) &= \int_V G_{mp}(r_A, r_s, \omega) G^*_{mp}(r_A, r_s, \omega) S_p(\omega) dr_s, \\ &= S^0_p(\omega) \int_V |G_{mp}(r_A, r_s, \omega)|^2 N(r_s) dr_s, \end{aligned} \tag{5.3}$$

where S_p and S^0_p are nonnegative (e.g. Xu *et al.*, 2019). We then combine the autocorrelation (Equation 5.3) and the far-field Rayleigh-wave Green's functions (Equations 5.1 and 5.2) as

$$C_{ZZ}(r_A, \omega) = S^0_Z(\omega) \int_V \frac{1}{8\pi\omega r_{As}/c(\omega)} N(r_s) dr_s = \frac{S^0_Z(\omega)}{\omega/c(\omega)} \int_V \frac{N(r_s)}{8\pi r_{As}} dr_s, \tag{5.4}$$

and

$$C_{RR}(r_A, \omega) = S^0_Z(\omega) \int_V \left[\frac{H(\omega)}{V(\omega)}\right]^2 \frac{1}{8\pi\omega r_{As}/c(\omega)} N(r_s) dr_s = \frac{S^0_R(\omega)}{\omega/c(\omega)} \int_V \frac{N(r_s)}{8\pi r_{As}} dr_s, \tag{5.5}$$

where r_{As} is the distance between a source (r_s) and the receiver (r_A). Noting that $S^0_R(\omega) = [H(\omega)/V(\omega)]^2 S^0_Z(\omega)$ The integral over V in Equations 5.4 and 5.5 represents a geometric relationship between the receiver and all seismic sources. The integral is independent of frequency, and thus we can write this integral as an amplitude normalization constant

$$D(r_A) = \int_V \frac{N(r_s)}{8\pi r_{As}} dr_s. \tag{5.6}$$

Finally, we write:

$$S_Z^0(\omega) = \frac{\omega C_{ZZ}(r_A, \omega)}{c(\omega) D(r_A)}, \tag{5.7}$$

$$S_R^0(\omega) = \frac{\omega C_{RR}(r_A, \omega)}{c(\omega) D(r_A)}. \tag{5.8}$$

We estimate $S_Z^0(\omega)$ and $S_R^0(\omega)$ using the same raw ambient seismic data in the observed crosscorrelations. We calculate the autocorrelations (C_{ZZ}, $C_{RR} = C_{EE} + C_{NN}$) for each sensor following the processing procedures in Section 5.3.1. We then transform the autocorrelations to the frequency domain. For each ZZ autocorrelation we normalize by the value of that autocorrelation at the lowest targeted frequency (D in Equations 5.7 and 5.8). For the corresponding RR autocorrelation we normalize by the ZZ value to preserve the H/V information. We then average the normalized autocorrelations among different sensors. We multiply the averaged autocorrelation with $\omega/c(\omega)$ to estimate $S_Z^0(\omega)$ and $S_R^0(\omega)$ (Figure 5.4). The S_Z^0 is different from S_R^0 due to the $H(\omega)/V(\omega)$ ratio as noted previously.

5.3.4 Source waveform inversion scheme

We are now ready to conduct the source inversion after the three previous steps. The inversion scheme has already been stated in detail (e.g. Ermert *et al.*, 2017; Xu *et al.*, 2019). Thus we describe the whole scheme briefly here. Notice one can define the misfit function not only on crosscorrelation waveforms as we do, but also on correlation symmetry (e.g. Ermert *et al.*, 2015) or on correlation envelope (e.g. Fichtner *et al.*, 2008; Bozdağ *et al.*, 2011). We choose the waveform misfit function because the waveform inversion can potentially recognize multiple seismic sources (e.g. Xu *et al.*, 2019). We define an L_2-norm waveform misfit function and present

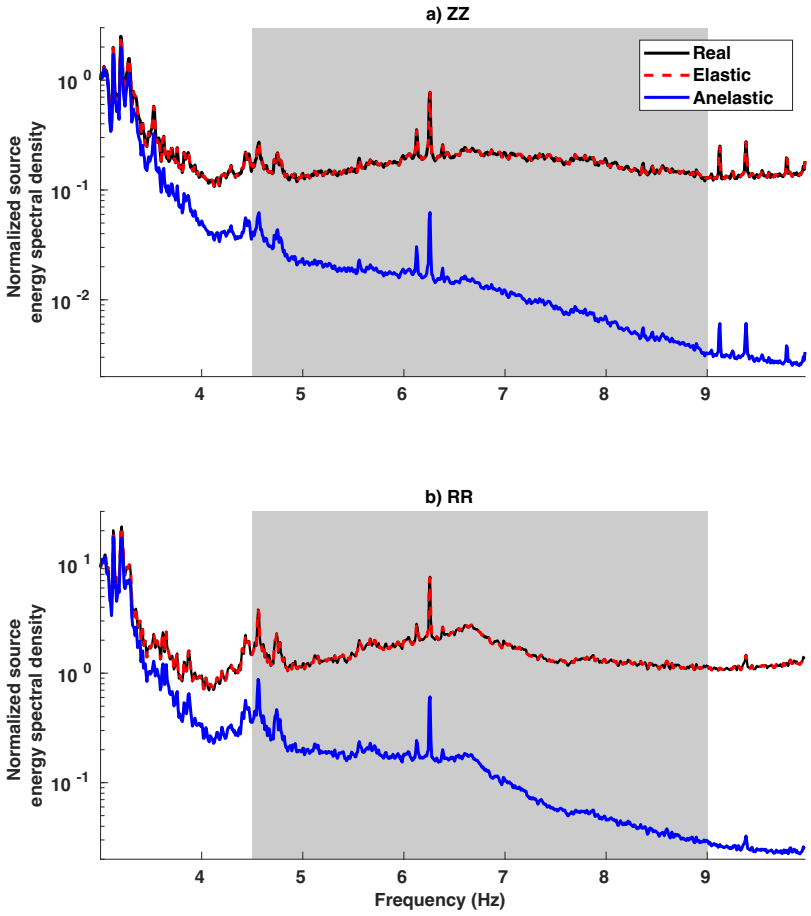

Figure 5.4: Normalized source energy spectral density estimations, S_Z^0 and S_R^0. We estimate S_Z^0 (a) and S_R^0 (b) (black lines) from the field data waveform autocorrelations C_{ZZ} and C_{RR}, respectively. We then use the two estimates in the forward model. In the forward model, if we use the elastic Green's function (Equation 5.1 and 5.2), our estimated source energy spectral densities (red dashed lines) are the same shape as the real source energy spectral density. If we use the anelastic Green's functions, we estimate incorrect densities (blue lines). Here the spectral density is for displacement wavefield (Appendix C.3). The gray areas indicate the frequency range we use in the waveform inversion, 4.5-9 Hz. Note here that we only focus on the shape, instead of the absolute values among real, elastic and anelastic estimations. All S_Z^0 and S_R^0 in this figure are normalized by the S_Z^0 at the lowest frequency.

both the time- and frequency-domain versions, respectively:

$$\chi = \frac{1}{2}\sum_{mn}\sum_{r_A r_B}\int [w(t)(C_{mn}(r_A, r_B, t) - C^o_{mn}(r_A, r_B, t))]^2 dt, \tag{5.9}$$

$$= \frac{1}{2}\sum_{mn}\sum_{r_A r_B}\int |w(\omega) *_\omega (C_{mn}(r_A, r_B, \omega) - C^o_{mn}(r_A, r_B, \omega))|^2 d\omega, \tag{5.10}$$

where $w(t)$ is a time window, $*_\omega$ denotes a convolution in the frequency domain, and $C_{mn}(r_A, r_B, t)$ and C^o_{mn} are the synthetic and observed crosscorrelations, respectively. The crosscorrelations are between sensor r_A and r_B; m, n represent the components, vertical (Z) or radial (R), from each of the two sensors, respectively. One can also use the transverse component here if the noise source is thought to generate Love waves.

We use the time window in Equation 5.10 to focus on the main arrivals in the observed crosscorrelations (e.g. Maggi *et al.*, 2009; Fichtner *et al.*, 2017). We set the time window to be the signal window in our SNR measurement (Section 5.3.1). We calculate the observed crosscorrelations as described in Section 5.3.1. We calculate the synthetic crosscorrelations in the frequency domain as

$$C_{mn}(r_A, r_B, \omega) = \int_V G_{mp}(r_A, r_s, \omega) G^*_{np}(r_B, r_s, \omega) S^0_p(\omega) N(r_s) dr_s \tag{5.11}$$

where $G_{mp}(r_A, r_s, \omega)$ is the Green's function representing the mth component displacement response at location r_A due to a point force in the p direction at the source position r_s, ω is the angular frequency, and the asterisk denotes complex conjugation. We estimate the Green's functions in Section 5.3.2 and $S^0_p(\omega)$ in Section 5.3.3. In this study, we create a potential source grid that is 41 by 41 elements with a 5 m grid distance. We also assume that all sources only emit vertical-direction forces on

Earth's surface.

In order to minimize the misfit function and ensure nonnegative solutions, we apply an iterative waveform inversion methodology to update the ambient noise source distribution model (N). We minimize the waveform misfit function using a gradient-descent strategy (e.g. Ermert *et al.*, 2017; Xu *et al.*, 2019). The gradient is a sum of source sensitivity kernels over the chosen sensor pairs

$$K = \sum_{mn} \sum_{r_A r_B} \int_{\omega_1}^{\omega_2} K_{mn}(r_A, r_B, \omega) d\omega. \tag{5.12}$$

If we only use vertical data, K is a summed K_{ZZ}; if we use both C_{ZZ} and C_{RR}, $K = K_{ZZ} + K_{RR}$ among the chosen sensor pairs. We normalize K by the maximum of absolute values in K. We write the waveform source kernel for a sensor pair as

$$K_{mn}(r_A, r_B, \omega) = G_{mp}(r_A, r_s, \omega) G^*_{np}(r_B, r_s, \omega) S^0_p f, \tag{5.13}$$

where f is the adjoint source (e.g. Fichtner, 2015; Ermert *et al.*, 2017; Xu *et al.*, 2019). The adjoint source is derived from the waveform misfit function as

$$f(\omega) = \frac{1}{\pi} [w(\omega) *_\omega w(\omega) *_\omega (C_{mn}(r_A, r_B, \omega) - C^o_{mn}(r_A, r_B, \omega))]^*, \tag{5.14}$$

where $w(\omega)$ is the window function. We update the source strength distribution as

$$N_{i+1}(r_s) = N_i(r_s) e^{-\beta N_i(r_s) K}, \tag{5.15}$$

which is written this way to ensure positivity (e.g. Johansen, 1977; Xu *et al.*, 2019). We choose the step size (β) from many potential step size values (e.g. $\beta = 10^{-3}, 10^{-2}, ...10^2$).

We also apply a Gaussian smoothing filter to the updated models. We set the standard deviation of the filter to be the length of one source grid, 5 m. For each step size we generate an updated source distribution model (N_{i+1}) and compute synthetic crosscorrelations using Equation 5.11. We then calculate the corresponding misfit. Among these misfit values, we choose the step size that gives the minimum misfit; this is the common *line-search method*. If the new minimum misfit is less than 99% of the misfit in the last step, we adopt the step size and update the source model; if not, we do not update this iteration and instead expand the frequency band. We start from 4.5-6 Hz and then extend to 4.5-9 Hz.

5.4 Field data example

We process the ambient seismic recordings in the Hartoušov mofette field, Czech Republic, as a near-surface example. Mofettes, or fumaroles, are openings in Earth's surface where carbon dioxide (CO_2) flows from depths to the free surface and then escapes. This CO_2 degassing phenomenon generates high-frequency seismic waves at depth and at the free surface (e.g. Estrella *et al.*, 2016; Bussert *et al.*, 2017). The seismic waves behave like tremor (e.g. Umlauft & Korn, 2019) and thus in order to estimate the mofette distributions, we can use the source waveform inversion. We test the inversion with both synthetic and field data.

A seismic observation was conducted at the Hartoušov mofette field, Czech Republic. The seismic observations are continuous from 21 to 24 November 2016. In this paper we use a subset of the observation, a sub-array that consists of 23 three-component 4.5-Hz geophones (Figure 5.1). The recording sample rate is 250 Hz and we downsample the data to 200 Hz to speed the crosscorrelation process. We abandon one of the 23 geophones because there is too much noise at the station. Thus we

use the 22 geophones to estimate the ambient seismic source distribution. The area under the array is relatively flat. The maximum elevation difference is 1.5 m, which is negligible compared to the shortest wavelength we use in this study, about 20 m. Through the data selection (Section 5.3.1), we end up with 47 C_{ZZ} and 22 C_{RR} as the observed crosscorrelations, noting that we only use RR data that also had ZZ data to ensure we focus on the Rayleigh wave.

5.4.1 Synthetic data tests

We examine our estimation algorithm for S_p^0 and the subsequent inversion for $N(r_s)$ with synthetic data first to understand the resolution limits of the 22-station array. We also compare the synthetic waveform inversions with and without the smoothing filter because in practice one commonly smooths the model in waveform inversion results (e.g. Tape *et al.*, 2007; Groos *et al.*, 2017), and here we investigate the effectiveness of smoothing in the waveform inversion for sources. We use the same array and same available sensor pairs as in the field data (47 C_{ZZ} and 22 C_{RR}). We create a source strength distribution model with two in-array seismic sources (e.g. Figure 5.5a). We use synthetic data generated with an elastic model as the observed data and thus use elastic Rayleigh-wave Green's functions (Equation 5.1 and 5.2) in the inversion. We use the Rayleigh-wave phase velocities from the field data (Figure C.3) in the Green's functions; then use the source energy spectral density shapes (S_Z^0 and S_R^0) from the raw data (black lines in Figure 5.4) to calculate synthetic crosscorrelations (Equation 5.11) and autocorrelations (Equation 5.3). Prior to the inversion, we apply our algorithm to estimating the source energy spectral densities (Section 5.3.3). We observe that we recover the correct source energy spectral densities (red dashed lines in Figure 5.4). This observation fits our theory. Notice

the peaks in the spectra (Figure 5.4) do not affect the source inversion because the inversion already incorporates the spectra as S_Z^0 and S_R^0 in Equation 5.13.

After estimating the source energy spectral densities, we use the elastic synthetic data as the observed data and do the waveform inversion (Figure 5.5). For the elastic data, we obviously use the correct S_Z^0 and S_R^0 (red dashed line in Figure 5.4) in the waveform inversions. We observe that the $ZZ + RR$ inversion result (Figure 5.5e) is closer to the true source model than the ZZ inversion result (Figure 5.5c) if we do not use the smoothing filter. However, with smoothing, the $ZZ + RR$ gives a similar inversion result (Figure 5.5d and 5.5f) and a similar final misfit to ZZ (Table 5.1). Hence smoothing acts to suppress the improved resolution from the RR sensitivity kernels while helping to recover the shape of seismic sources within fewer iterations (Table 5.1). Therefore, we adopt the smoothing in the waveform inversion of the field data, recognizing that our results are perhaps overly smeared.

5.4.2 Source inversion results

We apply the waveform inversion to the Hartoušov observed data – 47 C_{ZZ} and 22 C_{RR} waveforms, after the preprocessing procedures (Sections 5.3.1-5.3.3). We use the estimated source energy spectral densities (black lines in Figure 5.4) in the forward model. We compare the different waveform misfits for the different inversion models in Table 5.2. For example, the waveforms from the ZZ inversion (Figure 5.6a) fit the observed C_{ZZ} well, but do not fit the observed C_{RR} as well as the $ZZ + RR$ inversion (Table 5.2 and Figure 5.7). The $ZZ + RR$ inversion model gives a similar misfit for C_{ZZ} waveforms and also a similar total misfit for C_{ZZ} and C_{RR} compared to the ZZ inversion. The ZZ inversion result (Figure 5.6b) indicates one strong and two weak (east and west) sources. However, the $ZZ + RR$ inversion only indicates one source

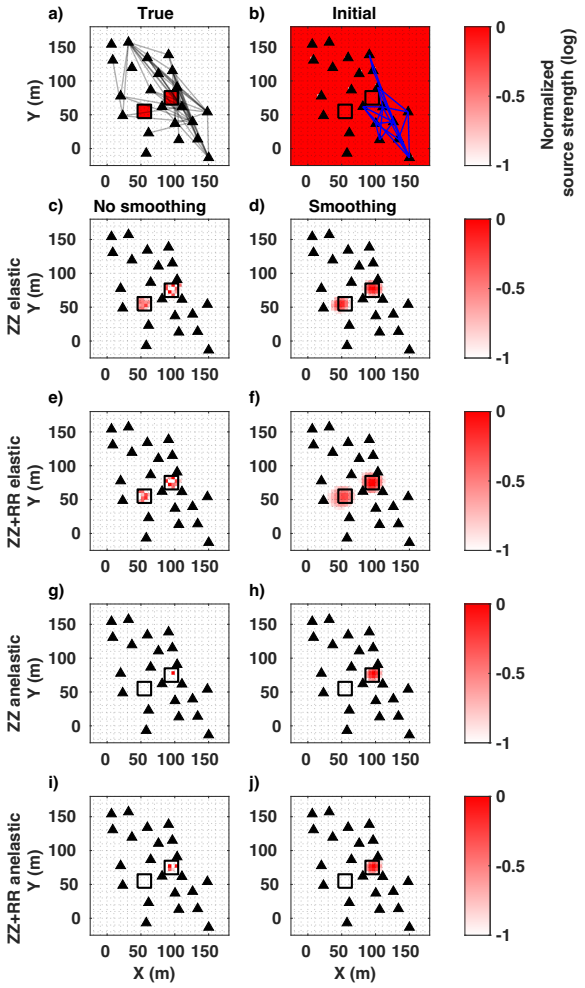

Figure 5.5: The elastic and anelastic synthetic data inversion results. a) The true source strength is zero everywhere except for the two source areas within the array. Each triangle represents a geophone. From an initial source model (b), for the elastic synthetic crosscorrelations, we invert ZZ waveforms with and without smoothing (c and d, respectively) and $ZZ+RR$ waveforms with and without smoothing (e and f, respectively). For the anelastic synthetic crosscorrelations, we invert ZZ waveforms with and without smoothing (g and h, respectively) and $ZZ + RR$ waveforms with and without smoothing (i and j, respectively). The empty squares indicate the true source areas. The gray lines in (a) indicate the 47 available C_{ZZ} sensor pairs; the blue lines in (d) indicate the 22 available C_{RR} sensor pairs that passed the data selection criteria.

Table 5.1: Final waveform inversion misfits from the ZZ/ZZ+RR inversions in the synthetic data tests. We show the final misfits in the 4.5 to 9 Hz band relative to the initial misfit (Equation 5.10). The number of iterations is provided in parenthesis next to the mistfit value. The two-source elastic examples are presented in Section 5.4.1 and the other examples are presented in Section 5.5.

Method	Elastic without smoothing	Elastic with smoothing	Anelastic without smoothing	Anelastic with smoothing
Two-source example	0.08(21)/0.10(15)	0.09(2)/0.10(4)	0.52(2)/0.43(3)	0.27(2)/0.34(2)
Out-of-array source	-	-	-	0.41 (2)/0.24(3)
Three-source example 1	-	0.13(4)/0.12(3)	-	-
Three-source example 2	-	0.24(3)/0.20(7)	-	-
Three-source example 3	-	0.08(14)/0.10(7)	-	-

in a similar location as the west weak source in the ZZ model (Figure 5.8b). Notice that the $ZZ + RR$ inversion result explains both C_{ZZ} and C_{RR} waveforms, while the ZZ model only explains the C_{ZZ} waveforms. Thus the one source estimation from the $ZZ + RR$ inversion is more reasonable than the ZZ inversion result. Moreover, based on a synthetic test in Section 5.5.1, the strong source in the ZZ result is likely due to the anelasticity of the subsurface

Table 5.2: Final waveform misfits from ZZ and $ZZ + RR$ waveform inversions on the Hartoušov crosscorrelations. We show the the final misfit in the 4.5 to 9 Hz band. Misfit values are relative to the initial misfit (Equation 5.10) in each case.

Data	Iteration	C_{ZZ}	C_{RR}	C_{ZZ} and C_{RR}
ZZ inversion	5	0.63	0.58	0.61
$ZZ + RR$ inversion	4	0.69	0.47	0.62

Besides the seismic data analysis, we use the CO_2 flux data to validate our inversion results. On top of the inversion results, we overlay the CO_2 flux map (Nickschick *et al.*, 2015) collected 3 years before the seismic data here. The strong source in the ZZ result is not close to any strong CO_2 gas areas, acknowledging that we lack complete data coverage of the gas data. However, the common source in the ZZ and $ZZ + RR$ results is near the strong gas sources to the East (i.e. fluxes>50 $g/d/m^2$), but does not perfectly coincide with a high gas-flux area measured three years prior. The location bias for the common source could be due to our simplified 1D velocity model and/or the source actually occurring at depth or moving laterally since the gas data were collected. We revisit the potential velocity model bias in Section 5.5.1, but we assume that all seismic sources are on the Earth's surface in this workflow, even though the CO_2 flux can generate seismic energy at depth (e.g. Bussert *et al.*, 2017). Both of these potentially invalid assumptions can lead to location biases. However we also note that the CO_2 data were not acquired at the same time as the seismic data, and mofettes/fumaroles are known to turn on and off through time (e.g. Nickschick *et al.*, 2015; Umlauft & Korn, 2019).

Based on the waveform misfits and the location of strong degassing, our conclusion is that the common source in the ZZ and $ZZ+RR$ inversion results is likely a seismic source (or small region of sources) active during the 2.5 hours over which the ambient seismic data were collected. The other seismic sources in the ZZ model can not explain the C_{RR} waveforms. Thus the $ZZ + RR$ inversion provides a better result than the ZZ inversion. We also note that the $ZZ + RR$ inversion required one less iteration than the ZZ inversion and from previous work (Xu *et al.*, 2019) we know that RR data have better resolution than ZZ data when the SNR of the two data

are comparable.

5.5 Discussion

It is important to estimate the uncertainty in inversion problems. Uncertainty in inversion results is due to (1) errors in data, (2) errors in the physics, and (3) insufficient sensitivity (resolution) of the inverse problem based on the spatial data sampling. We focus on the latter two here, noting that it is difficult to assess the true uncertainty in the source waveform inversion. For instance, we have incorporated smoothing, a type of regularization, into the inversion. Thus any estimated uncertainty would be for the regularized solution rather than for the true solution (e.g. Aster *et al.*, 2011). To address the issue of uncertainty one could use Monte Carlo methods (e.g. Sen & Stoffa, 1991; Tarantola, 2005) because one does not necessary need to adopt a regularization.

5.5.1 Inaccurate velocity model

We make two major assumptions in the waveform inversion method (listed in Section 5.2), and any violation of these assumptions leads to errors in the physics of the inverse problem. Here we consider the first assumption (that the subsurface structure is known) and focus on the error due to (i) an inaccurate subsurface velocity model or (ii) using an incorrect material model (e.g. elastic vs. anelastic). First, inaccurate velocity models are known to lead to artifacts and biased source location in traditional source imaging methods (e.g. Billings *et al.*, 1994; Eisner *et al.*, 2009). In full-waveform inversion, one can not resolve a source distribution accurately with an inaccurate velocity model because the two are coupled within the misfit function (e.g. Fichtner, 2015). Here we have neglected that coupling, but Xu *et al.* (2019) study

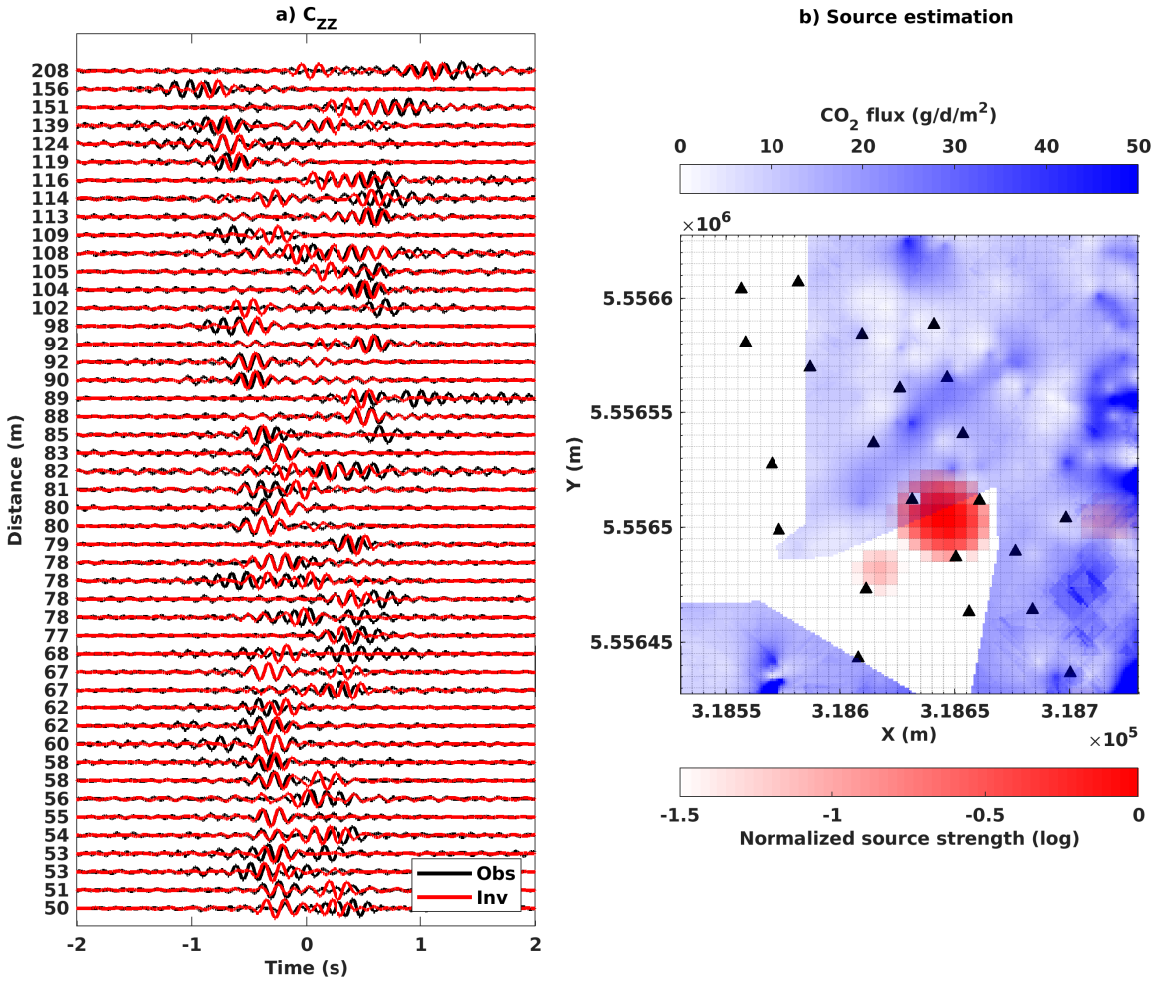

Figure 5.6: The data comparison and source distribution map from the inversion of C_{ZZ} waveforms. a) The observed and synthetic C_{ZZ} waveforms are arranged based on the interstation distance of sensor pairs. Each waveform is band-pass filtered between 4.5 and 9 Hz and then normalized by its maximum amplitude for visual comparison. b) The red area indicates the seismic source area and the red color indicates the source strength. The blue color indicates measured CO_2 gas fluxes in the unit of gram per day per meter square (Nickschick *et al.*, 2015). Black triangles are the geophones. The coordinates are in WGS84/UTM, zone 33.

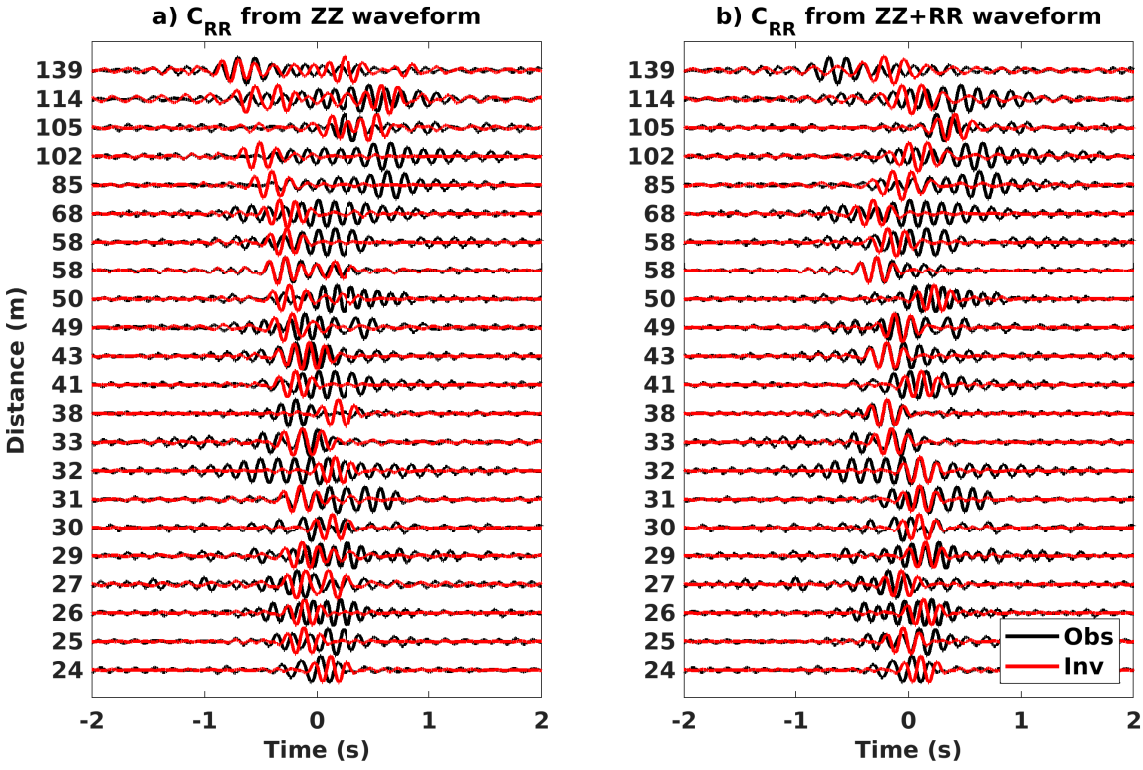

Figure 5.7: The C_{RR} waveform comparisons from the inversion of ZZ (a) and $ZZ + RR$ (b) crosscorrelations.

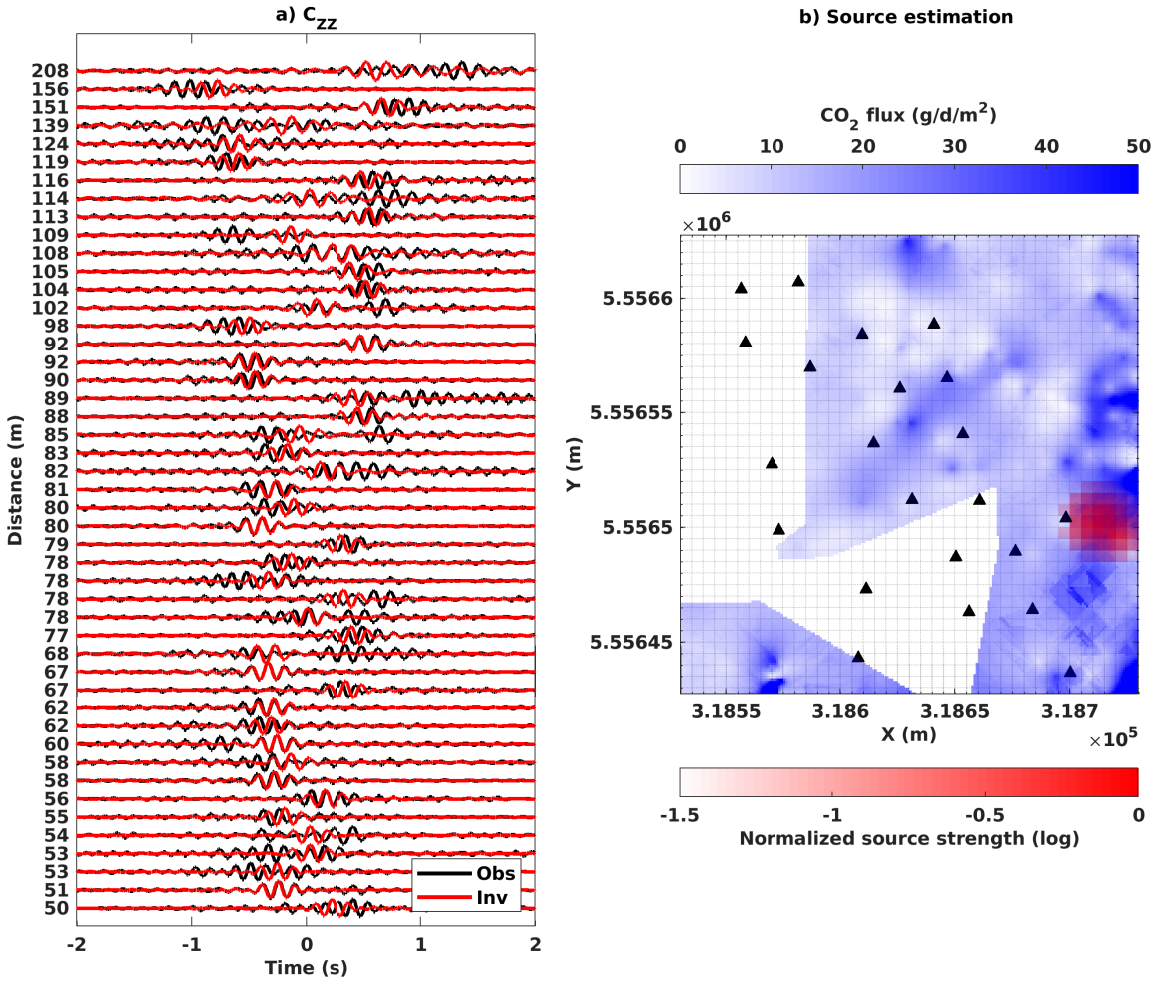

Figure 5.8: The data comparison and source distribution map from the inversion of C_{ZZ} and C_{RR} waveforms. All inversion parameters match those in Figure 5.6.

the source waveform inversion using an incorrect elastic velocity model and find that this increases the misfit and moves the estimated source location. In the field data presented here, we assume that the subsurface is laterally-homogeneous and elastic, but the real subsurface is laterally-heterogeneous and anelastic (e.g. Nickschick *et al.*, 2015).

The second violation we must consider is related to the latter, an anelastic material. We know that wave propagation through anelastic media influences the array sensitivity because, due to attenuation, some stations may not record signal from a given source. Therefore, different stations will sense different sources, potentially leading to competing source models within the inverse problem. Therefore, we study the effect of the anelasticity on the source waveform inversion here. Similar to the synthetic tests (Section 5.4.1), we generate synthetic data with an anelastic model to use as the observed data. From these data we estimate the incorrect S_Z^0 and S_R^0, and then apply the source waveform inversion using an elastic model. In doing so, we make the assumption that the observed data are elastic, directly leading to a violation of the inverse problem physics.

To generate anelastic data, we use anelastic Rayleigh-wave Green's functions:

$$G_{ZZ}^{\alpha}(r,\omega) = \sqrt{\frac{1}{8\pi\omega r/c}} e^{-i(\omega r/c+\pi/4)} e^{-\alpha r}, \tag{5.16}$$

and

$$G_{RZ}^{\alpha}(r,\omega) = \frac{H(\omega)}{V(\omega)} \sqrt{\frac{1}{8\pi\omega r/c}} e^{-i(\omega r/c-\pi/4)} e^{-\alpha r}, \tag{5.17}$$

where α is the attenuation coefficient for Rayleigh waves (e.g. Lai *et al.*, 2002; Xia *et al.*, 2002). We use $\alpha = 0.01\omega/2\pi$ here. For the source energy spectral density

estimation, our estimations of S_Z^0 and S_R^0 from the anelastic observed data autocorrelations (blue lines in Figure 5.4) are biased and should be corrected (e.g. Groos *et al.*, 2014) if possible. This bias is because our estimation procedure is based on an elastic medium and does not compensate the amplitude loss due to the anelastic attenuation, $e^{-\alpha r}$ in Equation 5.16 and 5.17. Here we do not correct this bias in order to assess the significance of this violation on the two-source example. We use the biased source energy spectral density estimates in the source waveform inversion, and observe that in all cases the misfits for the anelastic data are larger than the elastic model results (Table 5.1). The non-smoothed ZZ and $ZZ+RR$ anelastic data inversion results are similar to each other (Figure 5.5g and 5.5i), and both models only resolve one source instead of two. Thus the anelasticity can lead to missed sources, and in this case the one-source model is likely due to the inter-station correlation coverage (Figures 5.5a and 5.5b), which largely samples the one source that is resolved. Thus, in the case of anelastic data, one should use an anelastic model (e.g. Groos *et al.*, 2014, 2017).

We apply the above test to a model with one out-of-array source. This source is in a similar location as the estimated source from the field $ZZ + RR$ data (Figure 5.8b). The synthetic observed data come from the anelastic model, and we use the elastic model in the inversion. We observe that the ZZ inversion images spurious strong sources in the array and a weak source in the true source area (Figure 5.9a). In contrast, the $ZZ + RR$ inversion accurately estimates the true source location (Figure 5.9b). This observation indicates that even when the source inversion uses an elastic model, but the observed data come from an anelastic model, the multicomponent data provide a more accurate source estimation than the vertical-component data alone. Regardless of the lost resolution due to smoothing the kernels, this high-

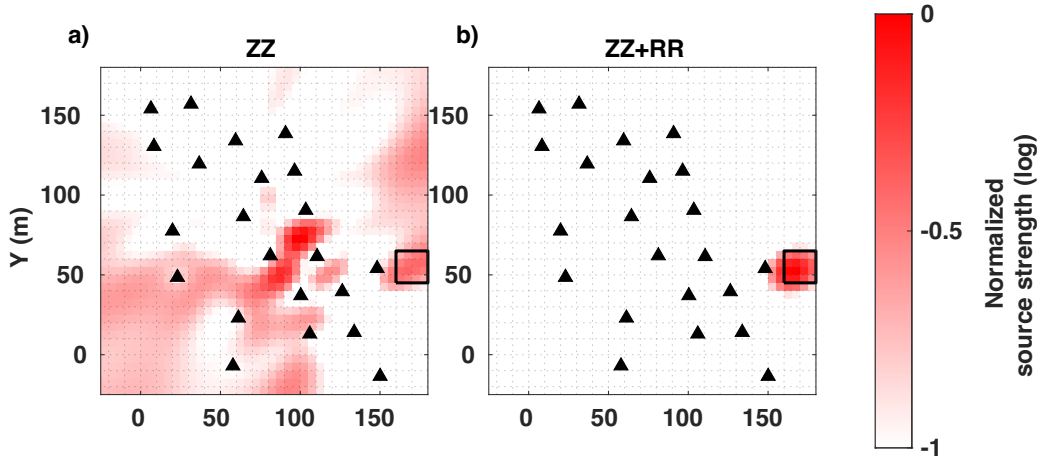

Figure 5.9: The anelastic synthetic data inversion results for one out-of-array source. The true source strength is zero everywhere except for the out-of-array source area which is indicated by the empty box. We invert ZZ and $ZZ + RR$ waveforms with smoothing (a and b, respectively). All inversion parameters match those in Figure 5.5.

lights the usefulness of incorporating the multicomponent crosscorrelations into source waveform inversion.

The last point to note related to violating the physics is that the subsurface velocity model changes when the CO_2 gas is moving through the subsurface and escaping into the atmosphere (e.g. Ikeda *et al.*, 2016). Thus it is likely necessary to jointly estimate both the source distribution and subsurface velocity models from ambient seismic noise data either iteratively or simultaneously (e.g. Sager *et al.*, 2018) to get the most accurate results. This is an area of future research and we plan to work on a joint inversion in the future.

5.5.2 Insufficient sensitivity

Besides attenuation, insufficient sensitivity in the inverse problem is due to the array geometry and the sensor pairs we choose based on the SNR of the crosscorrelations. The array geometry can lead to a null space in the inverse problem and thus there is

zero sensitivity to sources located in a particular region of the model. To determine how significant the errors are in the final results, one could do synthetic tests to characterize how the source location and strength changes with array geometry. Xu *et al.* (2019) study sources inside the array and outside of the array and find that sources outside of the array are smeared due to the lack of resolution.

To study the relationship between in- and out-of-array sources here, we complete a third synthetic elastic test. We add an out-of-array source region to our previous two-source synthetic elastic model (Figure 5.5) at three different locations. On the one hand, we observe that the waveform inversion resolves the out-of-array source, but with a reduced amplitude compared to the in-array sources (Figure 5.10), even though the true amplitudes for all the sources are the same. On the other hand, the waveform inversion may resolve out-of-array sources in biased locations when only the ZZ waveforms are used (Figure 5.10e). This is in contrast to the $ZZ + RR$ inversion, which resolves the sources more accurately than the ZZ inversion (Figure 5.10f) in this numerical experiment. Thus, although we have shown that ZZ and $ZZ+RR$ inversion result in similar models and misfits after applying regularization (i.e. smoothing), we recommend using all possible data in order to image sources as accurately as possible. We note that we have not tried more than three sources in our testing up to now.

5.6 Conclusion

We present a complete workflow to estimate the seismic source distribution from ambient seismic noise data. In the workflow, we propose a SNR measurement and apply a SNR criteria to select high-quality seismic crosscorrelations. We determine that it is important to select time windows that contribute to the overall SNR of the array, and to exclude correlated noise sources from the crosscorrelations. Under the

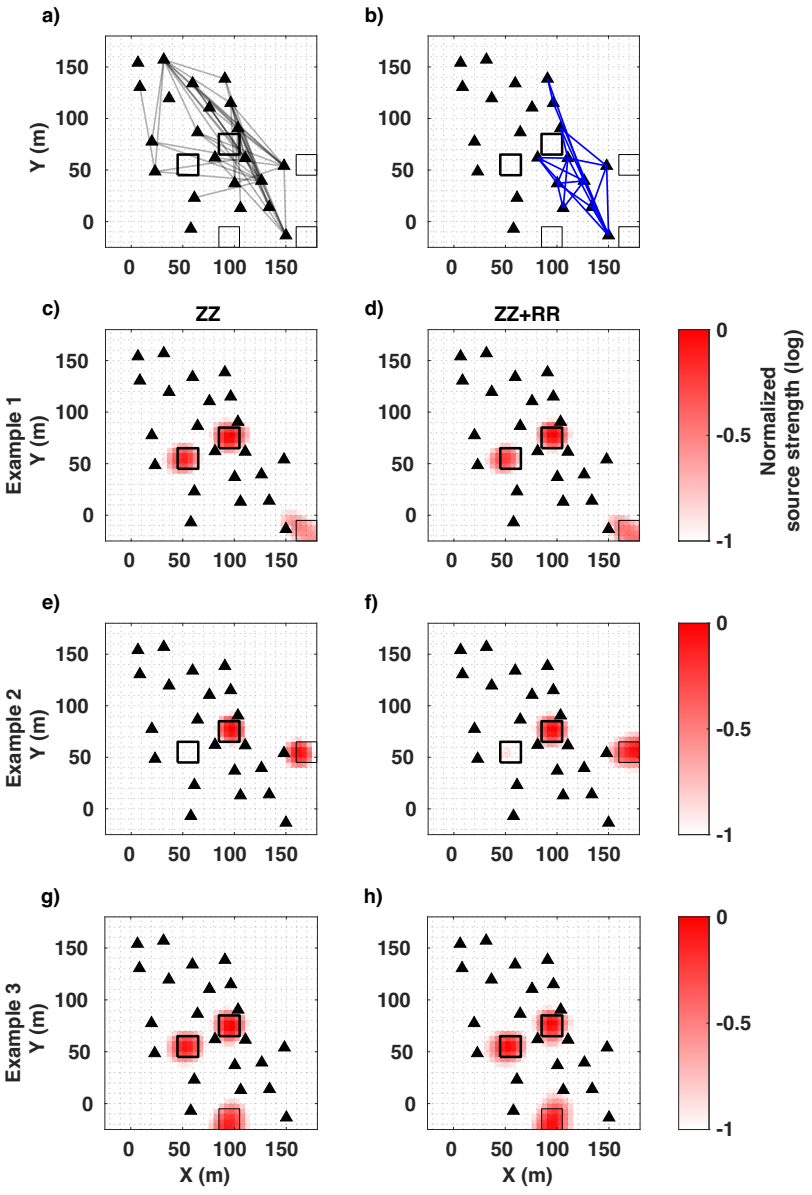

Figure 5.10: The three out-of-array source inversion results. The true source strength is zero everywhere except for the two fixed sources within the array and the one moving source outside of the array. The sources are represented by empty black squares. The initial inversion model is that in Figure 5.5b. For the elastic model crosscorrelations, we invert the ZZ waveforms (c,e,g) and $ZZ+RR$ waveforms (d,f,h). We use the same sensor pairs as in Figure 5.5: 47 C_{ZZ} sensor pairs (gray lines in a) and 22 C_{RR} sensor pairs (blue lines in b).

assumption that the subsurface is elastic and laterally homogeneous, we estimate the Green's functions and develop a novel algorithm to retrieve the source energy spectral density. Finally, we apply the waveform inversion to the highest quality crosscorrelations of field data and synthetic data sets using the same receiver geometries. We determine that $ZZ + RR$ better constrains the seismic source distribution than ZZ in elastic medium, and for anelastic data both $ZZ + RR$ and ZZ fail to recognize all seismic sources. The field data inversion results indicate a strong seismic source near the strong CO_2 gas flux area. The workflow presented is applicable for both vertical and multicomponent data, and also different scale field data.

CHAPTER 6:
ESTIMATION OF PRIMARY MICROSEISM SOURCE DISTRIBUTIONS AROUND ANTARCTICA

6.1 Summary

Primary microseism sources around Antarctica are important for ambient noise tomography studies and ocean studies in Antarctica. We apply the source waveform inversion method to the seismic recordings in Antarctica during February 2010 and estimate the primary microseism source distribution. Our source estimation provides good waveform fits to vertical-component crosscorrelations with interstation distances less than 500 km. The main part of the estimated sources are distributed outside of the sea ice surrounding Antarctica. Thus in terms of the spatial relationship with sea ice, our source estimation fits the blocking effect of sea ice on primary microseism source generations. Our research provides a new tool for studying and monitoring the primary microseism sources in Antarctica.

6.2 Introduction

Microseisms are low-frequency (<0.12 Hz) ambient seismic waves and one commonly uses the microseisms to image the Earth's crust with the ambient seismic tomography

(ANT) method (e.g. Shapiro *et al.*, 2005). One type of microseism is the primary microseism (PM), which is generated by the interaction between ocean gravity waves and the seafloor (Hasselmann, 1963). The PM ranges in frequency from about 0.04 Hz to 0.09 Hz and thus is an important signal source for ANT in investigating Earth's upper to middle crust, e.g. volcano magma chambers (e.g. Stankiewicz *et al.*, 2010) and fault systems (e.g. Vassallo *et al.*, 2016). As an improved geological understanding of Antarctica becomes important, the ANT method has been recently applied to PM data in Antarctica (e.g. An *et al.*, 2015; Shen *et al.*, 2018).

Seismic source distributions are important in the ANT method. The ANT method assumes that seismic sources are isotropically distributed in all directions around two sensors. Under this assumption, a key step in ANT is that one recovers Green's functions through seismic interferometry (e.g. Snieder, 2004; Wapenaar & Fokkema, 2006). However, this assumption is rarely met in practice (e.g. Stehly *et al.*, 2006), and thus the recovered Green's functions are biased (e.g. Yang & Ritzwoller, 2008). Many methods have been proposed to correct the bias based on seismic source distributions (e.g. Yao & Van Der Hilst, 2009; Nakata *et al.*, 2015). Therefore, in order to correct the ANT results in Antarctica, one needs the PM source distribution around Antarctica.

Microseisms are still under investigation today. Although Hasselmann (1963) theoretically explained the source mechanism of the PM, there are still many questions, e.g. the PM source distribution (locations and strengths). The beamforming method (e.g. Rost & Thomas, 2002), an array-based method for estimating seismic source direction, has been applied to locating PM sources (e.g. Cessaro, 1994; Juretzek & Hadziioannou, 2016). However, this method does not provide physical source strengths. In locating sources, this method requires at least two separate arrays

while the two arrays may be dominated by different PM sources (e.g. Gualtieri *et al.*, 2019). Thus, in this case, the beamforming method cannot even provide accurate PM source locations. One can also simulate the PM source distribution by using data of ocean gravity waves (e.g. Ardhuin *et al.*, 2015). However, the ocean data are poorly sampled in space around Antarctica and limit the accuracy of the simulation. Sea ice in this area is common, and can affect ocean gravity waves and also PM sources (e.g. Ardhuin *et al.*, 2011a). Therefore we propose another way to estimate the PM source distribution by applying full waveform inversion to the seismic recordings in Antarctica.

We apply the workflow described in Chapter 5 to process the PM data in Antarctica. We adjust the workflow based on the field scale and estimate the PM source distribution in February 2010. We use a sea ice map from the same time period to support our source estimation results.

6.3 Preprocessing

We process the seismic recordings and calculate crosscorrelations, as well as model the Green's functions and estimate the PM source energy spectral density in Antarctica. After these steps, we conduct the source waveform inversion.

6.3.1 Data selection

We process the raw seismic recordings to reduce uncorrelated and correlated noises. Stacking can suppress uncorrelated noise (e.g. Bensen *et al.*, 2007), but amplify correlated noise (e.g. Shapiro *et al.*, 2006). Thus we use the stacking in processing and meanwhile need to suppress or even remove the correlated noise, such as earthquakes. We use the seismic recordings in February 2010 and then remove the instrument re-

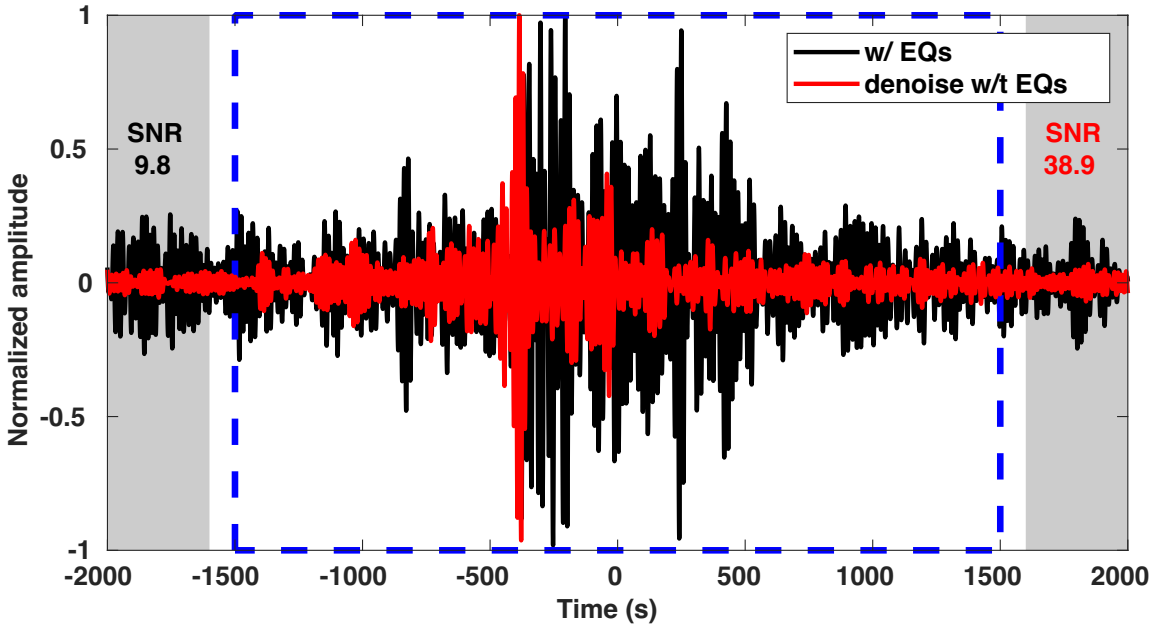

Figure 6.1: An example of the SNR changing with and without the date selection. The blue dashed box indicates the signal window (-1500-1500 s). The two gray areas indicate the two noise windows (-2000-1600 s and 1600-2000 s). SNR is defined as the ratio of the peak in the signal window and the RMS in the two noise windows. We combine the recordings in the two noise windows and then calculate the RMS from the combined recordings. The black (left) and red (right) numbers in the gray areas indicate the SNR for the two waveforms, respectively. The waveforms are band-pass filtered between 0.04-0.085 Hz.

sponse at each station. We cut the recordings into 4 h sections; then remove the mean and linear trend in each section. We then check earthquake catalogs for the month and remove the sections where earthquake occur, as well as the following sections. We also dampen events (e.g. earthquakes and spikes) with a denoising code based on the wavelet transform (Mousavi *et al.*, 2016). We observe that the signal-to-noise ratios (SNR) of crosscorrelations improve after removing the correlated noise (Figure 6.1).

We also winnow stations based on autocorrelations. We calculate the autocorrelation for each station by following the same processing above and plot all the

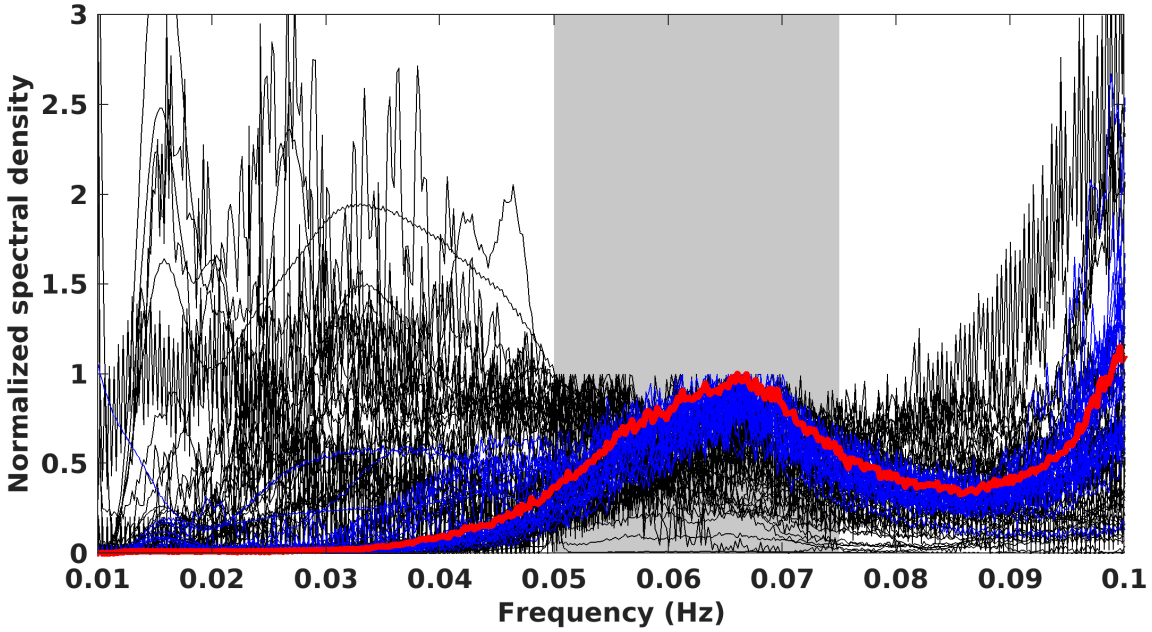

Figure 6.2: The autocorrelations of 81 available stations in the frequency domain (black lines). We estimate the median at each frequency (red line). We choose the autocorrelations which are similar to the red line with at least 0.8 crosscorrelation coefficient (blue lines).

autocorrelations in the frequency domain (Figure 6.2). We observe that the autocorrelations of some stations are noisy, which can be due to site effects as these stations may be on sediments or even ice. Thus we remove these stations from the inversion. We calculate the median at each frequency (the red line in Figure 6.2) and find the common microseism energy spectral density shape. We then choose the stations whose autocorrelations are similar to this shape with at least a 0.8 crosscorrelation coefficient between 0.05 and 0.08 Hz.

6.3.2 Green's function modeling and source energy spectral density estimation

We use the AK135 1D Earth model (Kennett *et al.*, 1995) and Instaseis (van Driel *et al.*, 2015) to model the Green's functions between all the potential sources and stations. In calculating the Green's functions, we do not consider the topography of Earth's surface.

We use the source energy spectral density shape (the red line in Figure 6.3.1) in the inversion.

6.4 Estimation of the primary microseism source distribution

We are ready to conduct the source waveform inversion. We have 81 available stations in February 2010 (Figure 6.3). After the data selection (Section 6.3.1), 26 stations and 85 high-SNR (SNR>15) observed ZZ crosscorrelations remain. We set potential seismic sources at underwater areas around Antarctica because the PM is generated by interactions between sea currents and seafloors (Hasselmann, 1963). Each two adjacent potential sources are apart by about 144 km in distance. We assume that the PM sources are all point vertical forces (e.g. Gualtieri *et al.*, 2019), and consider that the Ross ice shelf precludes microseism generation (Figure 6.3). We apply the source waveform inversion algorithm (e.g. Xu *et al.*, 2019) to the observed crosscorrelations. In the inversion, we use a gradient-decent algorithm (e.g. Ermert *et al.*, 2017) and extend the frequency band, from 0.05-0.055 Hz to 0.05-0.065 Hz and 0.05-0.075 Hz. We also smooth source models in the inversions with a 2D Gaussian smoother (3-source-point standard deviation along same latitudes and 1-source-point standard

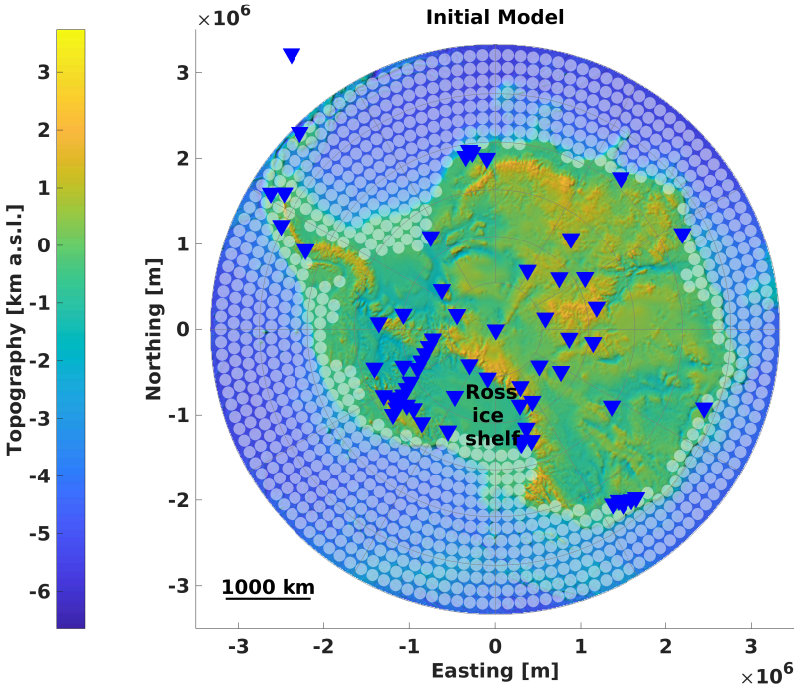

Figure 6.3: Initial 81 stations (blue triangles) and 955 potential sources. Each transparent disk represents a potential PM source. We plot the stations, topography and sources using the Antarctica mapping tool (Greene *et al.*, 2017). We will use the same tool in the following figures.

deviation along same longitudes).

6.4.1 Synthetic test

We validate our inversion algorithm with synthetic data first. We create a source strength distribution with one source in the Weddell sea (Figure 6.4) and then generate synthetic crosscorrelations using Equation 5.11. We use the same Green's functions and source energy spectral density shape (Section 6.3) in the forward modelling and also in the source inversion. We use the synthetic data as the observed data and then conduct the waveform inversion (Figure 6.5). We observe that the inversion result is close to the true source model, but does not quite have the same shape, and most of the estimated source strengths are lower compared to the true strengths.

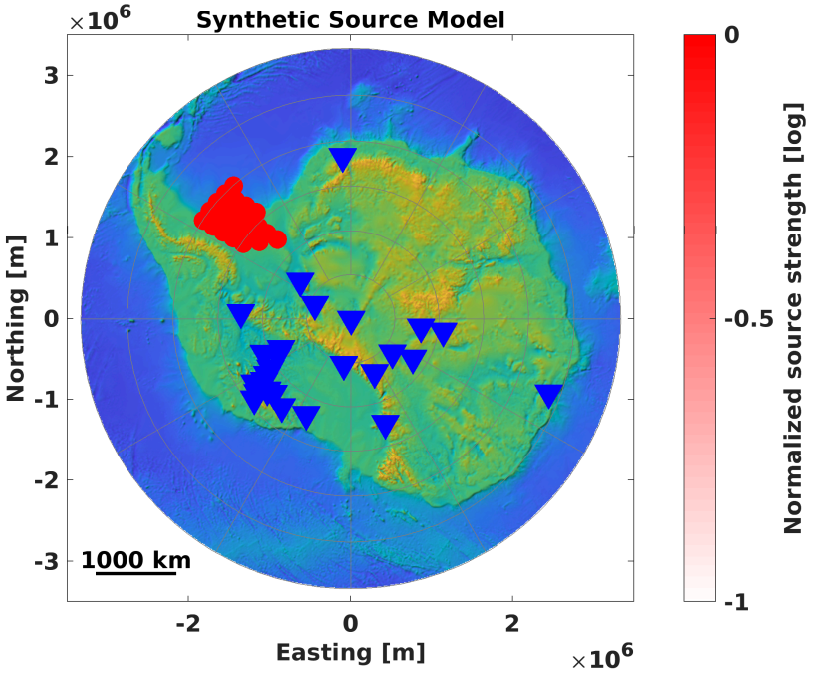

Figure 6.4: The true source strength distribution in the synthetic test. The source strengths are zero everywhere except the red area. The blue triangles represent the 26 stations which pass the data selection (Section 6.3.1). The green and yellow background represent the bed topography of Antarctica.

These discrepancies are because the source inversion cannot fully constrain out-of-array sources (e.g. Xu *et al.*, 2019).

6.4.2 Source inversion result

We apply the source waveform inversion to the real observed data, 85 ZZ crosscorrelations. Our inversion result indicates that the source distribution is not isotropic. The synthetic crosscorrelations from the inverse model fit the observed crosscorrelations well at short distance station pairs (<500 km), but arrive earlier at long distance pairs (>700 km). This arrival time difference can be because our velocity model, AK135, is not accurate for Antarctica. Despite of the arrival time difference, the main wave-

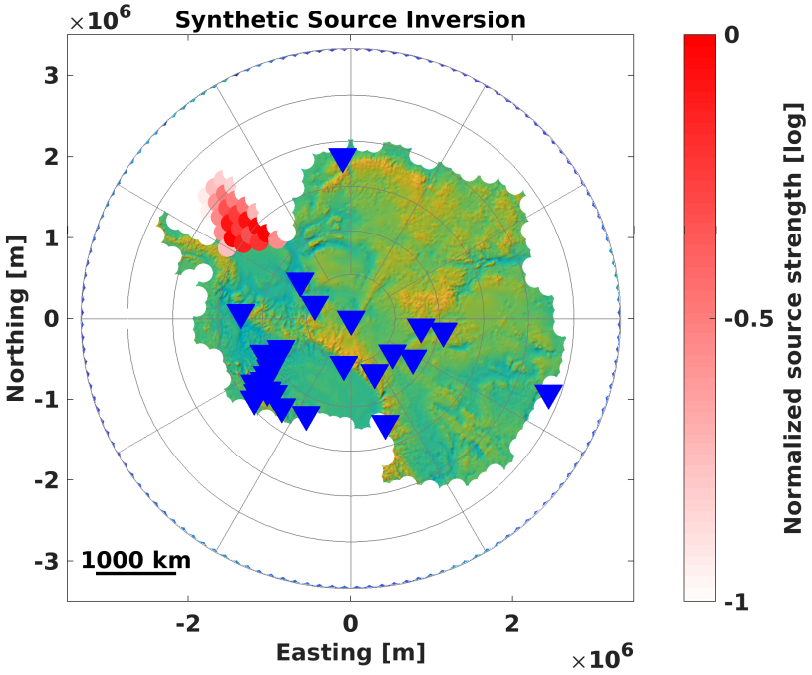

Figure 6.5: The red area is the source inversion result from the synthetic test.

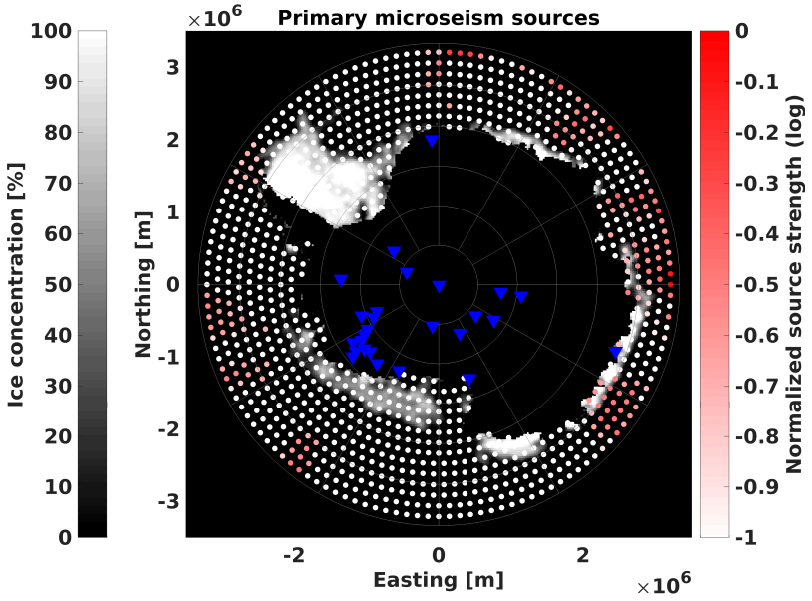

Figure 6.6: The estimation of PM source distributions in February 2010. The red dots represent the estimated PM sources. The white polygons represent sea ices. The sea ice data is acquired on February 1st 2010 (Lavergne *et al.*, 2019).

forms in the synthetic data are in the same causal branches as the observed data. Thus the source directions in our source estimation are correct.

Besides the waveform fitting, we validate our source estimation using sea ice concentration data. Sea ice can block and reflect surface gravity waves (e.g. Ardhuin *et al.*, 2011a), and thus produce PM sources in the direction where the surface gravity waves come (e.g. Ardhuin *et al.*, 2011b). Most of our estimated sources are distributed outside of the sea ice in Antarctica (Figure 6.6). Therefore, in terms of the spatial relationship with the sea ices, our source estimation fits the theory for PM sources.

6.5 Conclusion

We apply our source inversion workflow to the vertical-component seismic recordings in Antarctica during February 2010 and estimate the primary microseism source dis-

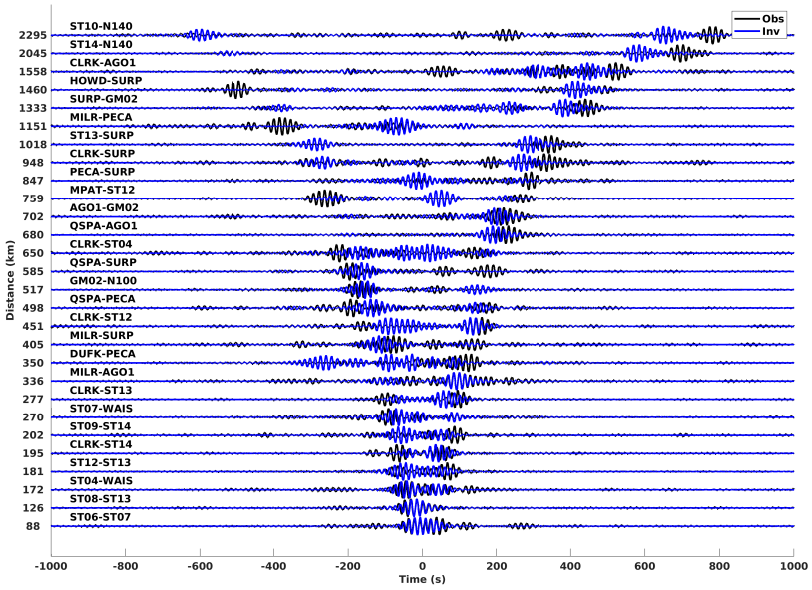

Figure 6.7: The waveform fitting from the estimated source distribution (Figure 6.6).

tribution. We select observed crosscorrelations based on signal-to-noise ratios and station site effects. We use the AK135 velocity model to calculate Green's functions. The waveform inversion provides an anisotropic source distribution. The synthetic waveforms from the estimation fit the observed crosscorrelations well at short interstation-distance (<500 km) station pairs, but not at long distance (>700 km) pairs. Our source estimation also fits the theory of primary microseism generation in terms of the spatial relationship with sea ice. Our source estimation provides a potential tool to monitor primary microseism source changes with time.

CHAPTER 7:
MONTE CARLO SIMULATIONS OF MULTIPLY SCATTERED BODY AND RAYLEIGH WAVES IN ELASTIC MEDIA

7.1 Summary

Time-lapse seismic monitoring exploits the sensitivity of coda waves to small changes in the subsurface and images the temporal and spatial evolution of seismic properties (e.g. density). This imaging method is complicated because the coda waves include multiply-scattered body and surface waves. The complication arises because these two types of waves possess different spatial sensitivities and can interact with each other via scattering. As a consequence of the latter, the energy ratio between the two types of waves evolves with time in the coda. Thus the estimation of this energy ratio is critical to obtain accurate monitoring results; however, the spatio-temporal evolution of energy partitioning in elastic media is not yet fully understood. In practice, one has to fix the energy ratio or even ignore the contributions of either surface or body waves. Based on scattering theory, we propose a Monte Carlo method to predict the energy partitioning between multiply-scattered body and Rayleigh waves as a function of time and depth in an elastic half-space. In the simulations, we use the

single scattering conversion rates from body to Rayleigh waves (and vice-versa), which rely on the depth-dependent eigenfunctions of the Rayleigh waves. We incorporate the elastic Rayleigh-wave eigenfunctions into our research. This research is a first step towards a complete modeling of coupled body- and Rayleigh-wave multiple scattering in elastic media.

7.2 Introduction

Coda waves are arrivals after direct waves in seismic recordings or seismic crosscorrelations. One commonly uses coda waves to monitor the subsurface. In the coda wave interferometry (CWI) monitoring method, one compares the coda waves in two event recordings where the two events share similar source locations (e.g. Snieder, 2006), and estimate differences in the coda-wave arrival times (e.g. Snieder *et al.*, 2002) or waveforms (e.g. Larose *et al.*, 2010). One can map these differences to small changes of seismic properties (e.g. density) in the subsurface (e.g. Pacheco & Snieder, 2005). This monitoring method has been applied to repeated event data in nature (e.g. Grêt *et al.*, 2005) and in the lab (e.g. Larose *et al.*, 2010); it is also commonly applied to the coda waves in seismic crosscorrelations (e.g. Sens-Schönfelder & Wegler, 2006; Brenguier *et al.*, 2007, 2008).

One actually utilizes multiply scattered waves in the coda waves when using the CWI monitoring method. *Multiply scattered* implies that these waves have scattered many times in the subsurface while propagating from a (virtual) source to a receiver. The multiply scattered waves propagate along longer paths in the changed subsurface than the direct waves, and thus are more sensitive to subsurface changes. Both body and surface waves exist during the scattering process. The two types of waves convert to one another via scattering and possess different spatial sensitivities to

the subsurface changes (e.g. Maeda *et al.*, 2008). Thus the energy ratio between the two types of waves evolves with time and one needs to have an estimate of the ratio for accurate monitoring. However, the evolution of the energy ratio is not fully understood yet. In seismic monitoring studies, one assumes that the coda waves consist of either multiply-scattered body waves (e.g. Sens-Schönfelder & Wegler, 2006) or multiply-scattered surface waves (e.g. Mainsant *et al.*, 2012; Obermann *et al.*, 2015), where neither assumption is actually valid. One can also assume an energy ratio, but still needs to know how the ratio evolves with time (e.g. Obermann *et al.*, 2019).

There are few studies about the multiply-scatted body and surface waves and how they interact. Zeng (2006) studies the energy ratio, but unphysically simplify the scattering process between body and surface waves. Maeda *et al.* (2008) describe the scattering process in detail, but ignored the depth-dependent sensitivity of Rayleigh waves in deriving the scattering cross sections. Margerin *et al.* (2019) consider both the scattering process and the Rayleigh-wave sensitivities, and present the energy ratio temporal evolution using a Monte Carlo simulation method. However, the simulation is for scalar wavefields, instead of elastic wavefields. There is yet another method to calculate the evolution with numerical modelling methods (e.g. Obermann *et al.*, 2013, 2016), but that method requires significant computation costs compared to the Monte Carlo simulation method.

We present the evolution of energy partitioning between multiply-scatted body and surface waves in elastic media. We focus on perturbations of the *Lamé* parameter (λ), where these perturbations ($\delta\lambda$) act as scatters in the media. Thus we only have P-to-P (PP), P-to-Rayleigh (PR), Rayleigh-to-P (RP) and Rayleigh-to-Rayleigh

(RR) scatterings. We use the Monte Carlo simulation method to model the multiple scattering processing (e.g. Hoshiba, 1991; Margerin *et al.*, 2000). We conduct the simulation without a P-S coupling at the free surface, and then estimate the temporal energy ratio between multiply-scattered Rayleigh and body waves. The temporal energy ratio eventually reaches a steady value, an equipartition ratio. We verify the simulation by comparing the equipartition ratio to a theoretical prediction. We also conduct the simulation with the P-S coupling at free surface.

7.3 Scattering process

The Monte Carlo simulation of multiple scattering requires estimates of the single scattering cross sections and multiply scattering mean free path/time. The intensity of waves is the basis for the estimates. Thus we introduce the intensity, the cross sections and then calculate the mean free path/time. All the equations in this study are in the frequency domain.

7.3.1 Wave intensity

The intensity of an incident body wave (e.g. P wave) in a media is written as

$$I_P(\omega) = \rho_0 \alpha_0 \omega^2 A_{0P}^2, \tag{7.1}$$

where ρ_0 is the media density, α_0 is the P-wave velocity, ω is the angular frequency and A_{0P} is the P-wave amplitude (e.g. Aki & Richards, 2002). The intensity for a Rayleigh wave is different from a body wave, because a Rayleigh wave possess displacements in the whole depths while a body wave only possess displacement at one depth. Thus the intensity of an incident Rayleigh waves is defined with a depth integral as (e.g.

Aki & Richards, 2002)

$$I_R(\omega) = \rho_0 U_R \omega^2 \int_0^\infty A_{0R}^2 [r_1^2(z) + r_2^2(z)] dz, \tag{7.2}$$

where U_R is the Rayleigh-wave group velocity at the frequency ω, A_{0R} is the Rayleigh-wave displacement at the surface ($z = 0$). r_1 and r_2 are the horizontal and vertical displacement eigenfunctions of the Rayleigh wave (Appendix D.1). The eigenfunctions vary with the depth, also the frequency. Notice that the unit of I_P and I_R is $J/(m^2 s)$ and $J/(ms)$, respectively. The unit difference is due to the depth integral.

7.3.2 Single scattering

We need to calculate the cross sections for four types of single scattering: PP, PR, RP and RR. Calculation of each cross section requires the corresponding scattering amplitude (e.g. Margerin *et al.*, 2000). Maeda *et al.* (2008) derive the scattering amplitudes, and we use the result here. For example, PR scattering indicates a scattered Rayleigh wave from an incident P wave. The amplitude of a scattered Rayleigh wave due to a perturbation of the *Lamé* parameter ($\delta\lambda$) is written as

$$A_\lambda^{PR}(z_s, \omega) = -A_{0P} \frac{\omega^2 p_i(z, \omega) \alpha_0}{4 \int (r_1^2 + r_2^2) dz U_R^2 c_R} \left(1 - \frac{2\beta_0^2}{\alpha_0^2}\right) \sqrt{\frac{2}{\pi k_R \Delta}} \int_V [r_1(z_s, \omega) + \frac{1}{k_R} \frac{dr_2}{dz_s}] \frac{\delta\lambda}{\lambda_0} dr_s, \tag{7.3}$$

where β_0 is the S-wave velocity, c_R is the Rayleigh-wave phase velocity at frequency ω and $k_R = \omega/c$ (Maeda *et al.*, 2008). Δ is the scattered Rayleigh-wave travel distance along Earth's surface. p_i is the Rayleigh-wave eigenfunction, r_1 or r_2 (Section 7.3.1). z_s is the depth of the scatter, $\delta\lambda$. λ_0 is the unperturbed *Lamé* parameter of the media. The volume integral, $\int_V [r_1 + \frac{1}{k_R} \frac{dr_2}{dz_s}] \frac{\delta\lambda}{\lambda_0} dr_s$, is an integral on the scatter body. We

ignore the size of the scatter, and thus the volume integral becomes $[r_1 + \frac{1}{k_R}\frac{dr_2}{dz_s}]\frac{\int \delta\lambda dr_s}{\lambda_0}$. Therefore we are working in the regime of so-called Rayleigh scattering (e.g. Wu & Aki, 1985), where scatterer shapes are negligible for low-frequency waves.

We then calculate the intensity of scattered Rayleigh waves in all directions using a cylinder surface integral:

$$I_\lambda^{PR}(z_s,\omega) = \rho_0 U_R \omega^2 \int_S (A_\lambda^{PR})^2 \Delta d\xi dz, \tag{7.4}$$

$$= \rho_0 U_R \omega^2 2\pi\Delta \int_0^\infty (A_\lambda^{PR})^2 dz, \tag{7.5}$$

$$= \rho_0 \omega^5 \frac{(\alpha_0^2 - 2\beta_0^2)^2 A_{0P}^2}{4\int (r_1^2 + r_2^2) dz U_R^3 \alpha_0^2 c_R} [r_1(z_s) + \frac{1}{k_R}\frac{\partial r_2}{\partial z_s}]^2 \left(\frac{\int \delta\lambda dr_s}{\lambda_0}\right)^2, \tag{7.6}$$

where ξ is the scattering azimuth and z is the depth. The scattering cross section is defined as the ratio of intensities between all the scattered waves and the incident wave. Thus we write the PR cross section as

$$\sigma_\lambda^{PR}(z_s,\omega) = \frac{I_\lambda^{PR}}{I_P} = \frac{k_P^3(\alpha_0^2 - 2\beta_0^2)^2}{4U_R^3 c_R \int (r_1^2 + r_2^2) dz} [r_1(z_s) + \frac{1}{k_R}\frac{\partial r_2}{\partial z_s}]^2 \left(\frac{\int_V \delta\lambda dr_s}{\lambda_0}\right)^2, \tag{7.7}$$

where $k_p = \omega/\alpha_0$. The unit for this cross section is m^2. Notice this cross section depends on the scatterer depth (z_s) and is linked to the depth-dependent eigenfunctions of the scattered Rayleigh waves. Following the same logic, we can write the PP cross section as:

$$\sigma_\lambda^{PP}(\omega) = \frac{k_P^4}{4\pi} \left(\frac{\alpha_0^2 - 2\beta_0^2}{\alpha_0^2}\right)^2 \left(\frac{\int_V \delta\lambda dr_s}{\lambda_0}\right)^2. \tag{7.8}$$

Notice that, different from σ_λ^{PR}, σ_λ^{PP} is independent of the scatterer depth.

We then calculate the cross sections for incident Rayleigh waves. Following the same steps above, we can write the RP cross section as

$$\sigma_\lambda^{RP}(z_s,\omega) = \frac{I_\lambda^{RP}}{I_R} = \frac{k_P^4(\alpha_0^2-2\beta_0^2)^2}{4\pi c_R^2 U_R \alpha_0 \int(r_1^2+r_2^2)dz}[r_1(z_s)+\frac{1}{k_R}\frac{\partial r_2}{\partial z_s}]^2\left(\frac{\int_V \delta\lambda dr_s}{\lambda_0}\right)^2. \quad (7.9)$$

Notice the unit for σ_λ^{RP} is m, instead of m^2 like σ_λ^{PR} or σ_λ^{PP}. This is because of the unit difference between I_R and I_P (Section 7.3.1). The incident Rayleigh wave possess displacements and the scatters exist randomly both at all depths; thus the RP scattering can also happen where the eigenfunctions are non-zero. Thus we need to consider all possible scatterings and integrate σ_λ^{RP} over depth to achieve the average cross section:

$$\overline{\sigma}_\lambda^{RP}(\omega) = \int_0^\infty \sigma_\lambda^{RP} dz_s \quad (7.10)$$

$$= \frac{k_P^4(\alpha_0^2-2\beta_0^2)^2}{4\pi c_R^2 U_R \alpha_0 \int(r_1^2+r_2^2)dz}\int[r_1(z_s)+\frac{1}{k_R}\frac{\partial r_2}{\partial z_s}]^2 dz_s\left(\frac{\int_V \delta\lambda dr_s}{\lambda_0}\right)^2, \quad (7.11)$$

where the cross section unit is m^2. Following the same logic, we achieve $\overline{\sigma}_\lambda^{RR}$ as

$$\overline{\sigma}_\lambda^{RR}(\omega) = \frac{\omega^3(\alpha_0^2-2\beta_0^2)^2}{4U_R^2 c_R^5[\int(r_1^2+r_2^2)dz]^2}\int[r_1(z_s)+\frac{1}{k_R}\frac{\partial r_2}{\partial z_s}]^4 dz_s\left(\frac{\int_V \delta\lambda dr_s}{\lambda_0}\right)^2. \quad (7.12)$$

7.3.3 Multiple scattering

Multiple scattering means that single scattering happens many times as a wave propagates from a (virtual) source to a receiver, and thus single scattering is the basis for multiple scattering. We link multiple scattering to single scattering using the independent scattering approximation (e.g. Lagendijk & Van Tiggelen, 1996). In the

approximation, we define a volume density of point scatters (n) and write the mean free path (l^w) for one incident wave as

$$l^w = \frac{1}{n\sigma}, \tag{7.13}$$

where σ is the sum of all the single-scattering cross sections for the incident wave (e.g. Margerin *et al.*, 2000), such as $\sigma^P(z,\omega) = \sigma_\lambda^{PR}(z,\omega) + \sigma_\lambda^{PP}(\omega)$ in this study. The mean free path indicates the average distance between two scatters (e.g. Hoshiba, 1991) and has the unit of m. The corresponding mean free time (τ^w) is defined as

$$\tau^w = \frac{l^w}{v} = \frac{1}{n\sigma v}, \tag{7.14}$$

where v is the incident wave velocity (e.g. Margerin *et al.*, 2000). The mean free time indicates the average time interval between scattering.

7.3.4 Theoretical equipartition value

We calculate the theoretical equipartition ratio between two types of multiply-scattered waves. For example, one can calculate the ratio between multiply-scattered P and S waves based on $P-to-S$ and $S-to-P$ cross sections (e.g. Snieder, 2002). Following Margerin *et al.* (2019) and ignoring the P-S coupling at free surface, we write the equipartition energy ratio between multiply-scattered P and Rayleigh waves as

$$\frac{\bar{\bar{E}}_R}{\bar{E}_P} = \int \frac{\tau_\lambda^{RP}}{\tau_\lambda^{PR}} dz = \frac{\pi\alpha_0^3}{\omega c_R^2}, \tag{7.15}$$

where $\bar{\bar{E}}_R$ is the total Rayleigh-wave energy over the whole media, and $\bar{E}_P$ is an integral of P-wave energy over a constant-depth plane and is the same in all depths

in the equipartition status (Margerin *et al.*, 2019). We write U as c_R because the two are equal in a homogeneous isotropic elastic media.

7.4 Monte Carlo simulation

We simulate multiple scattering with a Monte Carlo method. The Monte Carlo simulation method has been applied to multiply scattered acoustic/elastic body waves (e.g. Hoshiba, 1991; Margerin *et al.*, 2000). We use the method to simulate multiply-scatted P and Rayleigh waves in a homogeneous isotropic elastic media. The underlying idea for the Monte Carlo simulation is that we simulate a wave propagating like a particle N times (Algorithm 2). We generate a wave each time, and the wave can be either a P or a Rayleigh wave. We then let the wave propagate during a random free time τ, where τ is the time before the next scattering happens. We calculate τ as $\tau = -\tau^w ln(n)$ where n is a random number with a uniform possibility distribution from 0 to 1 (e.g. Hoshiba, 1991). If τ^w is constant in the whole media, we only need one τ before the next scattering. However, the P-wave mean free time (τ^P) varies with depth, because σ^{PR} depends on depth (z). Thus we need to modify the mean free time and free time for P waves in the propagation because $-\tau^w ln(n)$ changes. This makes the simulation difficult to be conducted because we need to always track the P-wave depth and modify the free time when the P waves propagate to different depths. To address this difficulty, we adopt a trick called delta collisions (Lux & Koblinger, 1991). The idea of this method is to create an effective and constant τ^P. The details of this method are in Algorithm 3. This difficulty does not exist for τ^R because both $\overline{\sigma}_\lambda^{RP}$ and $\overline{\sigma}_\lambda^{RR}$ are independent of depth. After τ, the wave encounters a scatterer, and scattering occurs. We generate a random value from 0 to 1 to determine if the wave converts to the other wave type (Algorithm 3 and 4). Notice that

for incident Rayleigh waves, if the RP conversion happens, we place the scattered P wave at a depth based on the probability of σ_λ^{RP} at all depths (Appendix D.2). We also need to generate the scattering azimuths/angles. The four types of single scattering are all isotropic in the assumed frequency range which means the scattered-wave amplitudes are independent of incident/scattered-wave angles/azimuths (e.g. Maeda *et al.*, 2008). Thus the scattering azimuth distributions are uniform. We repeat the propagation and scattering until the sum of τ reaches a certain time in the simulation. After N simulations, we count how many P and Rayleigh waves exist at each time step and the result is the P- and Rayleigh-wave energy.

We calculate the cross sections (Equation 7.7 7.8, 7.11 and 7.12) and mean free times (Equation 7.14). We set the media parameters as: α_0=5 km/s, β_0=3 km/s and thus c_R=2.74 km/s (Rayleigh, 1885). We compute the Rayleigh-wave eigenfunctions based on these velocities (Appendix D.1). We assume that the scatterers ($\delta\lambda$) are randomly distributed in the media and set $n = 2\ m^{-3}$.

7.4.1 Simulation without the free-surface P-S coupling

We first validate the simulation algorithm using a model without the P-S coupling at the free surface. We simulate the multiply scattering process 10^7 times. We place initial waves at 1 km depth and set the frequency to be 1 Hz. The boundary condition at Earth's surface is a total reflection. We conduct multiple simulations with different initial wave types. We set the initial wave types to be all P waves, half P and half Rayleigh waves, and all Rayleigh waves (Figure 7.1). In these three cases, the energy ratios between the multiply-scattered Rayleigh and P waves all converge to the theoretical prediction (Equation 7.15).

Algorithm 2 Monte Carlo simulation algorithm

$\sigma^{be} = \sigma^{PP} + max[\sigma^{PR}(z)]$ ▷ Effective body-wave cross section
$\tau^{be} = 1/n/\sigma^{be}/vp$ ▷ Effective mean free time
$\sigma^{R} = \sigma^{RR} + \sigma^{RP}$; ▷ Rayleigh wave cross section
$\tau^{R} = 1/n/\sigma^{R}/vr$ ▷ Rayleigh wave mean free time
for $i = 1 : N$th particle/simulation **do**
generating a particle and its **mode** can be body (b) or surface (s) waves ▷ Initialization
if mode == b **then**
$\tau = -ln(rand) * \tau^{be}$ ▷ Generate a random free time from a random number
ang = acos(-1+2*rand) ▷ A random angle in [0,π]
azi = 2*pi*rand ▷ A random propagation azimuth in [0,2π]
kx = sin(ang)*cos(azi) ▷ P-wave propagation vectors in x/y/z direction
ky = sin(ang)*sin(azi)
kz = cos(ang);
else
$\tau = -ln(rand) * \tau^{R}$
azi = 2*pi*rand ▷ A random propagation azimuth in [0,2π]
kx = cos(azi) ▷ Rayleigh-wave propagation vectors in x/y direction
ky = sin(azi)
deltat = dt
while itime < Nstep **do** ▷ ith simulation starts
if Mode == b **then** ▷ P-wave propagation
if $\tau >$ deltat **then** ▷ No scatterings happen
x = x+deltat*vp*kx; y = y+deltat*vp*ky; z = z+deltat*vp*kz
if z < 0 **then** ▷ **Encount the free surface**
z = -z; kz = -kz
it = it+1
deltat = dt
else ▷ A scattering will happen
x = x+τ*vp*kx; y = y+τ*vp*ky; z = z+τ*vp*kz
if z < 0 **then** ▷ **Encount the free surface**
z = -z; kz = -kz
deltat = deltat - τ
scatterb() ▷ P-wave scattering
if Mode == s **then** ▷ Rayleigh-wave propagation
if $\tau >$ deltat **then** ▷ No scatterings happen
x = x+deltat*vr*kx; y = y+deltat*vr*ky
it = it+1
τ = τ - deltat
deltat = dt
else ▷ A scattering will happen
x = x+τ*vr*kx; y = y+τ*vr*ky
deltat = deltat - τ
scatters() ▷ Rayleigh-wave scattering

Algorithm 3 P-wave scattering subprogram: scatterb()

pbs = $(\sigma^{PR}(z)+\sigma^{PP})/\sigma^{be}$ ▷ Possibility for real scatterings happening
if rand < pbs **then**
  pbb = $\sigma^{PP}/(\sigma^{PR}(z)+\sigma^{PP})$ ▷ Possibility for P-P scattering
  if rand < pbb **then** ▷ P-P scattering
    mode = b
    $\tau = -ln(rand) * \tau^{be}$ ▷ Generate a random free time from a random number
    ang = acos(-1+2*rand) ▷ A random angle in [0,π]
    azi = 2*pi*rand ▷ A random propagation azimuth in [0,2π]
    kx = sin(ang)*cos(azi) ▷ P-wave propagation vectors in x/y/z direction
    ky = sin(ang)*sin(azi)
    kz = cos(ang);
  else ▷ P-Rayleigh scattering
    mode = s
    $\tau = -ln(rand) * \tau^{s}$
    azi = 2*pi*rand ▷ A random propagation azimuth in [0,2π]
    kx = cos(azi) ▷ Rayleigh-wave propagation vectors in x/y direction
    ky = sin(azi)
else ▷ Imaginary scattering happens
  mode = b
  $\tau = -ln(rand) * \tau^{be}$ ▷ The propagation direction stays the same

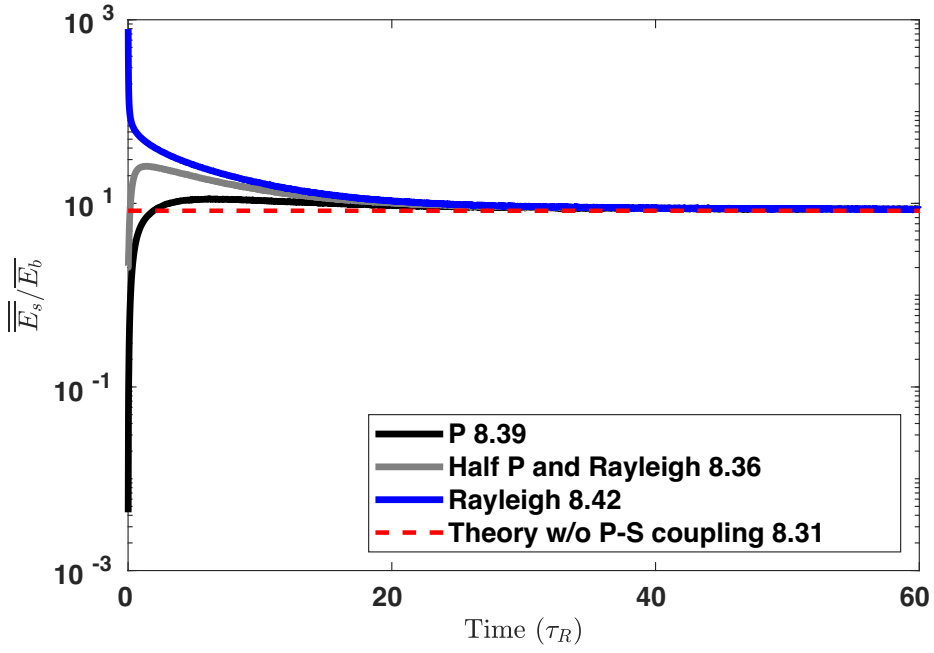

Figure 7.1: The energy ratios evolve with time between the total Rayleigh-wave energy and the average P-wave energy in the 1 km depth from the surface. The time is normalized by the mean free time of Rayleigh waves (τ_R). The values in the legend indicate the average energy ratio in the last 10 τ_R in each simulation and the theoretical value.

Algorithm 4 Rayleigh-wave scattering subprogram: scatters()

```
pss = σ^RR/σ^R                                   ▷ Possibility for R-R scattering
if rand < pss then                                                ▷ R-R scattering
    mode = s
    τ = −ln(rand) ∗ τ^s
    azi = 2*pi*rand                          ▷ A random propagation azimuth in [0,2π]
    kx = cos(azi)                ▷ Rayleigh-wave propagation vectors in x/y direction
    ky = sin(azi)
else                                                              ▷ R-P scattering
    mode = b
        ▷ Generate a depth based on the distribution of R-P cross section in depth
    z = interp1(zvec,σ^RP(zvec)/∫σ^PR(z)dz,rand)
    τ = −ln(rand) ∗ τ^be      ▷ Generate a random free time from a random number
    ang = acos(-1+2*rand)                                ▷ A random angle in [0,π]
    azi = 2*pi*rand                          ▷ A random propagation azimuth in [0,2π]
    kx = sin(ang)*cos(azi)           ▷ P-wave propagation vectors in x/y/z direction
    ky = sin(ang)*sin(azi)
    kz = cos(ang);
```

7.4.2 Simulation with the free surface P-S coupling

We consider the P-S coupling in this simulation. We change the boundary condition at the surface to the physical P-wave free-surface reflection (e.g. Aki & Richards, 2002). P waves can continue as P waves or convert to S waves in the free surface reflection. To deal with the reflection, we generate a random possibility from 0 to 1, and compare the possibility to the ratio between reflected and incident P-wave intensities. If the the possibility is lower, the incident P waves will not convert; if higher, the incident P waves will convert to reflected S waves. The reflected/down-going S waves do not interact with the scatters ($\delta\lambda$). Thus the reflected S waves will not covert to P or Rayleigh waves and thus behave as leaky energy. Therefore, there are fewer P waves in this simulation compared to the simulation without the free surface P-S coupling and thus the energy equipartition ratio becomes higher (Figure 7.2).

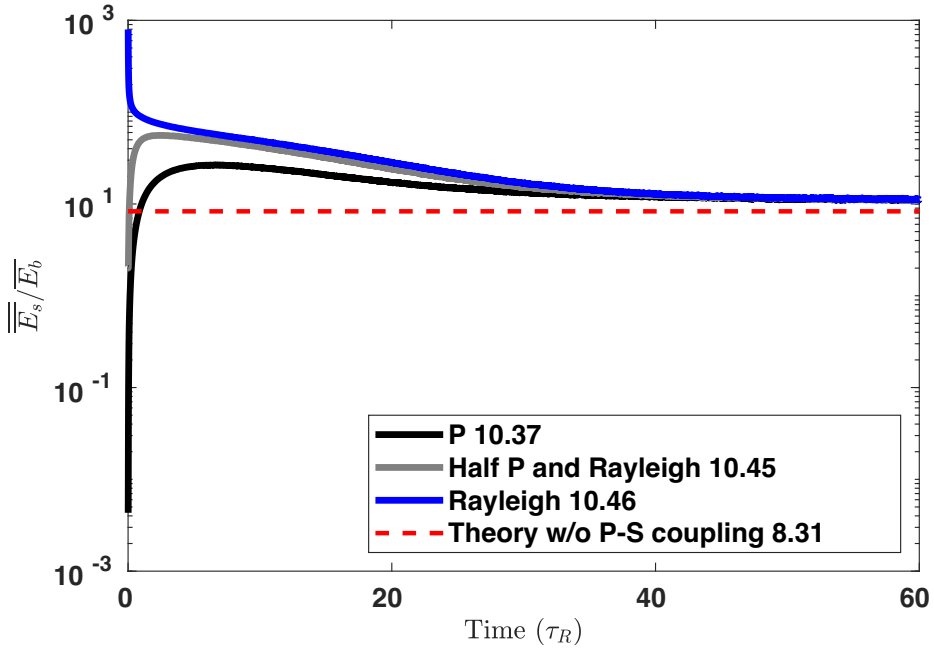

Figure 7.2: Same as Figure 7.1 but with the free surface P-S coupling in the three simulations.

7.5 Conclusion

We present a Monte Carlo simulation for multiply-scattered P and Rayleigh waves in an elastic homogeneous media. We consider perturbations in *Lamé* parameters acting as scatters in the simulations. The simulations provide the temporal evolution of the energy ratio between the multiply-scattered Rayleigh and P waves. The simulations without a free surface produce an energy equipartition ratio that matches the theoretical prediction. The simulations with the free surface produce a higher energy ratio than the simulations without the free surface, because of the leakage of converted S waves from the P-wave reflection at the free surface. This study is a first step toward a complete modeling of multiply-scattered body and surface waves in elastic media.

CHAPTER 8:

CONCLUDING REMARKS

My Ph.D. dissertation mainly covers three research areas in seismic interferometry (SI): estimating accurate direct Rayleigh-wave phase velocities, estimating ambient seismic source distributions with full-waveform inversion, and more accurately modelling elastic multiply-scattered waves. I state the main conclusions in each chapter, and thus I will not restate the conclusions here. However, I do state some ideas about future research directions regarding the material covered in this disseration.

8.1 Joint inversion between source and structure

A joint inversion between seismic sources and structures is necessary because the two are coupled (e.g. Valentine & Woodhouse, 2010; Fichtner, 2015). Thus we need to update the two in inversions either simultaneously (e.g. Valentine & Woodhouse, 2010; Sager *et al.*, 2018) or iteratively (e.g. Lee *et al.*, 2014). In the inversions, one would use low-resolution misfit functions in the beginning, such as symmetry differences (Ermert *et al.*, 2015) and/or envelope differences (e.g. Fichtner *et al.*, 2008; Bozdağ *et al.*, 2011). These misfit functions are robust to starting models (e.g. Sager *et al.*, 2018) but do not possess the high resolution necessary for source and/or structure imaging. Thus, in order to increase the resolution, one should switch to high-resolution misfit functions like L_2 waveform differences at some point in the

inversion (e.g. Pan *et al.*, 2020).

Attenuation models, as well as velocity models, are important for subsurface investigation. We know that we should not use a crosscorrelation between two sensors to approximate the Green's function between the two sensors (e.g. Yang & Ritzwoller, 2008; Halliday & Curtis, 2008; Yao & Van Der Hilst, 2009). The amplitude from the crosscorrelation is often biased, and estimating accurate attenuation information from the biased amplitudes requires the seismic source distribution (e.g. Stehly & Boué, 2017). However, as we stated in Chapter 5, estimating the seismic source distribution requires accurate subsurface attenuation models, which is our original goal. Thus the whole logic is circular. We normally do not have good reference attenuation models to break this circularity. Therefore, how to estimate seismic source distributions without a reference attenuation model is a challenge for estimation of attenuation models and requires further attention.

This challenge might be addressed with a joint inversion for velocity and attenuation models (e.g. Fabien-Ouellet *et al.*, 2017) in active-source seismic studies, but for ambient seismic (noise) research, the joint inversion should include the source distribution, in addition to velocity and attenuation models.

8.2 Ambient seismic source solutions

Ambient seismic sources (e.g. primary microseism) usually possess both vertical and horizontal forces (e.g. Ardhuin *et al.*, 2015), even moment tensors if necessary. Moreover, current research suggests that horizontal-force sources may not be in the same locations as vertical-force sources (e.g. Juretzek & Hadziioannou, 2016). Thus in order to fully study these sources, we need more complicated (e.g. vertical and horizontal force) source models than only vertical forces at Earth's surface. However, this

increase in the complexity of source models would increase the model space of the source inversion and thus make the convergence to the global minimum harder in the inversion. Furthermore, because of Rayleigh-wave eigenfunctions, the inverted source strengths will be biased if the sources are in depth instead of at the Earth's surface. Therefore, in these cases, how to achieve accurate source distribution estimations is a challenge. One option to reduce the model space is that we can set possible source forces based on the knowledge of source mechanisms. For example, the interaction between sea current and the sea floor can generate vertical and horizontal forces on the sea floor (e.g. Ardhuin *et al.*, 2015). Therefore we will incorporate the vertical-, north- and east-direction point forces into the source inversion for the primary microseism in future.

8.3 Time-lapse monitoring

The coda-wave monitoring method is still rapidlly developing. Nowadays, one can monitor changes in coda waves (e.g. Brenguier *et al.*, 2007), but has no idea if the changes are caused by multiply-scattered body or surface waves. Furthermore, one can not accurately map the coda wave changes to the changes in the subsurface because one does not have multiply-scattered elastic-wave sensitivity kernels, but instead only acoustic-wave sensitivity kernels in homogeneous media (e.g. Larose *et al.*, 2007). We still need to work on the theory to calculating multiply-scattered body-/surface-wave sensitivity kernels for $\delta\lambda/\delta\mu/\delta\rho$ in (laterally) homogeneous media. Besides these issues, in practice, we also need to incorporate topography into the sensitivity kernels because the topography can affect coda wave propagation and wavefield scattering (e.g. Snieder, 1986b; Takemura *et al.*, 2015).

One can also use direct waves to monitor small changes in the subsurface (e.g.

Takano *et al.*, 2019). The advantages for using direct waves are that the wave type for direct waves is clear and thus one can easily calculate the sensitivity kernels (e.g. Dahlen *et al.*, 2000; Tromp *et al.*, 2005). However, compared to the coda waves, the direct waves are less stable to the changes in seismic source distribution (e.g. Hadziioannou *et al.*, 2009). Thus how to assess or suppress the source effect is key to the direct-wave monitoring method.

REFERENCES

Aki, Keiiti, & Richards, Paul G. 2002. *Quantitative Seismology.* Science Books.

An, Meijian, Wiens, Douglas A, Zhao, Yue, Feng, Mei, Nyblade, Andrew A, Kanao, Masaki, Li, Yuansheng, Maggi, Alessia, & Lévêque, Jean-Jacques. 2015. S-velocity model and inferred Moho topography beneath the Antarctic Plate from Rayleigh waves. *Journal of Geophysical Research: Solid Earth*, **120**(1), 359–383.

Arai, Hiroshi, & Tokimatsu, Kohji. 2004. S-wave velocity profiling by inversion of microtremor H/V spectrum. *Bulletin of the Seismological Society of America*, **94**(1), 53–63.

Ardhuin, Fabrice, Tournadre, Jean, Queffeulou, Pierre, Girard-Ardhuin, Fanny, & Collard, Fabrice. 2011a. Observation and parameterization of small icebergs: Drifting breakwaters in the southern ocean. *Ocean Modelling*, **39**(3-4), 405–410.

Ardhuin, Fabrice, Stutzmann, Eleonore, Schimmel, Martin, & Mangeney, Anne. 2011b. Ocean wave sources of seismic noise. *Journal of Geophysical Research: Oceans*, **116**(C9).

Ardhuin, Fabrice, Gualtieri, Lucia, & Stutzmann, Eléonore. 2015. How ocean waves rock the Earth: Two mechanisms explain microseisms with periods 3 to 300 s. *Geophysical Research Letters*, **42**(3), 765–772.

Artman, Brad, Podladtchikov, Igor, & Witten, Ben. 2010. Source location using time-reverse imaging. *Geophysical Prospecting*, **58**(5), 861–873.

Aster, Richard C, Borchers, Brian, & Thurber, Clifford H. 2011. *Parameter estimation and inverse problems*. Vol. 90. Academic Press.

Baig, Adam M, Campillo, Michel, & Brenguier, Florent. 2009. Denoising seismic noise cross correlations. *Journal of Geophysical Research: Solid Earth*, **114**(B8).

Bakulin, Andrey, & Calvert, Rodney. 2006. The virtual source method: Theory and case study. *Geophysics*, **71**(4), SI139.

Bensen, G D, Ritzwoller, M H, Barmin, M P, Levshin, A L, Lin, F, Moschetti, M P, & Yang, Y. 2007. Processing seismic ambient noise data to obtain reliable broad-band surface wave dispersion measurements. *Geophysical Journal International*, **169**(3), 1239–1260.

Billings, SD, Sambridge, MS, & Kennett, BLN. 1994. Errors in hypocenter location: picking, model, and magnitude dependence. *Bulletin of the Seismological Society of America*, **84**(6), 1978–1990.

Boaga, Jacopo, Cassiani, Giorgio, Strobbia, Claudio L, & Vignoli, Giulio. 2013. Mode misidentification in Rayleigh waves: Ellipticity as a cause and a cure. *Geophysics*, **78**(4), EN17–EN28.

Bonnefoy-Claudet, Sylvette, Cornou, Cécile, Bard, Pierre Yves, Cotton, Fabrice, Moczo, Peter, Kristek, Jozef, & Fäh, Donat. 2006. H/V ratio: A tool for site effects evaluation. Results from 1-D noise simulations. *Geophysical Journal International*, **167**(2), 827–837.

Boué, Pierre, Denolle, Marine, Hirata, Naoshi, Nakagawa, Shigeki, & Beroza, Gregory C. 2016. Beyond basin resonance: characterizing wave propagation using a dense array and the ambient seismic field. *Geophysical Journal International*, **206**(2), 1261–1272.

Bozdağ, Ebru, Trampert, Jeannot, & Tromp, Jeroen. 2011. Misfit functions for full waveform inversion based on instantaneous phase and envelope measurements. *Geophysical Journal International*, **185**(2), 845–870.

Brenguier, Florent, Shapiro, Nikolai M, Campillo, Michel, Nercessian, Alexandre, & Ferrazzini, Valérie. 2007. 3-D surface wave tomography of the Piton de la Fournaise volcano using seismic noise correlations. *Geophysical research letters*, **34**(2).

Brenguier, Florent, Shapiro, Nikolai M, Campillo, Michel, Ferrazzini, Valérie, Duputel, Zacharie, Coutant, Olivier, & Nercessian, Alexandre. 2008. Towards forecasting volcanic eruptions using seismic noise. *Nature Geoscience*, **1**(2), 126.

Bussert, Robert, Kämpf, Horst, Flechsig, Christina, Hesse, Katja, Nickschick, Tobias, Liu, Qi, Umlauft, Josefine, Vylita, Tomáš, Wagner, Dirk, Wonik, Thomas, *et al.* 2017. Drilling into an active mofette: pilot-hole study of the impact of CO_2-rich mantle-derived fluids on the geo–bio interaction in the western Eger Rift (Czech Republic). *Scientific Drilling*, **23**, 13.

Campillo, Michel, & Paul, Anne. 2003. Long-range correlations in the diffuse seismic coda. *Science*, **299**(5606), 547–549.

Cessaro, Robert K. 1994. Sources of primary and secondary microseisms. *Bulletin of the Seismological Society of America*, **84**(1), 142–148.

Cheng, Feng, Xia, Jianghai, Xu, Yixian, Xu, Zongbo, & Pan, Yudi. 2015. A new passive seismic method based on seismic interferometry and multichannel analysis of surface waves. *Journal of Applied Geophysics*, **117**, 126–135.

Cheng, Feng, Xia, Jianghai, Luo, Yinhe, Xu, Zongbo, Wang, Limin, Shen, Chao, Liu, Ruofei, Pan, Yudi, Mi, Binbin, & Hu, Yue. 2016. Multi-channel analysis of passive surface waves based on cross-correlations. *Geophysics*, **81**(5), EN57–EN66.

Chmiel, Malgorzata, Roux, Philippe, Herrmann, Philippe, Rondeleux, Baptiste, & Wathelet, Marc. 2018. Data-based diffraction kernels for surface waves from convolution and correlation processes through active seismic interferometry. *Geophysical Journal International*, **214**(2), 1468–1480.

Civilini, Francesco, Pancha, Aasha, Savage, Martha Kane, Sewell, Steven, & Townend, John. 2016. Inferring shear-velocity structure of the upper 200 m using cultural ambient noise at the Ngatamariki geothermal field, Central North Island, New Zealand. *Interpretation*, **4**(3), SJ87–SJ101.

Clarke, Daniel, Zaccarelli, Lucia, Shapiro, NM, & Brenguier, Florent. 2011. Assessment of resolution and accuracy of the Moving Window Cross Spectral technique for monitoring crustal temporal variations using ambient seismic noise. *Geophysical Journal International*, **186**(2), 867–882.

Corciulo, Margherita, Roux, Philippe, Campillo, Michel, Dubucq, Dominique, & Kuperman, WA. 2012. Multiscale matched-field processing for noise-source localization in exploration geophysics. *Geophysics*, **77**(5), KS33–KS41.

Cros, Estelle, Roux, Philippe, Vandemeulebrouck, Jean, & Kedar, S. 2011. Locating

hydrothermal acoustic sources at Old Faithful Geyser using matched field processing. *Geophysical Journal International*, **187**(1), 385–393.

Dahlen, FA, Hung, S-H, & Nolet, Guust. 2000. Fréchet kernels for finite-frequency traveltimes-I. Theory. *Geophysical Journal International*, **141**(1), 157–174.

Dahlen, FAand, & Tromp, Jeroen. 1998. *Theoretical global seismology*. Princeton university press.

Delaney, Evan, Ermert, Laura, Sager, Korbinian, Kritski, Alexander, Bussat, Sascha, & Fichtner, Andreas. 2017. Passive seismic monitoring with nonstationary noise sources. *Geophysics*, **82**(4), KS57–KS70.

Eisner, Leo, Duncan, Peter M, Heigl, Werner M, & Keller, William R. 2009. Uncertainties in passive seismic monitoring. *The Leading Edge*, **28**(6), 648–655.

Ermert, Laura, Villaseñor, Antonio, & Fichtner, Andreas. 2015. Cross-correlation imaging of ambient noise sources. *Geophysical Journal International*, **204**(1), 347–364.

Ermert, Laura, Sager, Korbinian, Afanasiev, Michael, Boehm, Christian, & Fichtner, Andreas. 2017. Ambient seismic source inversion in a heterogeneous Earth-Theory and application to the Earth's hum. *Journal of Geophysical Research: Solid Earth*.

Estrella, H Flores, Umlauft, Josefine, Schmidt, Andreas, & Korn, Michael. 2016. Locating mofettes using seismic noise records from small dense arrays and matched field processing analysis in the NW Bohemia/Vogtland Region, Czech Republic. *Near Surface Geophysics*, **14**(4), 327–335.

Fabien-Ouellet, Gabriel, Gloaguen, Erwan, & Giroux, Bernard. 2017. Time domain viscoelastic full waveform inversion. *Geophysical Journal International*, **209**(3), 1718–1734.

Fan, Yuanzhong, & Snieder, Roel. 2009. Required source distribution for interferometry of waves and diffusive fields. *Geophysical Journal International*, **179**(2), 1232–1244.

Fichtner, Andreas. 2014. Source and processing effects on noise correlations. *Geophysical Journal International*, **197**(3), 1527–1531.

Fichtner, Andreas. 2015. Source-structure trade-offs in ambient noise correlations. *Geophysical Journal International*, **202**(1), 678–694.

Fichtner, Andreas, Kennett, Brian LN, Igel, Heiner, & Bunge, Hans-Peter. 2008. Theoretical background for continental-and global-scale full-waveform inversion in the time–frequency domain. *Geophysical Journal International*, **175**(2), 665–685.

Fichtner, Andreas, Stehly, Laurent, Ermert, Laura, & Boehm, Christian. 2017. Generalised interferometry-I. Theory for inter-station correlations. *Geophysical Journal International*, **208**, 603–638.

Froment, Berenice, Campillo, Michel, Roux, Philippe, Gouedard, Pierre, Verdel, Arie, & Weaver, Richard L. 2010. Estimation of the effect of nonisotropically distributed energy on the apparent arrival time in correlations. *Geophysics*, **75**(5), SA85–SA93.

Froment, Bérénice, Campillo, Michel, & Roux, Philippe. 2011. Reconstructing the Green's function through iteration of correlations. *Comptes Rendus - Geoscience*, **343**(8-9), 623–632.

Garofalo, Flora, Foti, Sebastiano, Hollender, F, Bard, PY, Cornou, Cécile, Cox, BR, Ohrnberger, M, Sicilia, D, Asten, M, Di Giulio, G, *et al.* 2016. InterPACIFIC project: Comparison of invasive and non-invasive methods for seismic site characterization. Part I: Intra-comparison of surface wave methods. *Soil Dynamics and Earthquake Engineering*, **82**, 222–240.

Greene, Chad A, Gwyther, David E, & Blankenship, Donald D. 2017. Antarctic mapping tools for MATLAB. *Computers & Geosciences*, **104**, 151–157.

Grêt, Alexander, Snieder, Roel, Aster, Richard C, & Kyle, Philip R. 2005. Monitoring rapid temporal change in a volcano with coda wave interferometry. *Geophysical Research Letters*, **32**(6).

Gribler, Gabriel, Liberty, Lee M., Mikesell, T. Dylan, & Michaels, Paul. 2016. Isolating retrograde and prograde Rayleigh-wave modes using a polarity mute. *Geophysics*, **81**(5), V379–V385.

Groos, JC, Bussat, S, & Ritter, JRR. 2012. Performance of different processing schemes in seismic noise cross-correlations. *Geophysical Journal International*, **188**(2), 498–512.

Groos, Lisa, Schäfer, Martin, Forbriger, Thomas, & Bohlen, Thomas. 2014. The role of attenuation in 2D full-waveform inversion of shallow-seismic body and Rayleigh waves. *Geophysics*, **79**(6), R247–R261.

Groos, Lisa, Schäfer, Martin, Forbriger, Thomas, & Bohlen, Thomas. 2017. Application of a complete workflow for 2D elastic full-waveform inversion to recorded shallow-seismic Rayleigh waves. *Geophysics*, **82**(2), R109–R117.

Gualtieri, L, Stutzmann, E, Juretzek, Carina, Hadziioannou, C, & Ardhuin, F. 2019. Global scale analysis and modelling of primary microseisms. *Geophysical Journal International*, **218**(1), 560–572.

Hadziioannou, Céline, Larose, Eric, Coutant, Olivier, Roux, Philippe, & Campillo, Michel. 2009. Stability of monitoring weak changes in multiply scattering media with ambient noise correlation: Laboratory experiments. *The Journal of the Acoustical Society of America*, **125**(6), 3688–3695.

Halliday, David, & Curtis, Andrew. 2008. Seismic interferometry, surface waves and source distribution. *Geophysical Journal International*, **175**(3), 1067–1087.

Halliday, David, Curtis, Andrew, & Kragh, Ed. 2008. Seismic surface waves in a suburban environment: active and passive interferometric methods. *Leading Edge*, **7**(2), 210–218.

Haney, Matthew M, & Nakahara, Hisashi. 2014. Surface-wave Green's tensors in the near field. *Bulletin of the Seismological Society of America*, **104**(3), 1578–1586.

Haney, Matthew M, Mikesell, T Dylan, van Wijk, Kasper, & Nakahara, Hisashi. 2012. Extension of the spatial autocorrelation (SPAC) method to mixed-component correlations of surface waves. *Geophysical Journal International*, **191**(1), 189–206.

Harmon, Nicholas, Rychert, Catherine, & Gerstoft, Peter. 2010. Distribution of noise sources for seismic interferometry. *Geophysical Journal International*, **183**(3), 1470–1484.

Haskell, Norman A. 1953. The dispersion of surface waves on multilayered media. *Bulletin of the Seismological Society of America*, **43**(1), 17–34.

Hasselmann, K. 1963. A statistical analysis of the generation of microseisms. *Reviews of Geophysics*, **1**(2), 177–210.

He, Yanping, Monahan, Adam H, & McFarlane, Norman A. 2013. Diurnal variations of land surface wind speed probability distributions under clear-sky and low-cloud conditions. *Geophysical Research Letters*, **40**(12), 3308–3314.

Hoshiba, Mitsuyuki. 1991. Simulation of multiple-scattered coda wave excitation based on the energy conservation law. *Physics of the Earth and Planetary Interiors*, **67**(1-2), 123–136.

Hutt, Charles R, Ringler, Adam T, & Gee, Lind S. 2017. Broadband Seismic Noise Attenuation versus Depth at the Albuquerque Seismological LaboratoryBroadband Seismic Noise Attenuation versus Depth at the Albuquerque Seismological Laboratory. *Bulletin of the Seismological Society of America*, **107**(3), 1402–1412.

Ikeda, Tatsunori, Tsuji, Takeshi, Watanabe, Toshiki, & Yamaoka, Koshun. 2016. Development of surface-wave monitoring system for leaked CO_2 using a continuous and controlled seismic source. *International Journal of Greenhouse Gas Control*, **45**, 94–105.

Ishii, Miaki, Shearer, Peter M, Houston, Heidi, & Vidale, John E. 2005. Extent, duration and speed of the 2004 Sumatra–Andaman earthquake imaged by the Hi-Net array. *Nature*, **435**(7044), 933.

Iverson, Richard M. 2000. Landslide triggering by rain infiltration. *Water resources research*, **36**(7), 1897–1910.

Johansen, HK. 1977. A man/computer interpretation system for resistivity soundings over a horizontally strafified earth. *Geophysical Prospecting*, **25**(4), 667–691.

Juretzek, C, & Hadziioannou, C. 2016. Where do ocean microseisms come from? A study of Love-to-Rayleigh wave ratios. *Journal of Geophysical Research: Solid Earth*, **121**(9), 6741–6756.

Kennett, Brian LN, Engdahl, ER, & Buland, R. 1995. Constraints on seismic velocities in the Earth from traveltimes. *Geophysical Journal International*, **122**(1), 108–124.

Komatitsch, Dimitri, & Tromp, Jeroen. 2002. Spectral-element simulations of global seismic wave propagation-I. Validation. *Geophysical Journal International*, **149**(2), 390–412.

Kramer, Steven L. 2002. *Geotechnical Earthquake Engineering*. Prentice Hall, Inc.

Lagendijk, Ad, & Van Tiggelen, Bart A. 1996. Resonant multiple scattering of light. *Physics Reports*, **270**(3), 143–215.

Lai, Carlo G, Rix, Glenn J, Foti, Sebastiano, & Roma, Vitantonio. 2002. Simultaneous measurement and inversion of surface wave dispersion and attenuation curves. *Soil Dynamics and Earthquake Engineering*, **22**(9-12), 923–930.

Larose, Eric, Roux, Philippe, & Campillo, Michel. 2007. Reconstruction of Rayleigh-Lamb dispersion spectrum based on noise obtained from an air-jet forcing. *The Journal of the Acoustical Society of America*, **122**(6), 3437–3444.

Larose, Eric, Planes, Thomas, Rossetto, Vincent, & Margerin, Ludovic. 2010. Locating a small change in a multiple scattering environment. *Applied Physics Letters*, **96**(20), 204101.

Lavergne, Thomas, Sørensen, Atle Macdonald, Kern, Stefan, Tonboe, Rasmus, Notz, Dirk, Aaboe, Signe, Bell, Louisa, Dybkjær, Gorm, Eastwood, Steinar, Gabarro, Carolina, *et al.* 2019. Version 2 of the EUMETSAT OSI SAF and ESA CCI sea-ice concentration climate data records. *Cryosphere*, **13**(1), 49–78.

Lawrence, Jesse F., Denolle, Marine, Seats, Kevin J., & Prieto, Germán A. 2013. A numeric evaluation of attenuation from ambient noise correlation functions. *Journal of Geophysical Research: Solid Earth*, **118**(12), 6134–6145.

Lee, En-Jui, Chen, Po, Jordan, Thomas H, Maechling, Phillip B, Denolle, Marine AM, & Beroza, Gregory C. 2014. Full-3-D tomography for crustal structure in southern California based on the scattering-integral and the adjoint-wavefield methods. *Journal of Geophysical Research: Solid Earth*, **119**(8), 6421–6451.

Lin, Fan-Chi, Moschetti, Morgan P, & Ritzwoller, Michael H. 2008. Surface wave tomography of the western United States from ambient seismic noise: Rayleigh and Love wave phase velocity maps. *Geophysical Journal International*, **173**(1), 281–298.

Lin, Fan-Chi, Li, Dunzhu, Clayton, Robert W, & Hollis, Dan. 2013. High-resolution 3D shallow crustal structure in Long Beach, California: Application of ambient noise tomography on a dense seismic array. *Geophysics*, **78**(4), Q45–Q56.

Liu, Qinya, Polet, Jascha, Komatitsch, Dimitri, & Tromp, Jeroen. 2004. Spectral-

element moment tensor inversions for earthquakes in southern California. *Bulletin of the Seismological Society of America*, **94**(5), 1748–1761.

Lobkis, Oleg I., & Weaver, Richard L. 2001. On the emergence of the Green's function in the correlations of a diffuse field. *The Journal of the Acoustical Society of America*, **110**(6), 3011–3017.

Longuet-Higgins, Michael Selwyn. 1950. A theory of the origin of microseisms. *Philosophical Transactions of the Royal Society of London. Series A, Mathematical and Physical Sciences*, **243**(857), 1–35.

Louie, John N. 2001. Faster, better: shear-wave velocity to 100 meters depth from refraction microtremor arrays. *Bulletin of the Seismological Society of America*, **91**(2), 347–364.

Luo, Yi, & Schuster, Gerard T. 1991. Wave-equation traveltime inversion. *Geophysics*, **56**(5), 645–653.

Luo, Yinhe, Xia, Jianghai, Miller, Richard D, Xu, Yixian, Liu, Jiangping, & Liu, Qingsheng. 2008. Rayleigh-wave dispersive energy imaging using a high-resolution linear Radon transform. *Pure and Applied Geophysics*, **165**(5), 903–922.

Luo, Yinhe, Yang, Yingjie, Zhao, Kaifeng, Xu, Yixian, & Xia, Jianghai. 2015. Unraveling overtone interferences in Love-wave phase velocity measurements by radon transform. *Geophysical Journal International*, **203**(1), 327–333.

Lux, Iván, & Koblinger, László. 1991. *Monte Carlo particle transport methods: neutron and photon calculations*. CRC Press.

Ma, Yiran, Clayton, Robert W., & Li, Dunzhu. 2016. Higher-mode ambient-noise Rayleigh waves in sedimentary basins. *Geophysical Journal International*, **206**(3), 1634–1644.

Maeda, Takuto, Sato, Haruo, & Nishimura, Takeshi. 2008. Synthesis of coda wave envelopes in randomly inhomogeneous elastic media in a half-space: single scattering model including Rayleigh waves. *Geophysical Journal International*, **172**(1), 130–154.

Maggi, Alessia, Tape, Carl, Chen, Min, Chao, Daniel, & Tromp, Jeroen. 2009. An automated time-window selection algorithm for seismic tomography. *Geophysical Journal International*, **178**(1), 257–281.

Mainsant, Guénolé, Larose, Eric, Brönnimann, Cornelia, Jongmans, Denis, Michoud, Clément, & Jaboyedoff, Michel. 2012. Ambient seismic noise monitoring of a clay landslide: Toward failure prediction. *Journal of Geophysical Research: Earth Surface*, **117**(F1).

Margerin, Ludovic, Campillo, Michel, & Van Tiggelen, Bart. 2000. Monte Carlo simulation of multiple scattering of elastic waves. *Journal of Geophysical Research: Solid Earth*, **105**(B4), 7873–7892.

Margerin, Ludovic, Bajaras, Andres, & Campillo, Michel. 2019. A scalar radiative transfer model including the coupling between surface and body waves. *Geophysical Journal International*, **219**(2), 1092–1108.

McMechan, George A, & Yedlin, Mathew J. 1981. Analysis of dispersive waves by wave field transformation. *Geophysics*, **46**(6), 869–874.

Melo, Gabriela, Malcolm, Alison, Mikesell, Thomas Dylan, & van Wijk, Kasper. 2013. Using SVD for improved interferometric Green's function retrieval. *Geophysical Journal International*, **194**(3), 1596–1612.

Michaels, P, & Smith, RB. 1997. Surface wave inversion by neural networks (radial basis functions) for engineering applications. *Journal of Environmental and Engineering Geophysics*, **2**(1), 65–76.

Mikesell, Thomas Dylan, van Wijk, Kasper, Calvert, Alexander, & Haney, Matthew M. 2009. The virtual refraction: Useful spurious energy in seismic interferometry. *Geophysics*, **74**(3), A13.

Mikesell, Thomas Dylan, van Wijk, Kasper, Blum, Thomas E., Snieder, Roel, & Sato, Haruo. 2012. Analyzing the coda from correlating scattered surface waves. *The Journal of the Acoustical Society of America*, **131**(mar), EL275.

Mousavi, S Mostafa, Langston, Charles A, & Horton, Stephen P. 2016. Automatic microseismic denoising and onset detection using the synchrosqueezed continuous wavelet transform. *Geophysics*, **81**(4), V341–V355.

Mulargia, Francesco. 2012. The seismic noise wavefield is not diffuse. *The Journal of the Acoustical Society of America*, **131**(4), 2853.

Nakahara, Hisashi. 2006. A systematic study of theoretical relations between spatial correlation and Green's function in one-, two- and three-dimensional random scalar wavefields. *Geophys. J. Int.*, **167**(3), 1097–1105.

Nakata, Nori. 2016. Near-surface S-wave velocities estimated from traffic-induced

Love waves using seismic interferometry with double beamforming. *Interpretation*, **4**(4), SQ23–SQ31.

Nakata, Nori, Chang, Jason P, Lawrence, Jesse F, & Boué, Pierre. 2015. Body wave extraction and tomography at Long Beach, California, with ambient-noise interferometry. *Journal of Geophysical Research: Solid Earth*, **120**(2), 1159–1173.

Nakata, Nori, Boué, Pierre, Brenguier, Florent, Roux, Philippe, Ferrazzini, Valérie, & Campillo, Michel. 2016. Body- and surface-wave reconstruction from seismic-noise correlations between arrays at Piton de la Fournaise volcano. *Geophysical Research Letters*, **43**(3), 1047–1054.

Nakata, Norimitsu, Snieder, Roel, Tsuji, Takeshi, Larner, Ken, & Matsuoka, Toshifumi. 2011. Shear wave imaging from traffic noise using seismic interferometry by cross-coherence. *Geophysics*, **76**(6), SA97–SA106.

Nickschick, Tobias, Kämpf, Horst, Flechsig, Christina, Mrlina, Jan, & Heinicke, Jens. 2015. CO_2 degassing in the Hartoušov mofette area, western Eger Rift, imaged by CO_2 mapping and geoelectrical and gravity surveys. *International Journal of Earth Sciences*, **104**(8), 2107–2129.

Nishida, Kiwamu, & Fukao, Yoshio. 2007. Source distribution of Earth's background free oscillations. *Journal of Geophysical Research: Solid Earth*, **112**(B6).

Nishida, Kiwamu, Kawakatsu, Hitoshi, Fukao, Yoshio, & Obara, Kazushige. 2008. Background Love and Rayleigh waves simultaneously generated at the Pacific Ocean floors. *Geophysical Research Letters*, **35**(16).

Obara, Kazushige. 2002. Nonvolcanic deep tremor associated with subduction in southwest Japan. *Science*, **296**(5573), 1679–1681.

Obermann, Anne, Planès, Thomas, Larose, Eric, Sens-Schönfelder, Christoph, & Campillo, Michel. 2013. Depth sensitivity of seismic coda waves to velocity perturbations in an elastic heterogeneous medium. *Geophysical Journal International*, **194**(1), 372–382.

Obermann, Anne, Kraft, Toni, Larose, Eric, & Wiemer, Stefan. 2015. Potential of ambient seismic noise techniques to monitor the St. Gallen geothermal site (Switzerland). *Journal of Geophysical Research: Solid Earth*, **120**(6), 4301–4316.

Obermann, Anne, Planès, Thomas, Hadziioannou, Céline, & Campillo, Michel. 2016. Lapse-time-dependent coda-wave depth sensitivity to local velocity perturbations in 3-D heterogeneous elastic media. *Geophysical Journal International*, **207**(1), 59–66.

Obermann, Anne, Planès, Thomas, Larose, Eric, & Campillo, Michel. 2019. 4-D Imaging of Subsurface Changes with Coda Waves: Numerical Studies of 3-D Combined Sensitivity Kernels and Applications to the M_w7.9, 2008 Wenchuan Earthquake. *Pure and Applied Geophysics*, **176**(3), 1243–1254.

Pacheco, Carlos, & Snieder, Roel. 2005. Time-lapse travel time change of multiply scattered acoustic waves. *The Journal of the Acoustical Society of America*, **118**(3), 1300–1310.

Pan, Yudi, Xia, Jianghai, Xu, Yixian, Xu, Zongbo, Cheng, Feng, Xu, Hongrui, & Gao, Lingli. 2016. Delineating shallow S-wave velocity structure using multiple

ambient-noise surface-wave methods: An example from Western Junggar, China. *Bulletin of the Seismological Society of America*, **106**(2), 327–336.

Pan, Yudi, Gao, Lingli, & Shigapov, Renat. 2020. Multi-objective waveform inversion of shallow seismic wavefields. *Geophysical Journal International*, **220**(3), 1619–1631.

Park, Choon B, & Miller, Richard D. 2008. Roadside passive multichannel analysis of surface waves (MASW). *Journal of Environmental & Engineering Geophysics*, **13**(1), 1–11.

Park, Choon B, Miller, Richard D, & Xia, Jianghai. 1999. Multichannel analysis of surface waves. *Geophysics*, **64**(3), 800–808.

Park, Choon Byong, Miller, Richard D, Xia, Jianghai, *et al.* 1998. Imaging dispersion curves of surface waves on multi-channel record. *Pages 1377–1380 of: SEG Expanded Abstracts*, vol. 17.

Rayleigh, Lord. 1885. On waves propagated along the plane surface of an elastic solid. *Proceedings of the London Mathematical Society*, **1**(1), 4–11.

Rhie, Junkee, & Romanowicz, Barbara. 2006. A study of the relation between ocean storms and the Earth's hum. *Geochemistry, Geophysics, Geosystems*, **7**(10).

Richwalski, Sandra M, Picozzi, Matteo, Parolai, Stefano, Milkereit, Claus, Baliva, Francesco, Albarello, Dario, Roy-Chowdhury, Kabir, van der Meer, Henk, & Zschau, Jochen. 2007. Rayleigh wave dispersion curves from seismological and engineering-geotechnical methods: A comparison at the Bornheim test site (Germany). *Journal of Geophysics and Engineering*, **4**(4), 349.

Rost, Sebastian, & Thomas, Christine. 2002. Array seismology: Methods and applications. *Reviews of geophysics*, **40**(3).

Roux, Philippe, Sabra, Karim G, Kuperman, William A, & Roux, Andre. 2005. Ambient noise cross correlation in free space: Theoretical approach. *The Journal of the Acoustical Society of America*, **117**(1), 79–84.

Roux, Philippe, Bindi, Dino, Boxberger, Tobias, Colombi, Andrea, Cotton, Fabrice, Douste-Bacque, Isabelle, Garambois, Stéphane, Gueguen, Philippe, Hillers, Gregor, Hollis, Dan, *et al.* 2018. Toward seismic metamaterials: The METAFORET project. *Seismological Research Letters*, **89**(2A), 582–593.

Sager, Korbinian, Ermert, Laura, Boehm, Christian, & Fichtner, Andreas. 2018. Towards Full Waveform Ambient Noise Inversion. *Geophysical Journal International*, **212**(1), 566–590.

Sato, Haruo, Fehler, Michael C, & Maeda, Takuto. 2012. *Seismic wave propagation and scattering in the heterogeneous Earth*. Vol. 496. Springer.

Scott, James B, Clark, Matthew, Rennie, Thomas, Pancha, Aasha, Park, Hyunmee, & Louie, John N. 2004. A shallow shear-wave velocity transect across the Reno, Nevada, area basin. *Bulletin of the Seismological Society of America*, **94**(6), 2222–2228.

Sen, Mrinal K, & Stoffa, Paul L. 1991. Nonlinear one-dimensional seismic waveform inversion using simulated annealing. *Geophysics*, **56**(10), 1624–1638.

Sens-Schönfelder, Christoph, & Wegler, U. 2006. Passive image interferometry and

seasonal variations of seismic velocities at Merapi Volcano, Indonesia. *Geophysical research letters*, **33**(21).

Seydoux, Léonard, de Rosny, Julien, & Shapiro, Nikolai M. 2017. Pre-processing ambient noise cross-correlations with equalizing the covariance matrix eigenspectrum. *Geophysical Journal International*, **210**(3), 1432–1449.

Shapiro, Nikolai M, Campillo, Michel, Stehly, Laurent, & Ritzwoller, Michael H. 2005. High-resolution surface-wave tomography from ambient seismic noise. *Science*, **307**, 1615–1618.

Shapiro, Nikolai M, Ritzwoller, MH, & Bensen, GD. 2006. Source location of the 26 sec microseism from cross-correlations of ambient seismic noise. *Geophysical Research Letters*, **33**(18).

Shen, Chao, Wang, Ao, Wang, Limin, Xu, Zongbo, & Cheng, Feng. 2015. Resolution equivalence of dispersion-imaging methods for noise-free high-frequency surface-wave data. *Journal of Applied Geophysics*, **122**, 167–171.

Shen, Weisen, Wiens, Douglas A, Anandakrishnan, Sridhar, Aster, Richard C, Gerstoft, Peter, Bromirski, Peter D, Hansen, Samantha E, Dalziel, Ian WD, Heeszel, David S, Huerta, Audrey D, *et al.* 2018. The crust and upper mantle structure of central and West Antarctica from Bayesian inversion of Rayleigh wave and receiver functions. *Journal of Geophysical Research: Solid Earth*, **123**(9), 7824–7849.

Snieder, Roel. 1986a. 3-D linearized scattering of surface waves and a formalism for surface wave holography. *Geophysical Journal International*, **84**(3), 581–605.

Snieder, Roel. 1986b. The influence of topography on the propagation and scattering of surface waves. *Physics of the earth and planetary interiors*, **44**(3), 226–241.

Snieder, Roel. 2002. Coda wave interferometry and the equilibration of energy in elastic media. *Physical review E*, **66**(4), 046615.

Snieder, Roel. 2004. Extracting the Green's function from the correlation of coda waves: A derivation based on stationary phase. *Physical Review E*, **69**(4), 046610.

Snieder, Roel. 2006. The theory of coda wave interferometry. *Pure and Applied geophysics*, **163**(2-3), 455–473.

Snieder, Roel, & Fleury, Clement. 2010. Cancellation of spurious arrivals in Green's function retrieval of multiple scattered waves. *The Journal of the Acoustical Society of America*, **128**(4), 1598–1605.

Snieder, Roel, Grêt, Alexandre, Douma, Huub, & Scales, John. 2002. Coda wave interferometry for estimating nonlinear behavior in seismic velocity. *Science*, **295**(5563), 2253–2255.

Snieder, Roel, Wapenaar, Kees, & Larner, Ken. 2006. Spurious multiples in seismic interferometry of primaries. *Geophysics*, **71**(4), SI111.

Snieder, Roel, Van Wijk, Kasper, Haney, Matt, & Calvert, Rodney. 2008. Cancellation of spurious arrivals in Green's function extraction and the generalized optical theorem. *Physical Review E - Statistical, Nonlinear, and Soft Matter Physics*, **78**(3), 1–8.

Song, Yi-Yung, Castagna, John P, Black, Ross A, & Knapp, Ralph W. 1989. Sensitivity of near-surface shear-wave velocity determination from Rayleigh and Love waves. *SEG, 59th Annual Meeting, Dallas, Texas*, 509–512.

Stankiewicz, Jacek, Ryberg, Trond, Haberland, Christian, Natawidjaja, Danny, *et al.* 2010. Lake Toba volcano magma chamber imaged by ambient seismic noise tomography. *Geophysical Research Letters*, **37**(17).

Stehly, L, Campillo, Michel, & Shapiro, NM. 2006. A study of the seismic noise from its long-range correlation properties. *Journal of Geophysical Research: Solid Earth*, **111**(B10).

Stehly, Laurent, & Boué, Pierre. 2017. On the interpretation of the amplitude decay of noise correlations computed along a line of receivers. *Geophysical Journal International*, **209**(1), 358–372.

Stehly, Laurent, Campillo, Michel, Froment, Brnice, & Weaver, Richard L. 2008. Reconstructing Green's function by correlation of the coda of the correlation (C3) of ambient seismic noise. *Journal of Geophysical Research: Solid Earth*, **113**(B11).

Stehly, Laurent, Cupillard, Paul, & Romanowicz, Barbara. 2011. Towards improving ambient noise tomography using simultaneously curvelet denoising filters and SEM simulations of seismic ambient noise. *Comptes Rendus - Geoscience*, **343**(8-9), 591–599.

Stehly, Lolo, Fry, B., Campillo, M., Shapiro, N. M., Guilbert, J., Boschi, L., & Giardini, D. 2009. Tomography of the Alpine region from observations of seismic ambient noise. *Geophysical Journal International*, **178**(1), 338–350.

Strobbia, Claudio, & Cassiani, Giorgio. 2011. Refraction microtremors: Data analysis and diagnostics of key hypotheses. *Geophysics*, **76**(3), MA11–MA20.

Takano, Tomoya, Brenguier, Florent, Campillo, Michel, Peltier, Aline, & Nishimura, Takeshi. 2019. Noise-based passive ballistic wave seismic monitoring on an active volcano. *Geophysical Journal International*, **220**(1), 501–507.

Takemura, Shunsuke, Furumura, Takashi, & Maeda, Takuto. 2015. Scattering of high-frequency seismic waves caused by irregular surface topography and small-scale velocity inhomogeneity. *Geophysical Journal International*, **201**(1), 459–474.

Tape, Carl, Liu, Qinya, & Tromp, Jeroen. 2007. Finite-frequency tomography using adjoint methods–Methodology and examples using membrane surface waves. *Geophysical Journal International*, **168**(3), 1105–1129.

Tarantola, Albert. 2005. *Inverse problem theory and methods for model parameter estimation*. Vol. 89. siam.

Thorson, Jeffrey R, & Claerbout, Jon F. 1985. Velocity-stack and slant-stack stochastic inversion. *Geophysics*, **50**(12), 2727–2741.

Tian, Ye, & Ritzwoller, Michael H. 2015. Directionality of ambient noise on the Juan de Fuca plate: Implications for source locations of the primary and secondary microseisms. *Geophysical Journal International*, **201**(1), 429–443.

Traer, James, & Gerstoft, Peter. 2014. A unified theory of microseisms and hum. *Journal of Geophysical Research: Solid Earth*, **119**(4), 3317–3339.

Tromp, Jeroen, Tape, Carl, & Liu, Qinya. 2005. Seismic tomography, adjoint methods, time reversal and banana-doughnut kernels. *Geophysical Journal International*, **160**(1), 195–216.

Tromp, Jeroen, Luo, Yang, Hanasoge, Shravan, & Peter, Daniel. 2010. Noise cross-correlation sensitivity kernels. *Geophysical Journal International*, **183**(2), 791–819.

Tsai, Victor C, & Moschetti, Morgan P. 2010. An explicit relationship between time-domain noise correlation and spatial autocorrelation (SPAC) results. *Geophysical Journal International*, **182**(1), 454–460.

Tsai, Victor C, Minchew, Brent, Lamb, Michael P, & Ampuero, Jean-Paul. 2012. A physical model for seismic noise generation from sediment transport in rivers. *Geophysical Research Letters*, **39**(2).

Turner, Greg. 1990. Aliasing in the tau-p transform and the removal of spatially aliased coherent noise. *Geophysics*, **55**(11), 1496–1503.

Umlauft, J, & Korn, M. 2019. 3-D fluid channel location from noise tremors using matched field processing. *Geophysical Journal International*, **219**(3), 1550–1561.

Valentine, Andrew P, & Woodhouse, John H. 2010. Reducing errors in seismic tomography: combined inversion for sources and structure. *Geophysical Journal International*, **180**(2), 847–857.

van Driel, M., Krischer, L., Stähler, S. C., Hosseini, K., & Nissen-Meyer, T. 2015. Instaseis: instant global seismograms based on a broadband waveform database. *Solid Earth*, **6**(2), 701–717.

van Wijk, Kasper, Mikesell, T Dylan, Schulte-Pelkum, Vera, & Stachnik, Josh. 2011. Estimating the Rayleigh-wave impulse response between seismic stations with the cross terms of the Green tensor. *Geophysical Research Letters*, **38**(16).

Vassallo, Maurizio, Festa, Gaetano, Bobbio, Antonella, & Serra, Marcello. 2016. Low shear velocity in a normal fault system imaged by ambient noise cross correlation: The case of the Irpinia fault zone, Southern Italy. *Journal of Geophysical Research: Solid Earth*, **121**(6), 4290–4305.

Virieux, Jean, & Operto, Stéphane. 2009. An overview of full-waveform inversion in exploration geophysics. *Geophysics*, **74**(6), WCC1–WCC26.

Wang, Limin, Xu, Yixian, & Luo, Yinhe. 2015. Numerical Investigation of 3D multichannel analysis of surface wave method. *Journal of Applied Geophysics*, **119**, 156–169.

Wapenaar, Kees, & Fokkema, Jacob. 2006. Green's function representations for seismic interferometry. *Geophysics*, **71**(4), SI33–SI46.

Wapenaar, Kees, Ruigrok, Elmer, Van Der Neut, Joost, & Draganov, Deyan. 2011. Improved surface-wave retrieval from ambient seismic noise by multi-dimensional deconvolution. *Geophysical Research Letters*, **38**(1), 1–5.

Weaver, Richard L, & Lobkis, Oleg I. 2001. Ultrasonics without a source: Thermal fluctuation correlations at MHz frequencies. *Physical Review Letters*, **87**(13), 134301.

Weaver, Richard L., & Lobkis, Oleg I. 2006. Diffuse fields in ultrasonics and seismology. *Geophysics*, **71**(4), SI5–SI9.

Wu, R-S, & Aki, Keiiti. 1985. Scattering characteristics of elastic waves by an elastic heterogeneity. *Geophysics*, **50**(4), 582–595.

Xia, Jianghai. 2014. Estimation of near-surface shear-wave velocities and quality factors using multichannel analysis of surface-wave methods. *Journal of Applied Geophysics*, **103**, 140–151.

Xia, Jianghai, Miller, Richard D, Park, Choon B, & Tian, Gang. 2002. Determining Q of near-surface materials from Rayleigh waves. *Journal of Applied Geophysics*, **51**(2-4), 121–129.

Xia, Jianghai, Miller, Richard D, Park, Choon B, & Tian, Gang. 2003. Inversion of high frequency surface waves with fundamental and higher modes. *Journal of Applied Geophysics*, **52**(1), 45–57.

Xia, Jianghai, Xu, Yixian, & Miller, Richard D. 2007. Generating an image of dispersive energy by frequency decomposition and slant stacking. *Pure and Applied Geophysics*, **164**(5), 941–956.

Xu, Yixian, Zhang, Baolong, Luo, Yinhe, & Xia, Jianghai. 2013. Surface-wave observations after integrating active and passive source data. *The Leading Edge*, **32**(6), 634–637.

Xu, Zongbo, & Mikesell, T Dylan. 2017. On the reliability of direct Rayleigh-wave estimation from multicomponent cross-correlations. *Geophysical Journal International*, **210**(3), 1388–1393.

Xu, Zongbo, Xia, Jianghai, Luo, Yinhe, Cheng, Feng, & Pan, Yudi. 2016. Potential

misidentification of Love-wave phase velocity based on three-component ambient seismic noise. *Pure and Applied Geophysics*, **173**(4), 1115–1124.

Xu, Zongbo, Dylan Mikesell, T, Xia, Jianghai, & Cheng, Feng. 2017. A comprehensive comparison between the refraction microtremor and seismic interferometry methods for phase-velocity estimation. *Geophysics*, **82**(6), EN99–EN108.

Xu, Zongbo, Mikesell, T Dylan, Gribler, Gabriel, & Mordret, Aurélien. 2019. Rayleigh-wave multicomponent cross-correlation-based source strength distribution inversion. Part 1: Theory and numerical examples. *Geophysical Journal International*, **218**(3), 1761–1780.

Yamanaka, Hiroaki, Dravinski, Marijan, & Kagami, Hiroshi. 1993. Continuous measurements of microtremors on sediments and basement in Los Angeles, California. *Bulletin of the Seismological Society of America*, **83**(5), 1595–1609.

Yang, Yingjie, & Ritzwoller, Michael H. 2008. Characteristics of ambient seismic noise as a source for surface wave tomography. *Geochemistry Geophysics Geosystems*, **9**(2), 1256–1256.

Yao, Huajian, & Van Der Hilst, Robert D. 2009. Analysis of ambient noise energy distribution and phase velocity bias in ambient noise tomography, with application to SE Tibet. *Geophysical Journal International*, **179**(2), 1113–1132.

Yao, Huajian, Van Der Hilst, Robert D., & de Hoop, Maarten V. 2006. Surface wave array tomography in SE Tibet from ambient seismic noise and two-station analysis - I. Phase velocity maps. *Geophysical Journal International*, **173**(1), 732–744.

Yilmaz, Öz. 2001. *Seismic data analysis: Processing, inversion, and interpretation of seismic data*. Society of exploration geophysicists.

Zeng, Xiangfang, & Ni, Sidao. 2010. A persistent localized microseismic source near the Kyushu Island, Japan. *Geophysical Research Letters*, **37**(24).

Zeng, Yuehua. 2006. Scattered surface wave energy in the seismic coda. *pure and applied geophysics*, **163**(2-3), 533–548.

Appendices

APPENDIX A:

A.1 $f-k$ analysis with a linear array

The phase-shift method (Park *et al.*, 1998) and the τ-p transform (McMechan & Yedlin, 1981) are related to frequency-wave number (f-k) analysis (e.g. Rost & Thomas, 2002), which for two-dimensional arrays can be used to determine back azimuth and phase velocity of incident plane waves. The array response function in f-k analysis can be written as

$$|A(\mathbf{k}-\mathbf{k}_0)|^2 = \left| \frac{1}{N} \sum_{n=1}^{N} e^{j(\mathbf{k}-\mathbf{k}_0)\cdot\mathbf{r}_n} \right|^2 \tag{A.1}$$

where $\mathbf{k}$ is the test wave vector, $\mathbf{k}_0$ is the observed wave vector, $\mathbf{r}_n$ is the location vector of the n^{th} sensor and N is the number of sensors (Rost & Thomas, 2002). For a linear array, if one assumes surface waves propagate along the array in the x-direciton then $\mathbf{k}\cdot\mathbf{r}_n = kx$, where $k = 2\pi fp$. Thus we can write Equation A.1 as

$$|A(f(p-p_0))|^2 = \left| \frac{1}{N} \sum_{x_{min}}^{x_{max}} e^{j2\pi f(p-p_0)x} \right|^2 = \left| \frac{1}{N} \sum_{x_{min}}^{x_{max}} d(x,f) e^{j2\pi fpx} \right|^2 \tag{A.2}$$

where $d(x,f) = e^{-j2\pi fp_0x}$. Equation A.2 is identical to Equation 2.6, and therefore, f-k analysis for a linear array is the phase-shift method or the τ-p transform under the assumption that waves propagate along the array.

APPENDIX B:

B.1 Traveltime adjoint sources

We compute the perturbation of the traveltime misfit function (Equation 4.2) as:

$$\delta\chi = (T_{syn} - T_{obs})\delta(T_{syn} - T_{obs}) = (T_{syn} - T_{obs})\delta T, \tag{B.1}$$

where $T = T_{syn} - T_{obs}$ represents the travel-time difference between synthetic and observed waveforms. Fichtner *et al.* (2017) derived an expression for δT. We present the main steps here. The travel-time difference, T, is measured by crosscorrelation (Figure B.1) and is determined as the crosscorrelation maximum (e.g. Luo & Schuster, 1991; Dahlen *et al.*, 2000):

$$T = max\left[\int C_{mn}(r_A, r_B, \tau)[w(\tau - t)C^o_{mn}(r_A, r_B, \tau - t)]d\tau\right], \tag{B.2}$$

where $w(t)$ is a time window and C^o_{mn} is the observed data. The time derivative of the max function argument at $t = T$ is zero. Thus we can write

$$\int C_{mn}(r_A, r_B, \tau)\frac{d}{dt}[w(\tau - t)C^o_{mn}(r_A, r_B, \tau - t)]_{t=T}d\tau = 0. \tag{B.3}$$

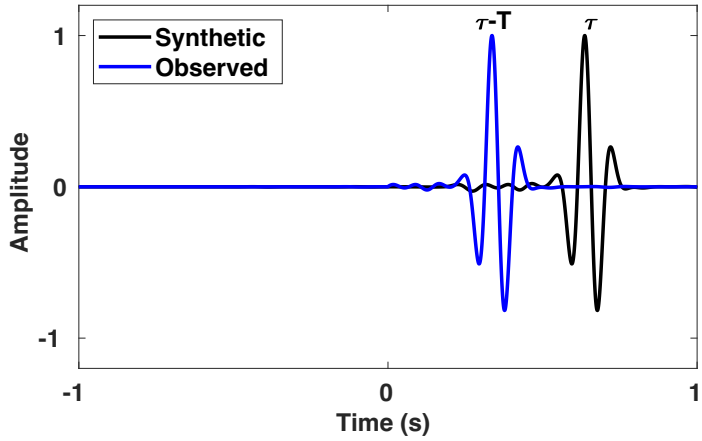

Figure B.1: An illustration of the traveltime difference, T, between synthetic and observed crosscorrelations.

We then write the traveltime perturbation to T and C_{mn} as:

$$\int \delta C_{mn}(r_A, r_B, \tau) \frac{d}{dt}[w(\tau - t) C^o_{mn}(r_A, r_B, \tau - t)]_{t=T} d\tau$$
$$+ \int C_{mn}(r_A, r_B, \tau) \frac{d^2}{dt^2}[w(\tau - t) C^o_{mn}(r_A, r_B, \tau - t)]_{t=T} \delta T d\tau = 0, \tag{B.4}$$
$$\rightarrow \delta T = - \frac{\int \delta C_{mn}(r_A, r_B, \tau) \frac{d}{dt}[w(\tau - t) C^o_{mn}(r_A, r_B, \tau - t)]_{t=T} d\tau}{\int C_{mn}(r_A, r_B, \tau) \frac{d^2}{dt^2}[w(\tau - t) C^o_{mn}(r_A, r_B, \tau - t)]_{t=T} d\tau}. \tag{B.5}$$

One usually assumes that the observed waveform is a time-shifted copy of the synthetic waveform, $[w(\tau - t) C^o_{mn}(r_A, r_B, \tau - t)]_{t=T} = w(\tau) C_{mn}(r_A, r_B, \tau)$. In this case, we can rewrite the integrand of Equation B.5 as

$$\frac{d}{dt}[w(\tau - t) C^o_{mn}(r_A, r_B, \tau - t)]_{t=T} = -\frac{d}{d\tau}[w(\tau) C_{mn}(r_A, r_B, \tau)],$$
$$\textit{and } \frac{d^2}{dt^2}[w(\tau - t) C^o_{mn}(r_A, r_B, \tau - t)]_{t=T} = \frac{d^2}{d\tau^2}[w(\tau) C_{mn}(r_A, r_B, \tau)].$$

Thus Equation B.5 becomes:

$$\delta T = \frac{\int \delta C_{mn}(r_A, r_B, \tau) \frac{d}{d\tau}[w(\tau) C_{mn}(r_A, r_B, \tau)] d\tau}{\int C_{mn}(r_A, r_B, \tau) \frac{d^2}{d\tau^2}[w(\tau) C_{mn}(r_A, r_B, \tau)] d\tau}, \tag{B.6}$$

or in the frequency domain on a frequency band, $[\omega 1, \omega 2]$:

$$\delta T = i \frac{\int_{\omega 1}^{\omega 2} \omega \delta C_{mn}(r_A, r_B, \omega)[w(\omega) * C_{mn}(r_A, r_B, \omega)]^* d\omega}{\int_{\omega 1}^{\omega 2} \omega^2 C_{mn}(r_A, r_B, \omega)[w(\omega) * C_{mn}(r_A, r_B, \omega)]^* d\omega}. \tag{B.7}$$

Finally, we write Equation B.7 with an adjoint source (f) for a single frequency (ω)

$$\delta T = \int_{\omega 1}^{\omega 2} f(\omega) \delta C_{mn}(r_A, r_B, \omega) d\omega. \tag{B.8}$$

where

$$f(\omega) = i \frac{\omega [w(\omega) * C_{mn}(r_A, r_B, \omega)]^*}{\int_{\omega 1}^{\omega 2} \omega^2 C_{mn}(r_A, r_B, \omega)[w(\omega) * C_{mn}(r_A, r_B, \omega)]^* d\omega}. \tag{B.9}$$

If we assume that we know the Green's functions (Equation 4.4), we can write

$$\delta T = \int_{\omega 1}^{\omega 2} \int_V G_{mp}(r_A, r_s, \omega) G^*_{np}(r_B, r_s, \omega) f(\omega) \delta S_p(r_s, \omega) dr_s d\omega, \tag{B.10}$$

and we can write the source kernel for δT as

$$K_{mn}(\omega, r_s) = G_{mp}(r_A, r_s, \omega) G^*_{np}(r_B, r_s, \omega) f(\omega). \tag{B.11}$$

Equation B.11 does not require observed data. Thus we use Equation B.11 in Section 4.4 to analyze the traveltime source kernels. This formulation assumes that the observed waveform is close to the synthetic waveform. As the assumption is not valid in our synthetic data examples, we do not adopt Equation B.11 in the actual inversion

algorithm.

In the traveltime inversions (Section 4 and 5), we combine the kernel equation B.11 with Equation B.1 as:

$$\begin{aligned} K^o_{mn}(\omega, r_s) &= (T_{syn} - T_{obs}) K_{mn}(\omega, r_s) \\ &= (T_{syn} - T_{obs}) G_{mp}(r_A, r_s, \omega) G^*_{np}(r_B, r_s, \omega) f(\omega). \end{aligned} \tag{B.12}$$

B.2 Waveform adjoint sources

We write the perturbation of the waveform misfit function (Equation 4.1) following Fichtner *et al.* (2017):

$$\delta\chi = \int [w^2(t)(C_{mn}(r_A, r_B, t) - C^o_{mn}(r_A, r_B, t))] \delta C_{mn}(r_A, r_B, t) dt \tag{B.13}$$

$$= \frac{1}{2\pi} \int [w(\omega) * w(\omega) * (C_{mn}(r_A, r_B, \omega) - C^o_{mn}(r_A, r_B, \omega))]^* \delta C_{mn}(r_A, r_B, \omega) d\omega, \tag{B.14}$$

where $\delta C^o_{mn}(r_A, r_B, \omega) = 0$. The corresponding adjoint source is defined as

$$f(\omega) = \frac{1}{2\pi} [w(\omega) * w(\omega) * (C_{mn}(r_A, r_B, \omega) - C^o_{mn}(r_A, r_B, \omega))]^*. \tag{B.15}$$

In Section 4.4 where there is no observed crosscorrelation, we write the adjoint source as (Fichtner *et al.*, 2017)

$$f(\omega) = \frac{1}{2\pi} [w(\omega) * w(\omega) * C_{mn}(r_A, r_B, \omega)]^*. \tag{B.16}$$

B.3 The link among waveform source inversion, matched-field processing and reverse-time migration

We can relate the waveform source inversion with the matched-field processing. If we assume that there are no seismic sources in the initial source distribution model, $C_{mn}(r_A, r_B, \omega)$ will be equal to zero. We can write the waveform source equation by combining Equation 4.9 and B.14 as

$$\delta\chi = -\frac{1}{2\pi}\int\int_V [C^o_{mn}(r_A, r_B, \omega)]^* G_{mp}(r_A, r_s, \omega) G^*_{np}(r_B, r_s, \omega)\delta S_p(r_s, \omega) dr_s d\omega, \tag{B.17}$$

where we neglect the time window term $w(\omega)$. We then rewrite the observed cross-correlation, $C^o_{mn}(r_A, r_B, \omega) = U^o_m(r_A, \omega)[U^o_n(r_B, \omega)]^*$, where $U^o_m(r_A, \omega)$ is the observed m-direction component seismic recording at r_A. The crosscorrelation at a single frequency is a component of the cross-spectral density matrix in matched-field processing (e.g. Cros *et al.*, 2011). We now write the source kernel in Equation B.17 explicitly as

$$K = -[U^o_m(r_A, \omega)]^* U^o_n(r_B, \omega) G_{mp}(r_A, r_s, \omega) G^*_{np}(r_B, r_s, \omega), \tag{B.18}$$

and rewrite Equation B.17 as

$$\delta\chi = -\frac{1}{2\pi}\int\int_V K\delta S_p(r_s, \omega) dr_s d\omega. \tag{B.19}$$

In practice, we stack the kernel among all sensor pairs and the stacked kernel

reads as

$$K = -\sum_{r_A r_B} [U_m^o(r_A, \omega)]^* U_n^o(r_B, \omega) G_{mp}(r_A, r_s, \omega) G_{np}^*(r_B, r_s, \omega). \tag{B.20}$$

We can recognize the stacked kernel is a conjugation of the linear (Bartlett) processor in matched-field processing (e.g. Cros *et al.*, 2011; Corciulo *et al.*, 2012) without autocorrelation terms:

$$\sum_{r_A r_B} G_{zz}^*(r_A, r_s, \omega) U_z^o(r_A, \omega) [U_z^o(r_B, \omega)]^* G_{zz}(r_B, r_s, \omega), \tag{B.21}$$

where people usually use vertical component (Z) data. Therefore the matched-field processing results are similar to the stacked waveform source kernels where the initial source strengths are zero. We apply the matched-field processing to the ZZ data in Section 4.5 and estimate the seismic source strengths shown in Figure B.2. We calculate the Rayleigh-wave phase velocity for the halfspace model (Table 4.1 True), 1391 m/s (Rayleigh, 1885). We use Equation 4.23 as the Green's function in MFP (Equation B.21) and estimate source distributions for each example in Section 4.5 (Figure B.2a, Figure B.2b and Figure B.2c). We observe that high source strength values concentrate near the sensors and the true source locations. This singularity at the sensors is due to the amplitude term in the Green's function, $\sqrt{\frac{1}{8\pi\omega r/c}}$. If we also only use the phase part of the Green's function, the singularities disappear (Figure B.2d, Figure B.2e and Figure B.2f). The singularity also exists in the waveform inversion and that is why people adopt a taper near sources and receivers or smooth the gradient (e.g. Groos *et al.*, 2017).

We can also relate this kernel (Equation B.18) to reverse-time migration. If we

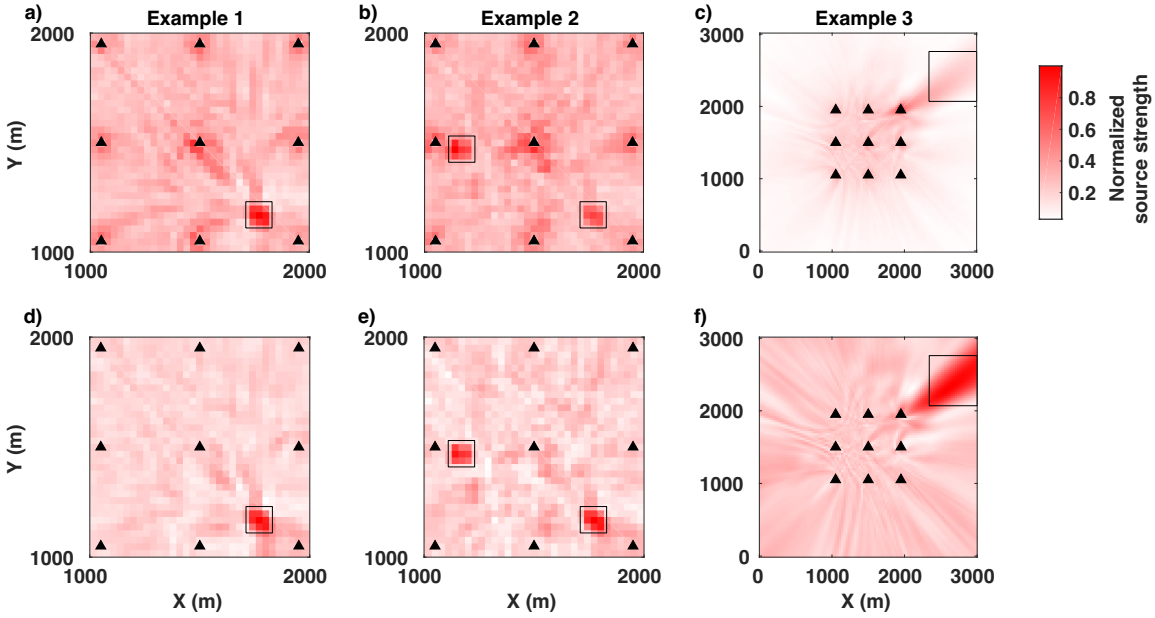

Figure B.2: Matched-field processing (MFP) results from the ZZ data in Section 4.5. We use the full Rayleigh-wave Green's function (Equation 4.23) in MFP (a, b and c), and we only use the phase part of the Green's function (Equation 4.23) in MFP (d, e and f). The black empty squares indicate the shapes and locations of the true sources.

assume that $C^o_{mn}(r_A, r_B, \omega)$ is due to a microseismic or secondary source, r', we can write the kernel as

$$K = [C^o_{mn}(r_A, r_B, \omega)]^* G_{mp}(r_A, r_s, \omega) G^*_{np}(r_B, r_s, \omega) \tag{B.22}$$

$$= [U^o_m(r_A, r', \omega)]^* U^o_n(r_B, r', \omega) G_{mp}(r_A, r_s, \omega) G^*_{np}(r_B, r_s, \omega) \tag{B.23}$$

$$= [U_m(r_A, r', \omega) G^*_{mp}(r_A, r_s, \omega)]^* [U_n(r_B, r', \omega) G^*_{np}(r_B, r_s, \omega)]. \tag{B.24}$$

We recognize that the kernel, Equation B.24, is the microseismic imaging condition (e.g. Artman *et al.*, 2010, Equation 4) in the frequency domain. Therefore the imaging condition in reverse-time migration is similar to the waveform source kernel with zero initial source strength.

B.4 Fourier transform convention

We use the following Fourier transform convention

$$U(\omega) = \int_{-\infty}^{\infty} U(t) e^{-i\omega t} dt, \tag{B.25}$$

as opposed to

$$U(\omega) = \int_{-\infty}^{\infty} U(t) e^{i\omega t} dt \tag{B.26}$$

(e.g. Aki & Richards, 2002; Haney & Nakahara, 2014).

APPENDIX C:

C.1 Source kernels

We compare the ZZ and RR source sensitivity kernels for two different interstation distances, 20 m and 100 m. Although some previous studies discussed the interstation distances (e.g. Bensen *et al.*, 2007; Luo *et al.*, 2015), these studies are for ANT not for source estimation. Furthermore, these studies did not consider the source sensitivity kernels. Thus it is still necessary to discuss the effect of different interstation distance on the source sensitivity kernels.

We set the observed data be zeros (Equation 5.10) and focus on the synthetic waveform energy in the time window -2 to 2 s. We examine two initial source cases: (i) an out-of-line source (small black box in upper right of Figures C.1a, C.1c, C.1e, C.1g) and (ii) an in-line source (small black box on center right of Figures C.1b, C.1d, C.1f, C.1h). From these initial distributions, we calculate synthetic crosscorrelations using the forward model (Equation 5.11). The 20 m interstation distance synthetic C_{ZZ} waveforms are similar for the two source cases (Figure C.2a), while the 20 m C_{RR} waveforms have significantly different amplitudes (Figure C.2b). For the 100 m sensor pair, the C_{ZZ} waveforms are quite different for the two source cases (Figure C.2c), as are the C_{RR} waveforms (Figure C.2d) indicating that these correlations are more sensitive to the source distribution than the small station spacing correlations.

From the waveforms, we can calculate source sensitivity kernels (Equation 5.13).

The sensitivity kernels indicate how source strength changes affect the synthetic waveform energy. We observe that the first Fresnel zone in the source sensitivity kernels for the 20 m sensor pair (Figures C.1a, C.1b, C.1e and C.1f) is much larger than for the 100 m sensor pair (Figures C.1c, C.1d, C.1g and C.1h). For the small-distance sensor pair, the ZZ sensitivity kernels are similar when the initial source location changes (Figures C.1a and C.1b), while the RR sensitivity kernels change more dramatically with initial source distribution (Figures C.1e and C.1f); the two ZZ sensitivity values in the source locations are the same order (a factor of 2 different) while the in-line RR sensitivity values are almost an order of magnitude different (a factor of 10) than the out-of-line source. This variation in sensitivity is because of the azimuthal effect of the R component (e.g. Haney *et al.*, 2012; Xu & Mikesell, 2017; Xu *et al.*, 2019). Thus, incorporating multicomponent crosscorrelations into the full-waveform inversion provides additional sensitivity that helps resolve sources, even when the station spacing is small.

C.2 Calculating Rayleigh-wave phase velocities

We estimate the phase velocity by combining classic ambient seismic noise processing (e.g. Bensen *et al.*, 2007) and surface-wave velocity analysis (e.g. McMechan & Yedlin, 1981; Park *et al.*, 1998). In order to calculate accurate surface-wave phase velocities, one needs to mitigate the effects of an anisotropic source distribution by using long recordings and/or time-/frequency-domain normalization (e.g. Yang & Ritzwoller, 2008). Here we use two days of geophone recordings (22 and 23 November 2016). We divide the two-day data into 60 s sections and remove the mean and linear trend from each section. We then apply one-bit amplitude normalization to the sections, crosscorrelate, and linearly stack. Note that we focus on accurate Rayleigh-wave

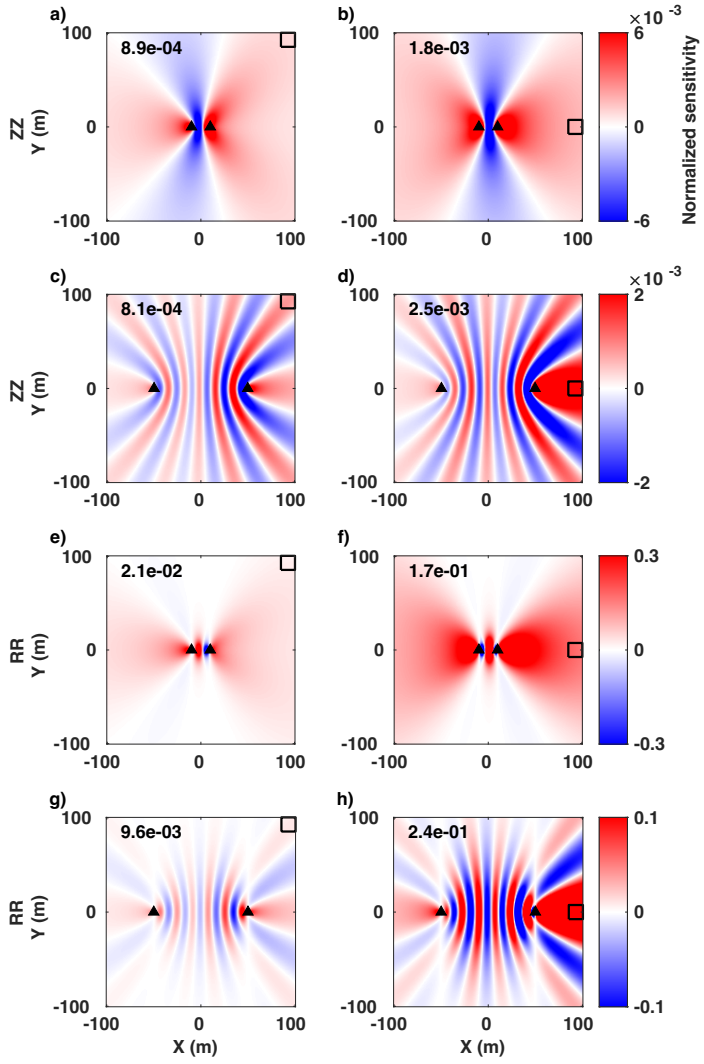

Figure C.1: ZZ and RR waveform energy source sensitivity kernels for out-of-line (left column) and in-line (right column) initial source models. The two sensors are separated by 20 m (a, b, e, and f) and 100 m (c, d, g, and h). All the sensitivity kernels are normalized by the absolute maximum value in (e). The black triangles are sensors. The black empty squares indicate the source locations. In each subplot, the number in the top left corner indicates the sensitivity value in the center of the square. We calculate the kernels from 4.5 to 6 Hz and use the same Green's functions and S_Z^0 (S_R^0) as in the paper.

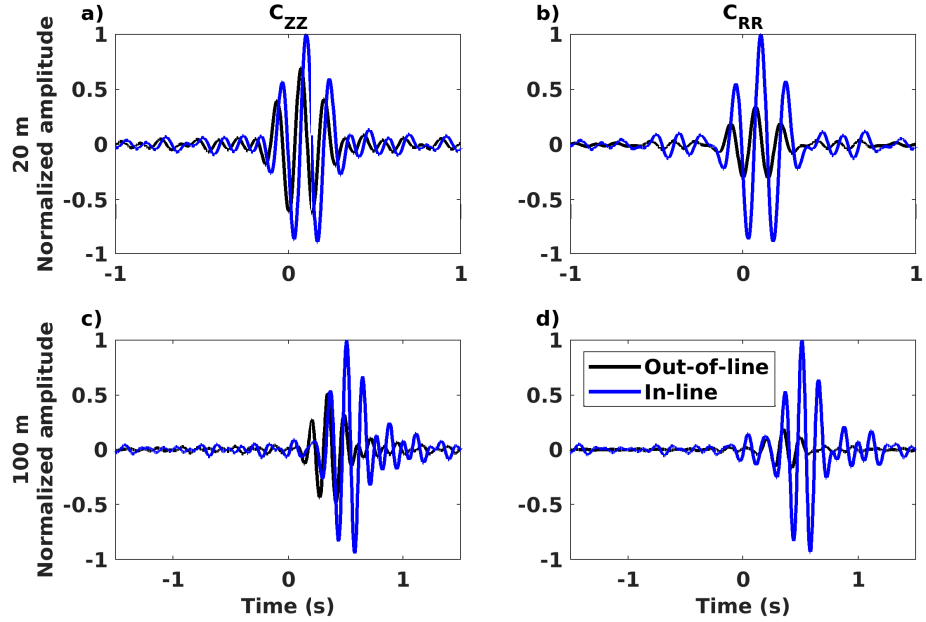

Figure C.2: Comparison of synthetic C_{ZZ} and C_{RR} waveforms between the in-line and out-of-line source cases. The top row is for the 20 m interstation distance sensor pair; the bottom row is for the 100 m interstation distance sensor pair. Each waveform is band-pass filtered between 4.5 and 9 Hz and then normalized by the maximum amplitude of the in-line crosscorrelations so that relative amplitudes are preserved.

phase velocities, not waveforms. Thus we use the one-bit time-domain normalization procedure.

We stack all of the crosscorrelations into 1 m offset bins to generate a virtual shot gather (Figures C.3a and C.3b). We sum the causal and acausal parts of the gather and then create a dispersion image (Figures C.3c and C.3d) by applying the phase-shift velocity transform (Park *et al.*, 1998). We observe a clear Rayleigh-wave dispersion signal in the C_{ZZ} waveforms (Figure C.3c). We pick the Rayleigh-wave phase velocity based on the maximum of coherence every 0.5 Hz in the 3-10 Hz band and smooth the phase velocities with an average window (black line in Figure C.3c). Although the dispersion trend is continuous, these phase velocities can still be biased due to an anisotropic seismic source distribution (e.g. Yang & Ritzwoller, 2008; Yao & Van Der Hilst, 2009; Xu *et al.*, 2017). We examine the accuracy of the phase velocities in a qualitative way by comparing the C_{ZZ}-derived phase velocity (the black line in Figure C.3d) to the dispersion trend from C_{RR} (Figure C.3d). C_{RR} is less sensitive to anisotropic seismic source distributions (e.g. Xu & Mikesell, 2017). In the dispersion image (Figure C.3d), we observe that the phase velocities from C_{ZZ} are close to C_{RR} in the 4-10 Hz band. This similarity indicates that the phase velocities are reliable. Knowing that this dispersion estimation is an average phase velocity for the subsurface (e.g. Wang *et al.*, 2015), we use this dispersion estimation in the analytical Green's functions (Equations 5.1 and 5.2).

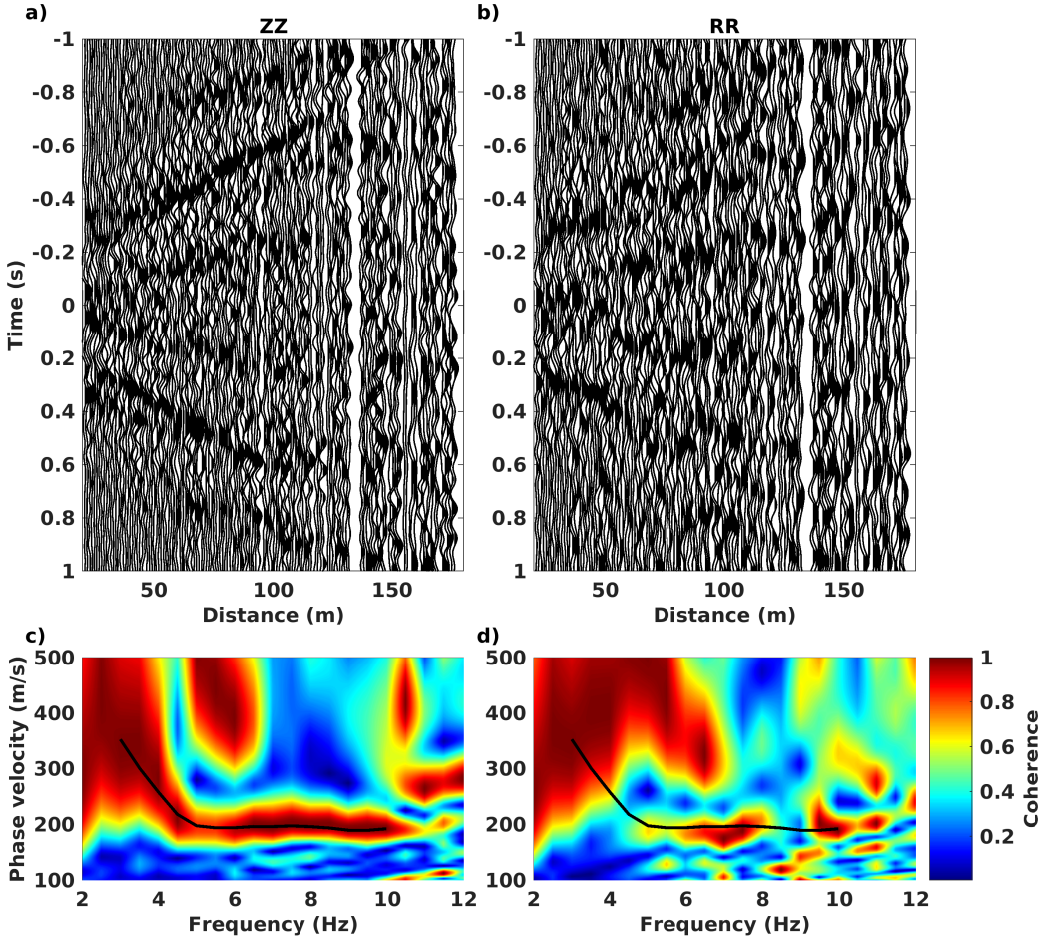

Figure C.3: The virtual shot gathers of C_{ZZ} (a) and C_{RR} (b) after applying a 1 m bin-stack to all crosscorrelations. We apply the phase-shift transform to the sum of causal and acausal parts of the crosscorrelations to generate the dispersion images (c and d). The black lines in the two dispersion images are the smoothed phase velocities from C_{ZZ}. The waveforms are band-pass filtered between 2-12 Hz.

C.3 Converting velocity recordings to displacement recordings

The geophones in this study recorded the ground motion velocity at the geophone locations, while the Green's functions (Equation 5.1 and 5.2) are the displacement Green's functions instead of the velocity Green's functions. Based on the Fourier transform, there is a ratio $i\omega$ that relates the spectra of velocity recordings (V) and the displacement recordings (U):

$$V = i\omega U. \tag{C.1}$$

For crosscorrelations this relationship becomes

$$VV^* = \omega^2 UU^*. \tag{C.2}$$

Thus in the estimation of the source energy spectral density (Equation 5.7 and 5.8), because we use the autocorrelation of the geophone recordings, we have to divide the estimation by ω^2 to estimate the displacement source energy spectral density (Figure 5.4).

The division is not necessary in the waveform inversions. Because the real crosscorrelations are for velocity, we need to transfer $G_{mp}G^*_{np}$ from displacement to velocity in the forward model (Equation 5.11) and the source kernel (Equation 5.13). The transfer requires multiplying by ω^2, and thus the division cancels with the multiplication. Therefore, we do not need to divide or multiply by ω^2 in the inversions. This is only done in Figure 5.4 because we wish to show the source energy spectral density

for the displacement Green's function.

APPENDIX D:

D.1 Rayleigh wave eigenfunctions

Rayleigh waves possess vertical (Z) and radial (R) components. In a 1D elastic media, one can write the two component displacements at frequency ω and depth z as

$$u_R = r_1(z,\omega)exp[i(k_R\Delta - \omega t)], \tag{D.1}$$

$$u_Z = r_2(z,\omega)exp[i(k_R\Delta - \omega t)], \tag{D.2}$$

where r_1 and r_2 are the eigenfunctions, k_R is the Rayleigh-wave wavenumber and Δ is the propagation distance (e.g. Aki & Richards, 2002). One can calculate the two eigenfunctions based on boundary conditions, vanishing traction at the free surface and no motion at infinity (e.g. Aki & Richards, 2002). In a homogeneous halfspace, the analytical expression for the two eigenfunctions are

$$r_1(z,\omega) = -k_R exp(-k_R\sqrt{1-\frac{c_R^2}{\alpha_0^2}}z) + k_R\frac{2\beta_0^2 - c_R^2}{2\beta_0^2}exp(-k_R\sqrt{1-\frac{c_R^2}{\beta_0^2}}z), \tag{D.3}$$

$$r_2(z,\omega) = -k_R\sqrt{1-\frac{c_R^2}{\alpha_0^2}}exp(-k_R\sqrt{1-\frac{c_R^2}{\alpha_0^2}}z) + k_R\frac{2\sqrt{1-\frac{c_R^2}{\alpha_0^2}}}{2-\frac{c_R^2}{\beta_0^2}}exp(-k_R\sqrt{1-\frac{c_R^2}{\beta_0^2}}z), \tag{D.4}$$

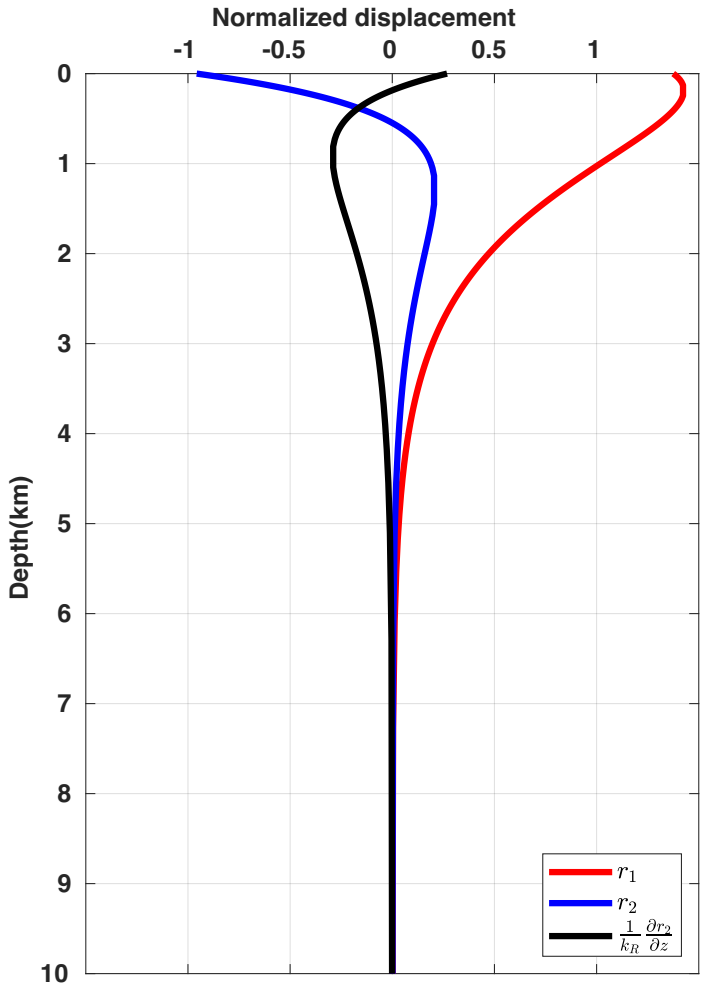

Figure D.1: r_1, r_2 and $\frac{1}{k_R}\frac{\partial r_2}{\partial z}$ vary with depths at 1 Hz.

where c_R is the Rayleigh-wave phase velocity at frequency ω, α_0 is the P-wave velocity, and β_0 is the S-wave velocity in the media. For the velocity model in Section 7.4 where α_0=5 km/s and β_0=3 km/s, we calculate the eigenfunctions and $\frac{1}{k_R}\frac{\partial r_2}{\partial z}$ (Figure D.1). We will use these in Equation 7.7, 7.11 and 7.12.

D.2 P-wave depth in the RP scattering

Rayleigh waves possess different displacements at all depths while P waves only possess displacement at one depth. Thus in the Monte Carlo simulation, we need the coordinate information in a surface (i.e. x and y) to indicate the position of a Rayleigh wave but need the coordinate information in a 3D space (i.e. x, y and z) for a P-wave position. For a RP scattering, the scattered P wave shares a same surface position as the incident Rayleigh wave, and we have to add a depth (z) to the P wave (i.e. place the P wave at a depth).

We see σ_λ^{RP} as a probability distribution for the RP scattering in depth (Figure D.2). We can generate possible depths for the scattered P wave (i.e. realizations of the distribution) using inverse transform sampling. This sampling method requires the cumulative distribution function of σ_λ^{RP} and a random number ($rand$) uniformly distributed from 0 to 1. We then find a depth (z) which satisfies

$$\frac{\int_0^z \sigma_\lambda^{RP} dz}{\int_0^\infty \sigma_\lambda^{RP} dz} = rand, \tag{D.5}$$

where the left hand side is the cumulative distribution (Figure D.2). The depth is the scattered P-wave depth. In practice, we will not do the integral ($\int_0^z \sigma_\lambda^{RP} dz$ in Equation D.5), but calculate the cumulative distribution at some depths prior to the Monte Carlo simulation and then interpolate the depth in the simulation (Algorithm 4).

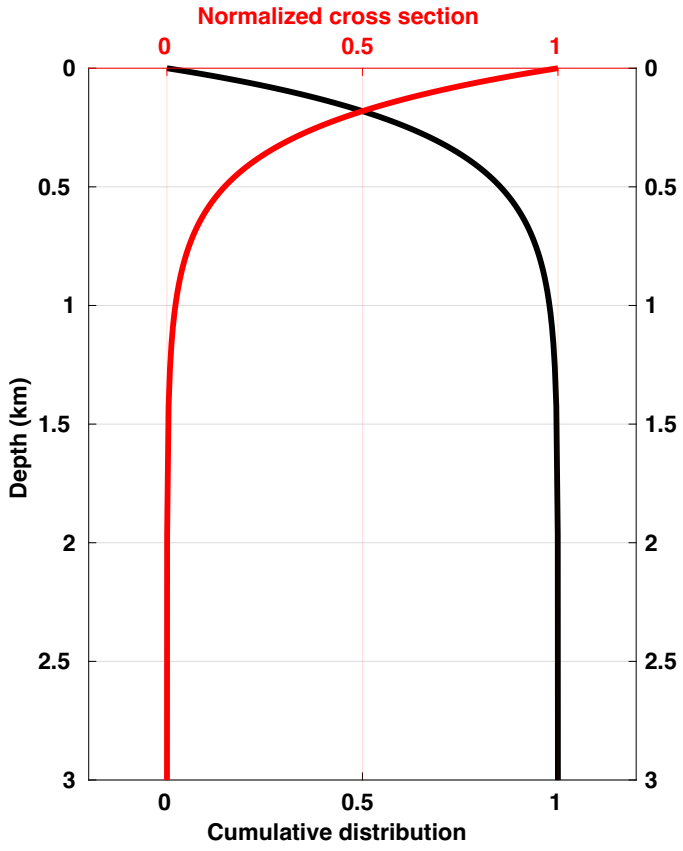

Figure D.2: We plot σ_λ^{RP} normalized by the value in the free surface (red) and the cumulative distribution function of σ_λ^{RP} (black).